UNIVERSITÀ DEGLI STUDI DI MILANO

Scuola di Dottorato in Fisica, Astrofisica e Fisica Applicata

Dipartimento di Fisica

Corso di Dottorato in Fisica, Astrofisica e Fisica Applicata

Ciclo XXX

Experimental study of Isospin symmetry in N=Z nuclei

Settore Scientifico Disciplinare FIS/04

Supervisore: Professor Franco CAMERA

Coordinatore: Professor Francesco RAGUSA

Tesi di Dottorato di:

Alice MENTANA

Anno Accademico 2016-2017

Referees of the thesis:

Prof. Adam Maj
Instytut Fizyki Jadrowej, Polskiej Akademii Nauk, Krakow, Poland

Prof. Giovanni La Rana
Universitá degli Studi di Napoli Federico II, Italy

Commission of the final examination:

Prof. Giuseppe Gorini
Universitá degli Studi di Milano-Bicocca, Italy

Prof. Gianluca Imbriani
Universitá degli Studi di Napoli Federico II, Italy

Prof. Franco Camera
Universitá degli Studi di Milano, Italy

Final examination:

26th February 2018

Università degli Studi di Milano, Dipartimento di Fisica, Milano, Italy

Cover illustration:

Andrea Zanzani

Internal illustrations:

Alice Mentana

Design:

Annalisa Varri

MIUR subjects:

FIS/04 - Fisica Nucleare e Subnucleare

Contents

Introduction

The Isospin symmetry is one of the first dynamical symmetries identified in nuclear physics. Like any symmetry, it helps us to simplify the description of a system, in this case the atomic nucleus, a quantum many-body system consisting of two types of fermion, the neutron and the proton, differing in charge but otherwise essentially identical in their behaviour [1].

The assumptions of the charge symmetry and charge independence of the nuclear interaction led to consider neutrons and protons as two different states of the same particle, the nucleon. To account for this, in 1932, Heisenberg introduced a new quantum number, the isotopic spin or Isospin. In the Isospin formalism, the nucleons are said to have Isospin I=1/2, and the neutron and the proton differ for the value of the Isospin operator projection I_z, 1/2 and -1/2 respectively. For a system of A nucleons, the atomic nucleus, $I_z = \frac{N-Z}{2}$ and I can assume values in the range $|I_z| \leqslant I \leqslant A/2$, according to quantum mechanical rules. In general, the ground state assumes the lowest possible value of Isospin, $I=I_z$, which means that, in self-conjugate nuclei, $I=I_z=0$.

The concept of Isospin symmetry neglects the presence of Coulomb interaction inside the atomic nucleus. This interaction, which is clearly charge dependent, breaks the Isospin symmetry, inducing a mixing between nuclear states with different Isospin values. Therefore, it is impossible to assign to a state a definite value of Isospin. This is the so called Isospin mixing phenomenon.

During the past years, the Isospin mixing phenomenon has been investigated from both theoretical and experimental point of view. It doubtless plays a key role in nuclear structure studies as, for instance, it contributes to explain the properties of the Isobaric Analog State. Furthermore, it represents an interesting phenomenon also beyond the nuclear structure field, due to its implication in the determination of the first term, V_{ud}, of the Cabibbo-Kobayashi-Maskawa (CKM) matrix. A precise value for this term, the *u*-quark to *d*-quark transition matrix element, is obtained from the experimental measurement of *ft* of $0^+ \rightarrow 0^+$ super-allowed Fermi β transitions, with some corrections. One of these, δ_C, depends on the Isospin mixing.

The Isospin cannot be directly measured. To test the Isospin symmetry, therefore, it is necessary to study transitions which would be forbidden if the Isospin was a good quantum number to describe the nucleus. An example are the electric dipole E1 transitions, and thus the IsoVector Giant Dipole Resonance (IVGDR) γ-decay (where the E1 strength is all concentrated), from I=0 states of N=Z nuclei. This approach has been used to measure the Isospin mixing in nuclei at finite temperature, formed using fusion-evaporation reactions among self-conjugate nuclei, to ensure the population of a compound nucleus in a I=0 state. The γ-decay of the IVGDR, built on this state, can be measured to deduce the mixing probability.
From the experimental point of view, this kind of measurement requires a dedicated apparatus characterized by high efficiency (to measure the high-energy γ-radiation from the decay of the IVGDR) and high granularity (to study the fusion-evaporation reaction and characterize the compound nucleus).

The investigation of the Isospin symmetry via the γ-decay of the IVGDR has been a scientific topic of interest for the nuclear physics group of Milano for several years. In the recent works of A. Corsi [2] and S. Ceruti [3], the Isospin mixing has been deduced in the nucleus ^{80}Zr at two different temperature values and, using the theoretical model describing the Isospin mixing temperature T dependence [4], the mixing probability at T=0 has been extracted. This has allowed to determinate, for the first time, the δ_C correction parameter for the calculation of the CKM matrix element V_{ud} [3].

In this thesis work a new experiment to investigate the Isospin mixing temperature dependence in the nucleus ^{60}Zn, via the γ-decay of the IVGDR, will be presented. It has been performed by Milano group in June 2016, with the final goal to extract the mixing probability at zero temperature and to obtain the value of δ_C parameter for ^{60}Zn. Such nucleus is located in an interesting mass region, where the δ_C parameter is expected to have a sudden increase. The Isospin mixing determination at T=0 in ^{60}Zn will provide a validation of both the used experimental technique (from the comparison with the existing experimental data in the same mass region, obtained using different experimental

techniques [5, 6]) and the theoretical model (through the comparison with the theoretical prediction [7]).
At the present time the data analysis of the experiment, which requires several years, is in the preliminary stage.

Alongside this, aim of this thesis is the characterization of two different types of detectors which could represent the future of the Isospin mixing experimental measurements.
The first one, the PARIS array [8], will be composed by 216 phoswich detectors, arranged in 24 clusters. The single phoswich is constituted by a $LaBr_3$:Ce or $CeBr_3$ scintillator, 2"x2"x2" in size, coupled to a NaI:Tl scintillator, 2"x2"x6" in size. The first crystal provides a good energy resolution for low energy γ-radiation, while the whole scintillation volume (2"x2"x8") is able to guarantee a good detection efficiency for high-energy γ-radiation. This features, together with the high granularity, make the PARIS array an ideal apparatus to investigate the Isospin mixing by measuring the γ-decay of the Isovector Giant Dipole Resonance. Indeed, the array can act simultaneously as multiplicity filter and high-energy calorimeter. In this work, the general properties of a single phoswich will be described and two characterization tests of the first array cluster, PARIS prototype, will be discussed.
The second detector is the CLYC (Cs_2LiYCl_6:Ce) scintillator, a very interesting material due to a good energy resolution and its capability to identify and measure neutrons and γ-rays. The Isospin mixing measurement via the γ-decay of IVGDR in self-conjugate nuclei heavier than ^{80}Zr demands the use of radioactive beams, that nowadays means low intensity beams. In this situation, small target-detector distances are necessary. Moreover, to measure the IVGDR decay, the capability to discriminate γ-rays from neutrons is an essential requirement. The CLYC scintillation properties allow to fulfil all of these conditions, making a CLYC scintillator array a unique solution for this kind of measurement. Currently, little is know about the performances of these detectors. In the context of a complete characterization work, a fast neutron detection efficiency measurement for two CLYC scintillator samples will be presented in this work.

In summary, Part I will be dedicated to the introduction of the physics case and to the description of the experimental technique. Part II will concern the characterization of the two array ideal for the Isospin mixing determination. Finally, the discussion on the preparation, realization and preliminary analysis of the experiment to determinate the Isospin mixing in ^{60}Zn will be will be addressed in Part III.

Part I

Isospin symmetry in nuclear structure

CHAPTER 1

Isospin symmetry

In this chapter we will give a general overview on the Isopin symmetry of the nuclear interaction. The Isospin quantum number will be presented. The breaking of this symmetry due to the Coulomb interaction, the so-called Isospin mixing phenomenon, will be then discussed together with the implications that it has in and beyond nuclear structure.

1.1 Charge invariance of nuclear interaction

A key feature of the nuclear interaction is associated to the presence, inside the atomic nucleus, of two kind of particles, the proton p, with a mass of m_p= 938.272 MeV/c^2, and the neutron n, with m_n=939.566 MeV/c^2. The near equality in their mass ($\frac{\triangle m}{m}$ = 0.14 %) firstly suggests the deep similarity between them and a more detailed study of their role has revealed a basic symmetry between neutron and proton in all nuclear interactions [9]. Charge symmetry is the assumption that *n-n* interaction is identical to the *p-p* one, corrected for the Coulomb force effect. A stronger assumption is charge independence, according to which the *p-n* interaction, in the singlet spin state, is also the same. Such assertions are supported by the experimental evidence of the similarity of *p-p*, *n-n* and *p-n* scattering lengths and effective ranges, after the *p-p* correction for the Coulomb interaction ([10] and references therein). The concept of charge symmetry

and charge independence lead us to consider, with good approximation, a symmetry between the neutron and the proton in the nuclear behaviour. This will be a very helpful tool in the description of the atomic nucleus.

1.2 The Isospin formalism

As a consequence of the charge independence of the nuclear interaction, it is convenient to adopt a formalism in which neutrons and protons are considered as different states of the same particle, the nucleon. On this basis, in 1932, Heisenberg introduced a quantum number, the Isobaric spin or Isospin [11]. The isospin operators **I** and I^2=I_x+I_y+I_z have the properties under rotation completely analogous to those of the spin [12]. In analogy with a spin 1/2 particle, which has two states, the nucleon has an Isospin value of I=1/2 and neutron and proton are two different projection I_z of the Isospin operator, with value +1/2 and -1/2 respectively.
The expression of the electric charge operator for the nucleons in terms of I_z is therefore:

$$Q = e(\frac{1}{2} - I_z). \tag{1.1}$$

This concept can be extended to a system of A nucleons, the nucleus. The I_z value corresponds to half the difference between number of neutrons (N) and number of proton (Z):

$$I_z = \frac{N - Z}{2}, \tag{1.2}$$

and the possible Isospin values associated to the nuclear states are:

$$|I_z| \leqslant I \leqslant \frac{N + Z}{2}. \tag{1.3}$$

The nuclear force prefers the states with the lowest possible Isospin value, therefore the Isospin of the nuclear ground state is generally I_0=$|I_z|$. An exception to this rule, which holds well for even-even and odd-mass nuclei, are some odd-odd nuclei like ^{34}Cl, ^{42}Sc, ^{46}V, ^{50}Mn, ^{54}Co, ^{62}Ga and ^{70}Br, where I_z = 0 and I(g.s.) = 1 [13].

Considering H the Hamiltonian for a system of A nucleons, charge conservation implies that H commutes with I_z:

$$[H, Q] = [H, I_z] = 0. \tag{1.4}$$

By complete analogy with spin conservation and rotational invariance under rotation, it is possible to give a more general definition of charge independence for the nuclear

interaction as:

$$[H, \mathbf{I}] = 0 \tag{1.5}$$

or

$$\left[H, I^2\right] = 0. \tag{1.6}$$

It means that the nuclear wave function is expected not to vary with the exchange of a neutron with a proton (or vice-versa).

An example of this is the internal structure of mirror nuclei, i.e. nuclei with the same mass but with the numbers of protons and neutrons interchanged (see Fig. 1.1). Formally, this neutron-proton exchange symmetry is described in terms of Isospin $|I, I_z\rangle$. In general, the yrast structures of a nucleus have I_0=$|I_z|$. Therefore, for example, for an odd-A mirror pair differing only through the exchange $1p$-$1n$, $I_z = \pm\frac{1}{2}$ and the low-lying states of the nuclei have I = $\frac{1}{2}$. In the absence of Coulomb effects, or other isospin non-conserving phenomena, these two sets of analogue states will be degenerate in energy [14]. However, since the presence of Coulomb interaction breaks the degeneracy, an energy shift in the level structure (of the order of tens of keV) results, as well as a difference in the binding energy of the states (of the order of tens of MeV) [15]. Nevertheless, the spatial symmetry of the wave functions of these analogue states is generally preserved [14]. Fig. 1.1 shows the partial level scheme of ^{51}Fe (Z=26,N=25) and ^{51}Mn (Z=25,N=26). The spectra are very similar to each other. Since the ground state are normalized to zero excitation energy, the difference in the binding energy is almost cancelled out and the only visible effects are the small energy shifts in the excited levels.

1.3 Breaking of the Isospin symmetry: the Isospin mixing

The concept of Isospin symmetry neglects the presence of Coulomb interaction inside the nucleus. Such interaction is clearly charge dependent and its effect is to break the symmetry. In other words, inside a nucleus, two competitive trends occurs: the nuclear force is strongly attractive in the isoscalar *p*-*n* channel, while the Coulomb force acts against this attraction by making neutron and proton states different [7]. In order to better understand the phenomenon, it is helpful to examine the expression of the Coulomb interaction in the Isospin formalism:

$$V_C = \sum_{i<j} \left(\frac{1}{2} - I_z^{(i)}\right)\left(\frac{1}{2} - I_z^{(j)}\right)\frac{e^2}{r_{ij}}. \tag{1.7}$$

It can be rewritten as the sum of an isoscalar $V_C^{(0)}$, an isovector $V_C^{(1)}$ and an isotensor $V_C^{(2)}$ terms:

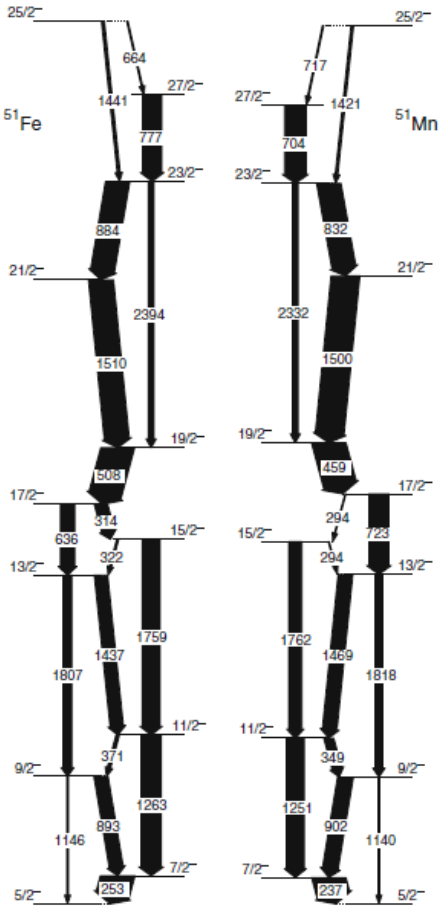

Figure 1.1: Mirror nuclei partial level schemes [15]. It refers to yrast negative-parity states of ^{51}Fe (Z=26,N=25) [16] and of ^{51}Mn (Z=25,N=26) [17].

$$
\begin{aligned}
V_C^{(0)} &= \sum_{i<j} \frac{1}{4}\frac{e^2}{r_{ij}}(1 + \frac{4}{3}\mathbf{I}^{(i)} \cdot \mathbf{I}^{(j)}),\\
V_C^{(1)} &= -\sum_{i<j} \frac{1}{2}\frac{e^2}{r_{ij}}(I_z^{(i)} + I_z^{(j)}),\\
V_C^{(2)} &= \sum_{i<j} \frac{1}{4}\frac{e^2}{r_{ij}}(4I_z^{(i)}I_z^{(j)} - \frac{4}{3}\mathbf{I}^{(i)} \cdot \mathbf{I}^{(j)}).
\end{aligned} \tag{1.8}
$$

While the isoscalar term has no effects, the isovector and isotensor ones are responsible for Isospin impurities in the nuclear wave function with $\triangle$I=1 and $\triangle$I=2 states respec-

tively: Isospin is no more a conserved quantum number, i.e. a good quantum number to describe the system. This phenomenon is generally called Isospin mixing.

Since the Coulomb interaction is much weaker than the nuclear one between nucleons, the effect of the symmetry breaking can be treated using a perturbative approach. In first order perturbation theory, the probability to have admixture of $I=I_0+1$ states into $I=I_0$ ones, α^2, is defined as:

$$\alpha^2 = \sum_{I_0+1} \frac{|\langle I = I_0 + 1| V_C^{(1)} |I_0\rangle|^2}{(E_{I_0+1} - E_{I_0})^2}. \tag{1.9}$$

Coulomb interaction preserves angular momentum J and parity π, so it can couple only states with the same J^π. Moreover, due to the denominator of eq. 1.9, the mixing effect is significant only between states close in energy, with a similar spacial wave function. Since the states with $\triangle I=2$ have a much higher energy difference than the $\triangle I=1$, the mixing contribution due to isotensor term $V_C^{(2)}$ is smaller than the one due to $V_C^{(1)}$.

The degree of mixing in the ground state (*g.s.*) of a nucleus gives information on how much the Isospin is a good quantum number to describe the system. The effect of the Coulomb force against the nuclear force, who leads towards the N=Z nuclei, is to bend away the stability valley toward the neutron-rich nuclei with the increasing of the mass number (A>40). This is the reason why the largest mixing degrees is expected in N=Z nuclei, as in nuclei near the proton drip line. A typical example is the ^{100}Sn, the heaviest bound N=Z nucleus in the nuclear chart, where microscopical calculation predicts a large α^2 value of about 5-6% [18].
The *g.s.* of a self-conjugate nucleus can be written as a linear combination of I=0 and I=1 states:

$$|g.s.\rangle = \beta|I = 0\rangle + \alpha|I = 1\rangle \tag{1.10}$$

where, using eq. 1.9, α^2 is:

$$\alpha^2 = \sum_{I=1} \frac{|\langle I = 1| V_C^{(1)} |I = 0\rangle|^2}{(E_{I=1} - E_{I=0})^2}. \tag{1.11}$$

The Isospin mixing phenomenon has been largely investigated, during the past years, from both theoretical and experimental point of view (see, for example [1, 6, 7, 18–20]). The development of experimental facilities to produces radioactive beams has allowed access to the proton-rich zone of the nuclear chart, the most interesting one for the mixing investigation. On the other hand, several theoretical calculation has been performed, using different approaches. Fig. 1.2 displays the A (or, equivalently, Z) dependence of the mixing probability, calculated using an Energy Density Functional (EDF) approach,

for self-conjugate nuclei up to Z=50. As one can expects, this probability increases with the number of protons Z.

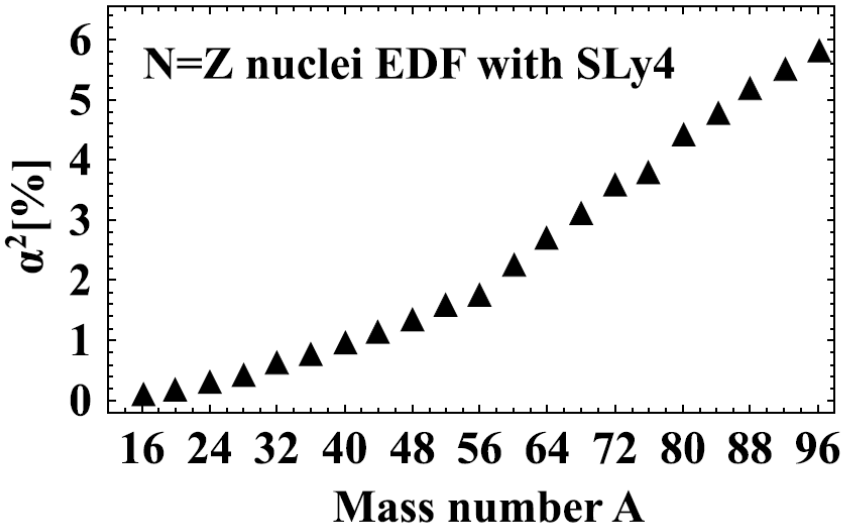

Figure 1.2: The isospin-mixing parameter α^2 for the ground state of even-even N=Z nuclei calculated using a Energy Density Functional approach and a SLy4 nuclear interaction. Adapted from [7] ([21]).

1.3.1 Isospin mixing and excitation energy

With the increasing of the excitation energy, the states lie close together and acquire a finite particle decay width Γ, since the particle threshold is exceeded. Such decay width increases with the excitation energy, and therefore with the number of decay channels opened. Equation 1.9 is no more valid and can be rewritten in a generalized form, accounting for this situation with a complex energy [22]:

$$\alpha^2 = \sum_{I_0+1} |\frac{\langle I = I_0 + 1| V_C^{(1)} |I_0\rangle}{(E_{I_0+1} + i\Gamma_{I=I_0+1}/2) - (E_{I_0} + i\Gamma_{I=I_0}/2)}|^2. \tag{1.12}$$

Looking at the denominator, it is clear that, if the decay width Γ is negligible, α^2 would increase as the level spacing decreases (eq. 1.9). However, since Γ becomes important with the excitation energy, one expects to have the maximum of α^2 when the level spacing and the decay width are similar.

Around 1955, Wilkinson [23] and Morinaga [24] proposed a time-dependent approach to describe the (inherently time-dependent) situation at high excitation energy

in compound nuclei (CN), alternative to the time-independent perturbation theory of eq. 1.12. (For a discussion on the compound nucleus, see Appendix A.) They started from the idea that, at high excitation energy, the nuclear decay width becomes so large to overwhelm the Coulomb interaction effects, restoring the Isospin symmetry.
According to their model, the time-independent nuclear states of a compound nucleus do not have a good Isospin themselves but, when a reaction forms a compound nucleus, initially this can be viewed as a superposition of defined-Isospin states. Because of the high-excitation energy, the compound nucleus decay occurs before the Isospin degree of freedom has time to equilibrate. This implies a dynamical behaviour between the Coulomb interaction time-scale and the compound nucleus lifetimes [22][9]. In order to better understand this concept is useful to describe the effect of the Coulomb interaction not in terms of a matrix element, but in terms of a spreading width, whose meaning is illustrated introducing the following picket fence model. We consider to have a number of I=0 levels with the same energy difference D and a I=1 state that lies between two of them at energy $E_{I=1}$. Its effect is to perturb the system, connecting the I=1 state with the underlying I=0 states. We call v the constant matrix element of the perturbation. The probability $P_{I=1}[E]$ of the I=1 configuration per unit energy interval, in the limit of $v \ll D$ is given by a Breit-Wigner distribution [9]:

$$P_{I=1}[E] = \frac{1}{2\pi} \frac{\Gamma^{\downarrow}}{(E_{I=1} - E)^2 + (\Gamma^{\downarrow}/2)^2}, \tag{1.13}$$

characterized by the Coulomb spreading width $\Gamma^{\downarrow}$ of the I=1 state:

$$\Gamma^{\downarrow} = \frac{2\pi v^2}{D}.$$

We analyse now the previous problem using a time-dependent approach. At t=0, only the state with I=0 is populated. The probability amplitude ($A_{I=1}[t]$) to find the system in the I=1 state at some later time t is given by:

$$A_{I=1}[t] = exp\left[-\frac{\Gamma^{\downarrow}}{2\hbar}t - \frac{i}{\hbar}E_{I=1}t\right]. \tag{1.14}$$

Therefore the I=1 state decays into, or in other words it mixes up with, a I=0 state with an exponential decay time of $\hbar/\Gamma^{\downarrow}$. This process gets into competition with the nuclear decay (Γ). In particular, if the latter is so fast not to allow the mixing to completely establish (high excitation energy) is it possible to say that the Isospin symmetry is restored. In

this sense, the dynamical behaviour of the mixing can be approximate with:

$$\alpha^2 \simeq \frac{\Gamma^{\downarrow}}{\Gamma}, \tag{1.15}$$

i.e. it is the ratio of the decay time of the system to the time for Isospin mixing ($\Gamma^{\downarrow} \sim 2\hbar/\tau_{mixing}$).

Parametrization of Harney, Richter and Weidenmüller

The Wilkinson and Morinaga time-dependent approach just described was formalized by Harney, Richter and Weidenmller (1986) [25]. They proposed a parametrization that takes into account both the Isospin formalism and the statistical description of compound nuclei. Two pure Isospin states are considered as starting point: $|I_<\rangle = |I, I_z\rangle$ and $|I_>\rangle = |I+1, I_z\rangle$. The description of the mixing of states $|I_<\rangle$ into $|I_>\rangle$ is performed using the Coulomb spreading width $\Gamma^{\downarrow}_{>}$:

$$\Gamma^{\downarrow}_{>} = 2\pi\overline{|\langle I_>|H_C|I_<\rangle|^2}\rho(I_<), \tag{1.16}$$

where $\rho(I_<)$ is the density of states $|I_<\rangle$. $\Gamma^{\downarrow}_{>}$ defines the time-scale of the mixing induced by the Coulomb interaction H_C.
By exchanging $>$ and $<$ in eq. 1.16, it is possible to define $\Gamma^{\downarrow}_{<}$, related to $\Gamma^{\downarrow}_{>}$ by the detailed balance:

$$\Gamma^{\downarrow}_{>} = \frac{\rho(I_>)}{\rho(I_<)}\Gamma^{\downarrow}_{<}. \tag{1.17}$$

Using the S-matrix formalism, the fraction $\alpha^2_<$ of states $|I_<\rangle$ that mix to states $|I_>\rangle$ can be written as:

$$\alpha^2_< = \frac{\Gamma^{\downarrow}_{<}/\Gamma^{\uparrow}_{<}}{1 + \Gamma^{\downarrow}_{<}/\Gamma^{\uparrow}_{<} + \Gamma^{\downarrow}_{>}/\Gamma^{\uparrow}_{>}}, \tag{1.18}$$

where $\Gamma^{\uparrow}$ is the compound nucleus decay width. Similarly, the fraction $\alpha^2_>$ of states $|I_>\rangle$ that mix to states $|I_<\rangle$ is:

$$\alpha^2_> = \frac{\Gamma^{\downarrow}_{>}/\Gamma^{\uparrow}_{>}}{1 + \Gamma^{\downarrow}_{>}/\Gamma^{\uparrow}_{>} + \Gamma^{\downarrow}_{<}/\Gamma^{\uparrow}_{<}}. \tag{1.19}$$

For small mixing, eq. 1.19 is reduced to eq. 1.15, $\Gamma^{\downarrow}_{<}/\Gamma^{\uparrow}_{<} = \tau_{CN}/\tau_{mixing}$, and this confirms the Wilkinson hypothesis that, at finite excitation energy, the mixing degrees should depends only on the ratio between the time scale characterizing the Isospin mixing process and the CN decay. For larger mixing degrees it is necessary to take into account also the correction in the denominator, that give the probability that $|I_>\rangle$ states mix back to $|I_<\rangle$ ones.

1.3.2 Isospin mixing at finite temperature

The Isospin mixing phenomenon has been investigated also through its connection with the isobaric analog state, IAS (see Appendix B). An explicit relation between the spreading width of the IAS and the mixing probability of the corresponding parent nucleus has been derived at zero temperature using a microscopic model based on the Feshbach projection method [19]. The nuclear temperature dependence of the Isospin mixing probability and, in particular, the restoration of the Isospin symmetry at high temperature have been then quantitatively studied extending the microscopic model mentioned above to the case of excited compound nuclei [4]. The relation between the Isospin mixing probability $\alpha^2_{I_0+1}$, the spreading width of the isobaric analog state $\Gamma^{\downarrow}_{IAS}$ and the statistical decay width of the compound nucleus has been found to be:

$$\alpha^2_{I_0+1} = \frac{1}{I_0+1}\frac{\Gamma^{\downarrow}_{IAS}}{\Gamma^{\uparrow}_{CN}(E^*)+\Gamma_M(E_{IAS})}, \tag{1.20}$$

where $\Gamma_M(E_{IAS})$ is the Coulomb spreading width of the IsoVector Giant Monopole Resonance (IVGMR) at the energy of the IAS, a quantity that cannot be experimentally measured and it remains as a parameter of the model. As one can clearly see in Fig. 1.3 for the case of ^{208}Pb, the mixing probability remains nearly constant with the temperature up to about 1 MeV and then decreases up to around 1/4 of its zero temperature value, because of the short lifetimes of the compound system, at temperature higher than about 3 MeV [4].

It is worth to note that the Coulomb spreading of a compound nucleus width $\Gamma^{\downarrow}$ is physically equivalent to the spreading width of the corresponding IAS $\Gamma^{\downarrow}_{IAS}$, since they are both originated by the Isospin mixing. This assumption is supported by the experimental data, as shown in Fig. 1.4. According to [26], the slight temperature T dependence of these quantities has been parametrized as:

$$\Gamma^{\downarrow}(T) = \Gamma(T=0)\cdot(1+cT), \tag{1.21}$$

where the parameter *c* should be determined trough a microscopic calculation [4].

1.4 Isospin mixing in the standard model

The Isospin mixing investigation is not only a nuclear structure issue: its relevance has also a close connection with the standard model, since it is involved in the determination of the first term, V_{ud}, of the Cabibbo-Kobayashi-Maskawa (CKM) matrix [28]. The CKM matrix terms contain information on the strength of flavour-changing weak decays

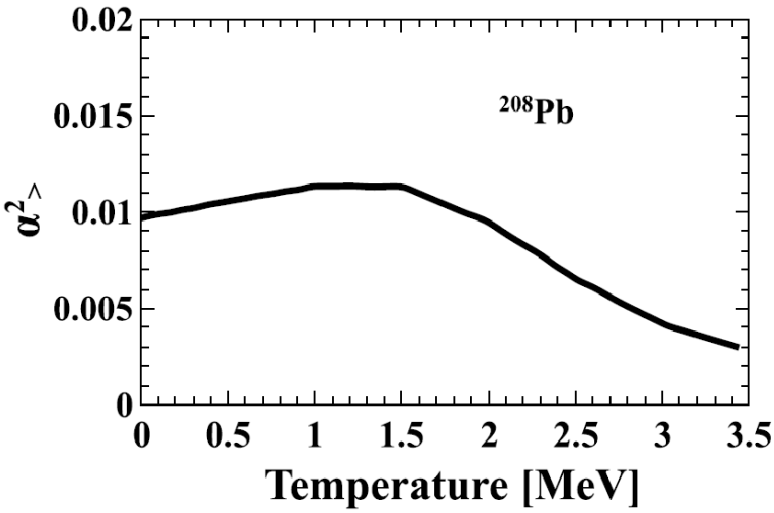

Figure 1.3: Temperature dependence of the Isospin mixing probability $\alpha^2_>$ for the nucleus ^{208}Pb. Adapted from [4] ([21]).

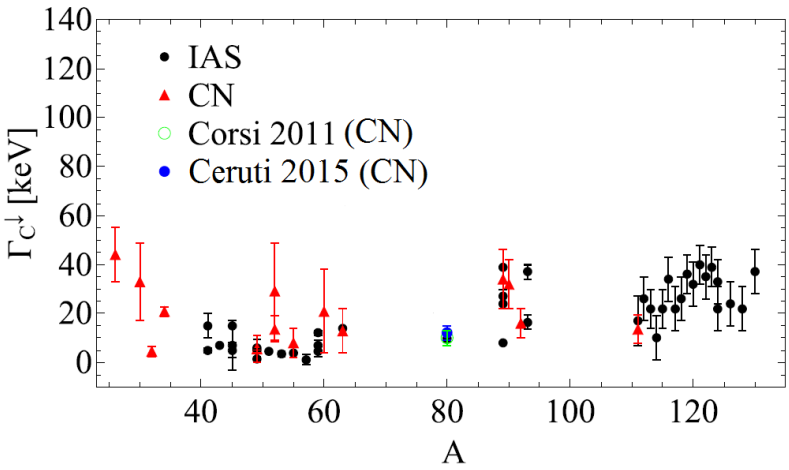

Figure 1.4: Experimental values of the Coulomb spreading width obtained from IAS (black dots) and from CN (red triangles, green dot [2] and blue circle [27]) [25]. Taken from [27].

among quarks:

$$V_{CKM} = \begin{pmatrix} V_{ud} & V_{us} & V_{ub} \\ V_{cd} & V_{cs} & V_{cb} \\ V_{td} & V_{ts} & V_{tb} \end{pmatrix}$$

The test of the unitarity of the CKM matrix is a fundamental pillar of the minimal standard model. The key ingredient for this test is a precise determination of V_{ud}, the transition matrix element between quark-*u* and quark-*d*, that is achieved trough the determination of the vector coupling constant G_v [29].

The most precise value for V_{ud} is provided by the experimental measurement of the transition *ft* value, a sort of partial half-life of the transition, in superallowed $0^+ \rightarrow 0^+$ nuclear β decay [30]. G_v can be obtained from the measured *ft* using:

$$ft = \frac{K}{G_v |M_F|^2}, \tag{1.22}$$

where $K/(\hbar c)^6 = 2\pi^3 \hbar \ln 2/(m_e c^2)^5$ and $|M_F|$ is the Fermi matrix element. Depending only on true constant (not renormalized to another value in the nuclear medium) [31], *ft* should be nucleus independent. As one can see in the left panel of Fig. 1.5, from the experimental data it is clear that this is not true and eq. 1.22 should be amended slightly by introducing two corrective terms. The first one, δ_R, is a radiative correction, to account for loss in the detection of bremsstrahlung photon coming from the emitted electrons. The second one, δ_C, is due to the Isospin symmetry breaking that cause a slight reduction of the matrix element $|M_F|$ respect to its Isospin-invariant value $|M_0|$: $|M_F|^2 = |M_0|^2(1 - \delta_C)$.

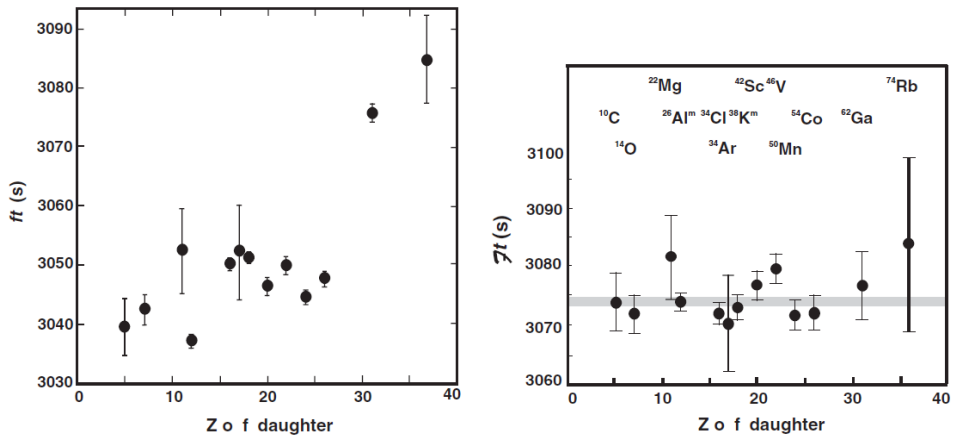

Figure 1.5: Left panel: the *ft* values for the 13 best-known superallowed decays. Right panel: $\mathcal{F}t$ values for the same 13 decays, resulting after the corrections (eq. 1.23). The shaded horizontal band gives one standard deviation around the average $\mathcal{F}t$ value ([29] and references therein)

.

Taking into account these considerations, Towner and Hardy [32] defined a corrected

ft value:

$$\mathcal{F}t \equiv ft(1+\delta_R)(1-\delta_C). \tag{1.23}$$

Since the data of $\mathcal{F}t$, taken in different mass regions, are consistent as they are expected to be (see Fig. 1.5, right panel), it is possible to use the average value $\overline{\mathcal{F}t}$ to calculate G_ν and then V_{ud} through the relation: $V_{ud} = \frac{G_\nu}{G_F}$, where G_F is the weak interaction constant. However, to reach the request accuracy in the determination of G_ν and V_{ud} the corrections to *ft*, which are all of the order of 1%, must be calculated with an accuracy of 10% of their central value (namely 0.1%). This is a strict demand especially for the nuclear structure dependent term [32].

Many theoretical studies has been made to obtain a parametrization of δ_C as a function of the mass number A [6, 33, 34]. The one proposed by Auerbach [35] points out the explicit relation between δ_C and the Isospin mixing probability α^2 in the ground state:

$$\delta_C = 4(I+1)\frac{V_1}{41\xi A^{2/3}}\alpha^2, \tag{1.24}$$

where V_1 = 100 MeV, ξ = 3 and I is the Isospin of the nucleus. Figure 1.6 shows the comparison between the experimental values of δ_C, obtained from *ft* measurements [6] and from mass measurements [36], and two theoretical calculations. The experimental values are therefore obtained using eq. 1.23, assuming the constance of $\mathcal{F}t$ for all the nuclei. This is, together with the *ft* experimental measurement precision, the strong limit of this method.

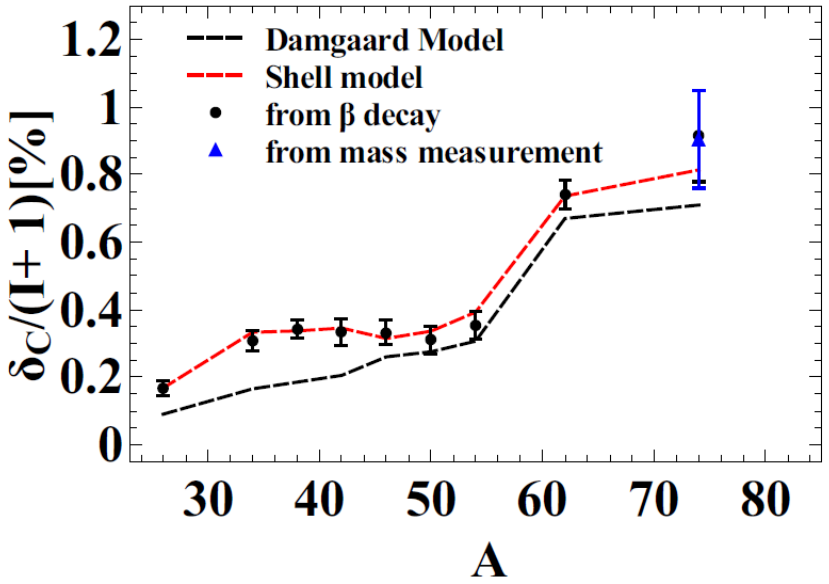

Figure 1.6: The Isospin symmetry breaking correction parameter δ_C as a function of the mass number A: comparison between theoretical models and experimental data [21]. The dashed black line refers to the Damgaard model prediction [37]. The dashed red line refers to shell-model with Saxon-Woods radial wave function prediction [38]. The black circles and the blue triangle are the experimental points obtained from β-decay ([6]) and mass measurement ([36]) respectively.

CHAPTER 2

Isospin mixing experimental measurement

In this chapter we will introduce the experimental technique we use to investigate the Isospin mixing, i.e. the γ-decay of the IsoVector Giant Dipole Resonance (IVGDR). We will start explaining why this phenomenon is a good probe to test the Isospin symmetry and then we will analyse the IsoVector Giant Dipole Resonance and its characteristics. Finally we will discuss the method to extract the Isospin mixing probability and we will give an overview on the recent experimental results reported in literature relative to this technique.

2.1 Electric Dipole E1 transitions

The Isospin is not an observable that one can directly measure. As a consequence, in order to obtain informations about the Isospin mixing, it is necessary to choose a phenomenon strictly connected to the Isospin conservation. The electromagnetic transitions are an example of this.

To better understand the concept, we follow the line illustrated in [12]. The electromagnetic transition from a nuclear state ″a″ to a nuclear state ″b″ can be expressed in

terms of the matrix element:

$$\Gamma_\gamma(L) = 8\pi k \sum_{M,M_b} |\langle J_b, M_b; I_b, I_{zb}| H(L,M) |J_a, M_a; I_a, I_{z,a}\rangle|^2, \tag{2.1}$$

where the interaction Hamiltonian H(L,M) is given by:

$$H(L,M) = \int \frac{1}{c} \mathbf{j}_N(\mathbf{r}) \cdot \mathbf{A}^*_{LM}(k\mathbf{r}) d\tau. \tag{2.2}$$

$\mathbf{j}_N(\mathbf{r})$ and $\mathbf{A}^*_{LM}(k\mathbf{r})$ are the nuclear current density and the vector potential of the electromagnetic field respectively. On the basis of its Isospin dependence, the nuclear current density can be decomposed in two terms: an isovector one, $\mathbf{j}^{(1)}_N$, linearly dependent on I_z and an isoscalar one, $\mathbf{j}^{(0)}_N$, independent of I_z. Since:

$$\mathbf{j}_N = \mathbf{j}^{(0)}_N + \mathbf{j}^{(1)}_N \tag{2.3}$$

it is useful to separate also the matrix element:

$$\langle J_b, M_b; I_b, I_{zb}| H_0(L,M) + H_1(L,M) |J_a, M_a; I_a, I_{z,a}\rangle, \tag{2.4}$$

being H_0 and H_1 the isoscalar and isovector interaction respectively. Using the Wigner-Eckhart theorem to make the I_z dependence explicit, one obtains:

$$\begin{aligned}
&\langle J_b, M_b; I_b, I_{zb}| H_0(L,M) + H_1(L,M) |J_a, M_a; I_a, I_{z,a}\rangle = \\
&\quad = (-1)^{I_b - I_{zb}} \begin{pmatrix} I_b & 0 & I_a \\ -I_{zb} & 0 & I_{za} \end{pmatrix} \langle J_b, M_b; I_b| H_0(L,M) |J_a, M_a; I_a\rangle \\
&\quad + (-1)^{I_b - I_{zb}} \begin{pmatrix} I_b & 1 & I_a \\ -I_{zb} & 0 & I_{za} \end{pmatrix} \langle J_b, M_b; I_b| H_1(L,M) |J_a, M_a; I_a\rangle.
\end{aligned} \tag{2.5}$$

Since both the isoscalar and isovector terms in eq. 2.5 do not vanish only if I_{za}=I_{zb}, the first Isospin selection rule for the electromagnetic transition is:

$$\triangle I_z = 0, \tag{2.6}$$

which formalizes that an electromagnetic transition cannot occur between different nuclei. The Wigner coefficients in eq. 2.5 allow us to deduce another Isospin selection rule:

$$\triangle I = 0, \pm 1. \tag{2.7}$$

Indeed,

$$(-1)^{I_b - I_{zb}} \begin{pmatrix} I_b & 0 & I_a \\ -I_z & 0 & I_z \end{pmatrix} = (2I_a + 1)^{-1/2} \delta_{I_a I_b} \tag{2.8}$$

points out that the isoscalar contribution vanishes except for $I \rightarrow I$ transitions. For the isovector part, corresponding to $I_a = I_b \pm 1$:

$$\begin{aligned} (-1)^{I_b - I_{zb}} \begin{pmatrix} I_b & 1 & I_a \\ -I_z & 0 & I_z \end{pmatrix} &= (-1)^{I_b + I_z} \begin{pmatrix} I_b & 1 & I_a \\ I_z & 0 & -I_z \end{pmatrix} = \\ &= (-1)^{I_b - I_a} \left[\frac{I_>^2 - I_z^2}{I_>(2I_> - 1)(2I_> + 1)} \right]^{1/2}, \end{aligned} \tag{2.9}$$

where $I_>$ is the larger between I_a and I_b.
It is worth to note, from eq. 2.5 that in self-conjugate nuclei, where I_z=0, the $\triangle$I=0 isovector contribution vanishes.

An important consideration is to be made now. In long-wavelength limit, the E1 operator is fully isovector. It becomes clear writing the electric dipole operator in the Isospin formalism [21, 22]:

$$\begin{aligned} H(L = 1, M) \simeq \sum_{i=1}^{A} q_i \mathbf{r}_i &= \sum_{i=1}^{A} (\frac{1}{2} - I_{zi}) \mathbf{r}_i = \\ &= \frac{1}{2} \mathbf{R}_{COM} + \sum_{i=1}^{A} I_{zi} \mathbf{r}_i = \\ &= H_0(L = 1, M) + H_1(L = 1, M) \end{aligned} \tag{2.10}$$

The isoscalar term H_0 depends only on the center of mass coordinate ($\mathbf{R}_{COM}$) and, therefore, it is not responsible for any excitation (its matrix element vanishes) and thus E1 operator allows only isovector transitions. It follows the rule:

$\triangle$I=0 E1 transitions in self-conjugate nuclei are forbidden.

Therefore, in N=Z nuclei only E1 transitions with $\triangle$I=$\pm$1 are allowed, with a consequent reduction of the decay strength.

In this sense, $\triangle$I=0 E1 transitions in self-conjugate nuclei, which are forbidden by the selection rules unless the Isospin mixing is taken into account, represent a good probe to test the Isospin symmetry. To better understand this concept, we consider a N=Z nucleus in a I=0 state: due to the selection rules, its only possible decay is to a I=1 state. This kind of decay has a very low yield for energetic reasons: only few I=1 states lie at lower energy than I=0 states. The presence of mixing (for the initial state $|I\rangle = \beta|0\rangle + \alpha|1\rangle$) increases the γ-decay yield. Such enhancement in the yield is a signature of the Isospin

mixing and it can be used to quantify the mixing degree.

As will be discussed in sec. 2.2, the E1 strength is all concentrated in the IsoVector Giant Dipole Resonance (IVGDR) γ-decay and thus it is the phenomenon we are going to study to obtain a quantitative information about the Isospin mixing.

2.2 IsoVecto Giant Dipole Resonance (IVGDR)

Giant resonances correspond to a collective motion involving many if not all the particle in the nucleus [39]. From a quantum-mechanical point of view, it corresponds to a transition between the ground state and the collective state of the many-body quantum system. The transition strength depends only on the basics properties of the system. If the resonance exhausts the major part of the total transition *sum rule* (more than 50%), we call it giant resonance. Macroscopically, a giant resonance can be seen as a high-frequency, damped, (nearly) harmonic density/shape vibration around the density/shape equilibrium of the nuclear system. Its oscillation amplitude is quite small, about a few percent of the nuclear radius. A (giant) resonance is described by three characteristics parameters: the energy E_R, the width Γ_R and the strength S_R [39].

The IsoVector Giant Dipole Resonance (IVGDR) is probably the best known and studied giant resonance. It is a very general phenomenon, since it occurs in all the nuclei from the ^{4}He up to ^{238}U [40].
The IVGDR is generally observed in photo-absorption experiments with a γ-ray beam of energy between 10 and 20 MeV. The wavelength associated to the projectile ($\hbar\omega_\gamma \approx$ 15 MeV) is $\lambda_\gamma \approx 100$ fm, much larger than the nuclear radius. In this condition it is possible to assert that the nucleus fills a constant electric field **E** and the protons move in the direction of **E**. To keep at rest the center of mass and to conserve the momentum, the neutrons move in the opposite direction. The attractive nuclear force acts as a restoring force which reverses the motion of neutrons and protons. Therefore, the IVGDR can be macroscopically viewed as an oscillation out-of-phase of neutrons and protons. From the microscopical point of view, the IVGDR is a coherent linear combination of 1p-1h (one particle-one hole) excitations.

Considering non-deformed nuclei with mass number A>50, the shape of the total absorption cross section $\sigma(\gamma, n)$, as shown in Fig. 2.1, is well reproduced by a Lorentzian curve:

$$\sigma(E) = \frac{\sigma_0}{1 + \left[(E^2 - E_0^2)^2/E^2\Gamma^2\right]}, \tag{2.11}$$

where E_0, σ_0 and Γ are the centroid position, the centroid cross-section and the full width at half maximum respectively.
The IVGDR centroid energy E_0 depends on the nuclear mass. It has been parametrized

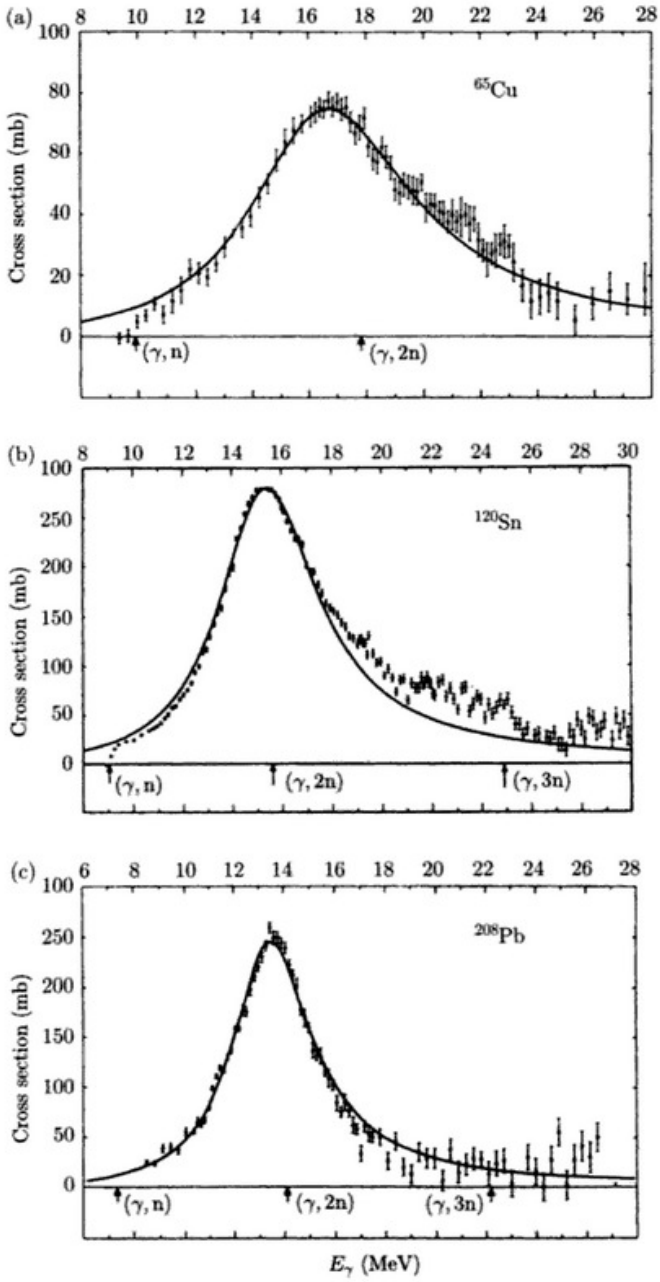

Figure 2.1: Photo-neutron cross section as a function of the photon energy for the nuclei ^{65}Cu (panel a), ^{120}Sn (panel b) and ^{208}Pb (panel c) [39].

using a combined power relation ([40, 40]):

$$E_0 = 31.2A^{-1/3} + 20.6A^{-1/6} MeV, \tag{2.12}$$

where A is the nucleus mass number. The trends of experimental data is such that the term $A^{-1/3}$ becomes dominant for increasing A. This can be explained by the fact that in heavier nuclei a larger fraction of the nucleons is located in the interior (rather than on the surface), so the surface term becomes less important.
In axially symmetric deformed nuclei, the photoabsorption cross section is split in two Lorentzian components (see Fig. 2.2) with different centroid, corresponding to the different oscillation axes.
The strength of the IVGDR, in terms of the Thomas-Reiche-Kuhn (TKR) sum rule, is:

$$S_{IVGDR} = \int_{E_{min}}^{E_{max}} \sigma_\gamma^{abs} dE = \frac{60NZ}{A} MeV \cdot mb. \tag{2.13}$$

S_{IVGDR} exhausts ~100% of the energy weighted sum rules for the electric dipole operator and the γ-decay of the IVGDR has a E1 character.
The width of the IVGDR built on the nuclear ground states varies from ~4 MeV up to ~8 MeV and it is smaller in closed-shell nuclei (see Fig. 2.3). It can be written as:

$$\Gamma = \Gamma^\uparrow + \Gamma^\downarrow. \tag{2.14}$$

$\Gamma^\uparrow$ is the escape width, associated to particle emission, while $\Gamma^\downarrow$ is the spreading width due to the mixing of the 1p-1h state to more complicated configuration (np-nh). The contribution of $\Gamma^\uparrow$ is, for heavy nuclei, less than 10%, so the dominant term is $\Gamma^\downarrow$.

2.2.1 IVGDR in hot nuclei

The high-excited nuclei decay occurs through the emission of light particles, such as protons, neutrons, α-particles etc., or γ-rays. The probability of γ-ray emission is about 10^3-10^5 times smaller than the particle one. In the case of energy constant E1 transition probability, the statistical model predicts that the γ-decay yield will decrease with the increasing of the γ-ray energy. The experiments ([42]), however, showed an enhancement of the γ-decay yield in the IVGDR region that has been interpreted as the coupling between the nuclear system, excited at an energy E^*, to a system in which the IVGDR is built on an excited state with energy $E_x = E^* - E_{GDR}$ [39]. The γ-decay probability of the IVGDR is higher than the one given by the statistical model and therefore the coupling results in the observed enhancement.
In 1981 it was experimentally established that the same phenomenon of increased γ-

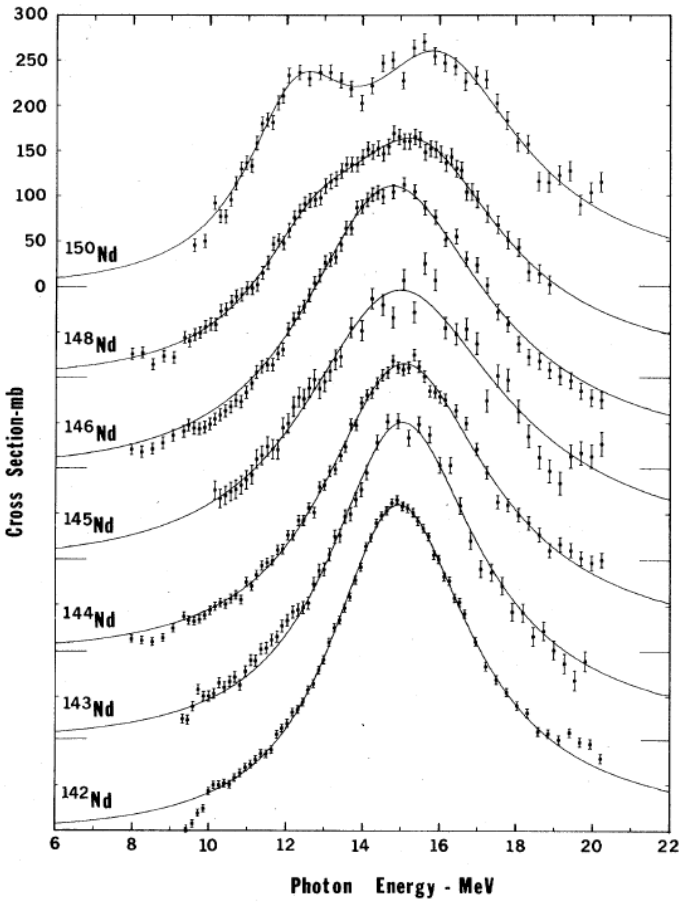

Figure 2.2: Photo-neutron cross section for Nd isotopes [39]. The development of a static deformation (with the increasing of the neutron number N) translate into a split of the GDR peak in two Lorentzians [40].

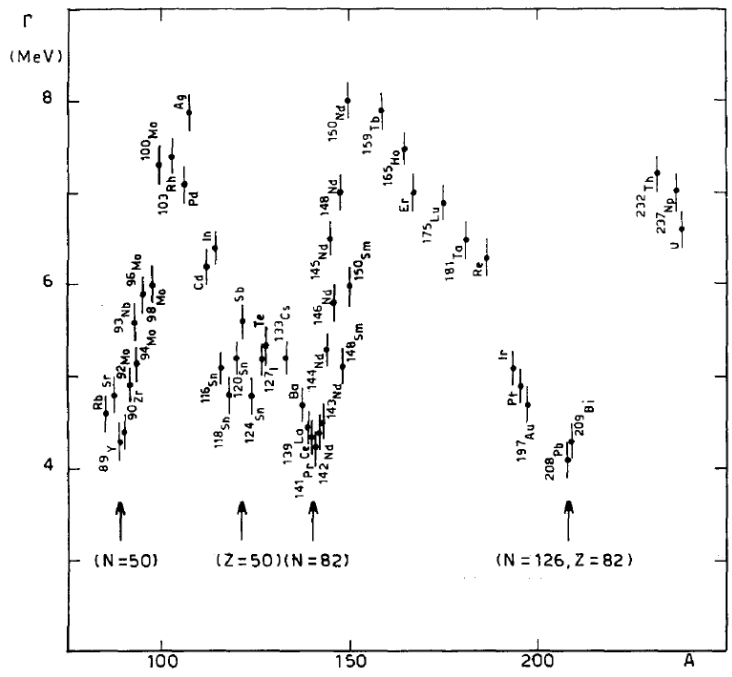

Figure 2.3: Width of the IVGDR (built on the ground state) as a funtion of the mass number A [41].

decay in the IVGDR energy range also occurs in the decay of nuclei produced in a fusion reaction [39]. Figure 2.4 shows the first results (Newton, 1981 [43]), observed for the reaction ^{82}Se + ^{40}Ar.

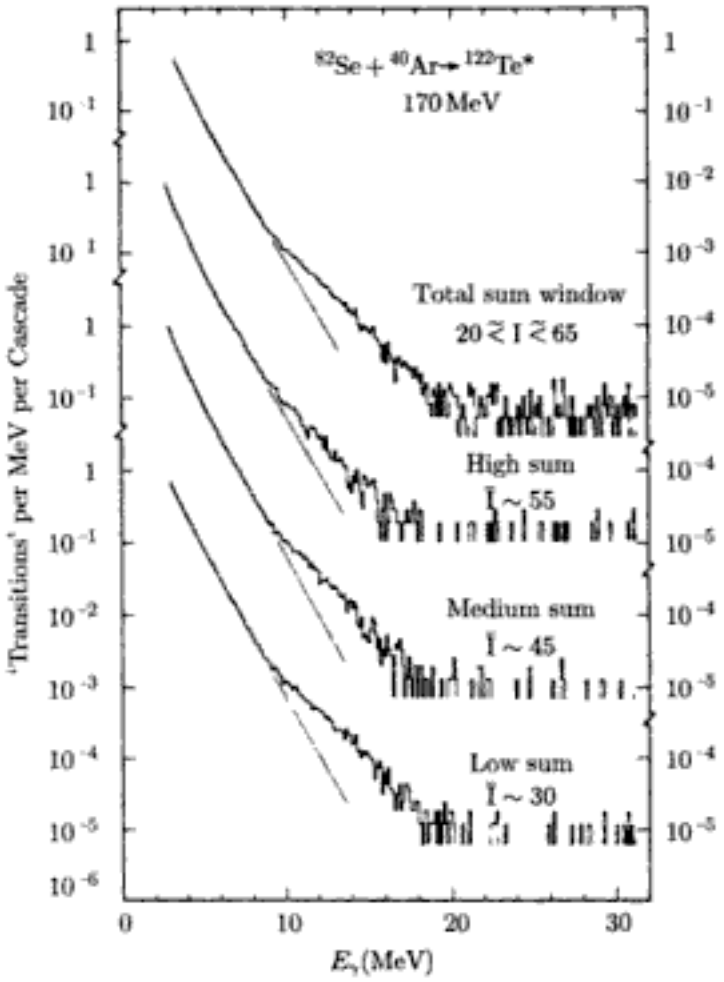

Figure 2.4: γ-ray spectra for different angular momentum (indicated with I) in the fusion-evaporation reaction ^{82}Se + ^{40}Ar [43]. Above ~ 10 MeV the IVGDR structure is clearly visible.

The hypothesis that the IVGDR can be built on an excited state of a nuclear system was firstly suggested in 1955 by Brink [44] and then became the so-called *Brink-Axel hypothesis* [45]. According to this assumption, a giant resonance (not only the IVGDR) can be built on each nuclear state and its overall characteristics do not depend on the micro-

scopical structure but on the bulk properties of the system. Indeed, as the experimental data confirm (see for example Fig. 2.5), the whole structure, as well as the centroid energy of the IVGDR built on the excited states, is the same as the ones on the ground state [46], [39].

According to this idea, during the years, the IVGDR has been investigated in hot compound nuclei, in different condition of excitation energy E^*, nuclear temperature T and angular momentum J [43, 46–52]. The experimental results confirm that the centroid energy does not change with the excitation energy, while the total IVGDR width depends on T and J and, in particular, it increases with them ([52, 53]), as discussed at the end of this section.

IVGDR γ-decay: statistical model

It is worth to remember that the statistical description of a compound nucleus is valid under the assumption that the system has reached the thermal equilibrium before its evaporation and that the detailed balance is valid (see Appendix A).
Under this condition and following the Brink-Axel hypothesis, the energy dependence of the γ-emission can be written as:

$$\sigma_{decay}(E_\gamma) = \sigma_{abs}(E_\gamma)\frac{\rho(E^*_{fin})}{\rho(E^*_{in})} = \sigma_{abs} exp(-E_\gamma/T), \tag{2.15}$$

where σ_{abs} is the absorption cross section at T=0, ρ is the level density, E_γ is the energy of the γ-transition and T the average nuclear temperature. If the excitation energy E^* is higher than the particle binding energy, the γ-decay process is in competition with the decay of particles, mainly neutrons in the case of stable nuclei. At the thermal equilibrium, the neutron evaporation cross section can be parametrized using the Maxwell-Boltzman distribution:

$$\sigma_n \sim T^2 exp\left[(E_n - B_n)/T\right] \sim T^2 exp\left[-B_n/T\right], \tag{2.16}$$

being B_n the neutron binding energy. The branching ratio between γ and *n* decay is therefore:

$$\frac{\sigma_\gamma}{\sigma_n} \sim \sigma_{abs} T^{-2} exp(-(E_\gamma - B_n)/T). \tag{2.17}$$

If $E_\gamma > B_n$ (the argument of the exponential in eq. 2.17 is <0), the emission probability for a high-energy γ-ray increases with T: the emission of high-energy γ-ray occurs preferably at high temperature, therefore in the first steps.
If $E_\gamma < B_n$ (the argument of the exponential in eq. 2.17 is >0), the γ-emission probability decreases with T: σ_γ is dominated by the last decay-steps, i.e. at low temperature.

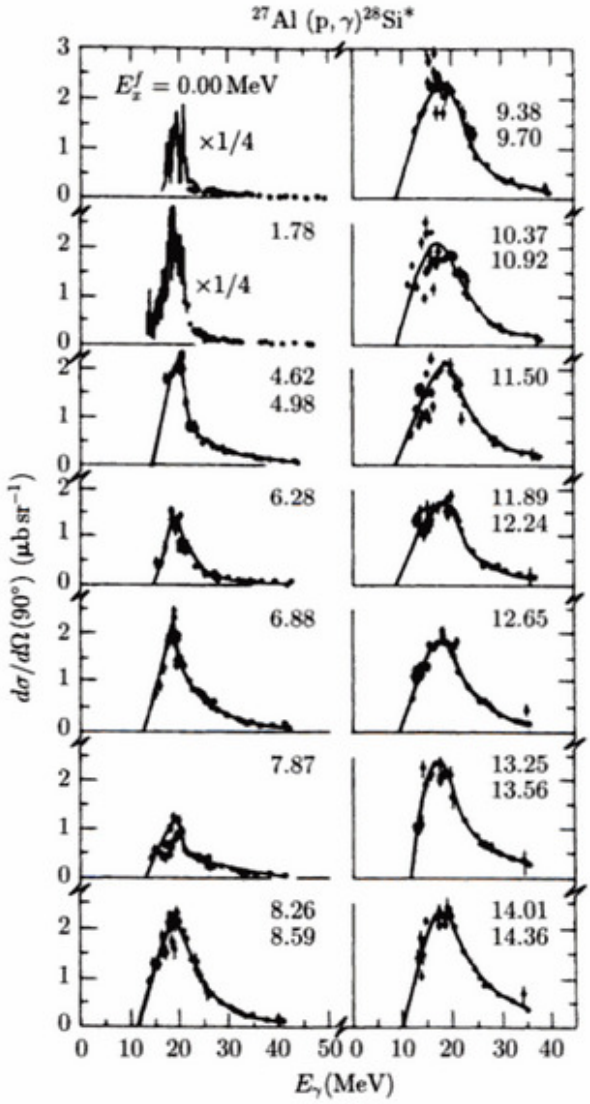

Figure 2.5: Cross section for ^{27}Al(p,γ)^{28}Si* to populate the ^{28}Si excited states defined by the excitation energies indicated. All the resonant excitation functions have a similar structure and the centroid energy of the resonances built on the excited states are the same as the ones on the ground state [46].

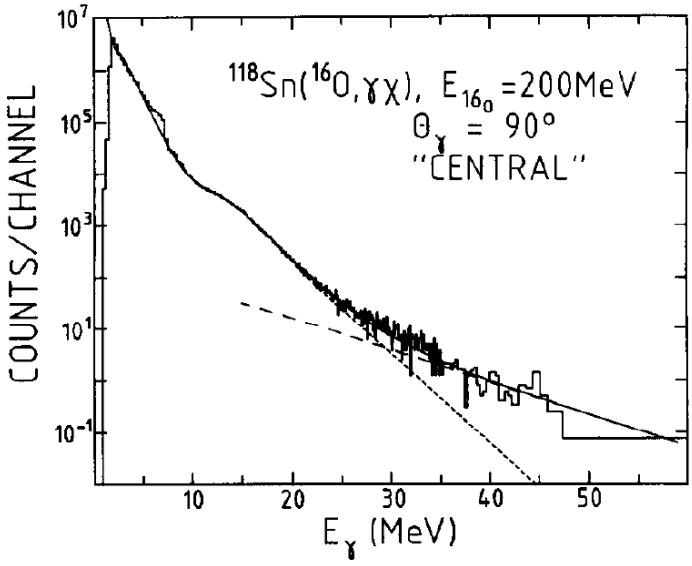

Figure 2.6: γ-ray spectrum from the fusion-evaporation reaction $^{16}O + ^{118}$ Sn with a beam energy of 200 MeV. The full line corresponds to a fit to the data obtained by the sum of the Bremsstrahlung component and the CN decay component (long dashed line and short dashed line respectively) [54].

Fig. 2.6 shows a typical γ-ray spectrum from a fusion-evaporation reaction [54].

As previously mentioned, when the IVGDR is built on an excited state, its total width Γ is larger than the one associated to a IVGDR built on the ground state and, in particular Γ increases with T and J [52, 53, 55]. The IVGDR Γ broadening is mainly due to the fact that the nucleus experiences a continuous range of deformations and space orientation as described by the Thermal Fluctuation Model (TFM) [50]. Each deformation is described by the couple of parameters (β,γ) and populated with a probability $P(\beta,\gamma)$:

$$P(\beta,\gamma) \approx exp(-F(\beta,\gamma,T)/T), \tag{2.18}$$

depending on the associated free energy F. The resulting strength function is a superposition of many Lorentzian distribution, each one associated to a specific deformation:

$$\sigma(E) = \int \sum_{k=1}^{3} \sigma_k(E,\beta,\gamma)P(T,\beta,\gamma)\beta^4|\sin(3\gamma)|d\beta d\gamma \tag{2.19}$$

The value of the β parameter which corresponds to the minimum of the free energy, β_{eq},

is different from the average value $\langle\beta(J,T,A)\rangle$:

$$\langle\beta(J,T,A)\rangle \approx \int \beta P(T,\beta,\gamma)\beta^4|\sin(3\gamma)|d\beta d\gamma d\sin\theta \tag{2.20}$$

A quasi-linear relation between the average nuclear deformation $\langle\beta(J,T,A)\rangle$ and the increasing of the Lorentzian distribution FWHM used to reproduce the IVGDR spectrum has been proposed in [55] and plotted as the dashed line in Fig. 2.7.

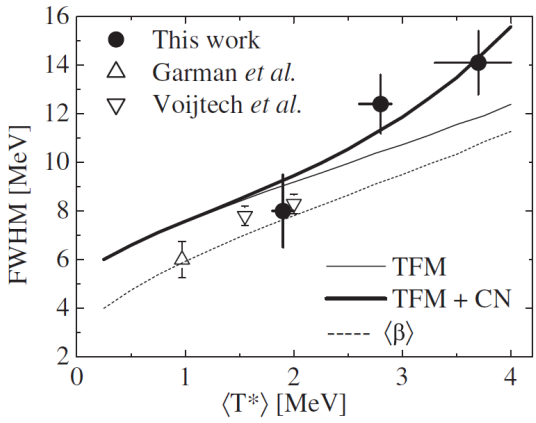

Figure 2.7: Comparison between measured and calculated FWHM of the IVGDR as a function of the nuclear temperature T [55]. The data are taken at $\langle J\rangle$ = 45 ħ (filled dots), $\langle J\rangle$ = 8-16 ħ (up-pointing triangle), $\langle J\rangle$ = 23-27 ħ (down-pointing triangle). The thin (thick) continuous line shows TFM calculations without (with) CN decay width, while the dashed line shows the average deformation β calculated with TFM.

A first parametrization of the IVGDR width dependence on temperature, angular momentum and mass has been obtained by Kusnezov et al. via a systematic study of the thermal fluctuation model [52]. Although it shows an increase of the IVGDR width with T, the model differs significantly from the experimental data at low temperatures ($T \leqslant 1.5$ MeV) [56]. In a more recent work [57] a new model, called Critical Temperature included Fluctuation Model (CTFM), was proposed, which is a modification of the TFM. The crucial point is that the IVGDR vibration itself induces, even at zero temperature, a quadrupole moment that cause the fluctuation of nuclear shape. It is therefore unlikely to feel the thermal fluctuations that are smaller than the IVGDR own intrinsic fluctuation. As a consequence, the experimental IVGDR width should remain nearly constant (at the ground state value Γ_{int}) up to a critical temperature value T_C and the effect of thermal fluctuations should become evident only when they become larger than the intrinsic ones [56].

The temperature and angular momentum dependences are parametrized as:

$$\Gamma(T, J = 0, A) = \Gamma_0(A) + c(A)\ln(T/T_C) + \Gamma_{int},$$
$$\Gamma(T, J, A) = \Gamma(T, J = 0, A)\left[L(\frac{J}{A^{5/6}})\right]^{7T_C/(T+3.3T_C)} \quad (2.21)$$

where Γ_{int} is usually adopted from the existing ground state GDR width systematics of nuclei, $c(A) \approx 8.45 - A/50$ and $L(\xi = \frac{J}{A^{5/6}})$ is a scaling function, also called reduced width Γ_{RED}, which can be approximately fitted by $L(\xi) = 1 + 1.8\left[1 + e^{(1.3-\xi)/0.2}\right]^{-1}$. The comparison between experimental Γ_{RED} data and theoretical calculations, perform using the CTFM model, is shown in Fig. 2.8.

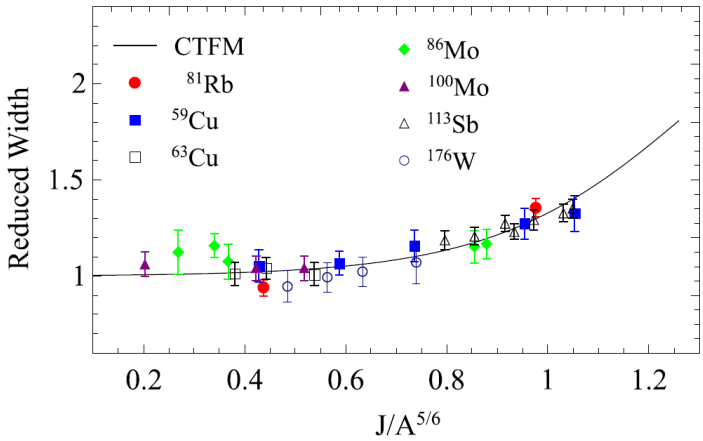

Figure 2.8: The IVGDR reduced width, Γ_{RED}, behaviour as a function of the parameter ξ, (see text). The experimental data are taken from [58] and references therein and [27]. The black curve corresponds to the $L(\xi)$ function in the CTFM theoretical model. Taken from [27].

2.3 The measurement: experimental technique and recent results

As previously asserted, to obtain informations about the Isospin mixing we need to study transitions which would be forbidden if the Isospin was a good quantum number to describe the nucleus. This is the case of β-transitions among nuclei with different isospin [59] or E1 transitions, and thus the γ-decay of the IVGDR, in self-conjugate nuclei [2, 3, 5, 60–64]. For the present work, we are interested in the latter.

We need to excite a IVGDR state in a I=0 configuration. A fusion evaporation reaction among two N=Z nuclei produces a N=Z compound nucleus in a I=0 state at a certain

temperature T. By measuring the γ-decay of the IVGDR, built on a CN state, and fitting such data with the statistical model (in which the formalism proposed by Harney, Richter and Weidenmüller, discussed in sec. 1.3.1, is included) it is possible to obtain the value of α^2, the mixing degree, and the Coulomb spreading width $\Gamma^{\downarrow}$ at the temperature value T.

This technique has been proposed firstly in [61] by Harakeh, who studied the γ emission from the hot nuclei $^{28}Si^*$ and $^{24}Mg^*$ populated using a fusion-evaporation reaction (see Fig. 2.9). The role of the E1 transition has been then exploited, during the years, by the Washington, Warsaw and Mumbai groups [62–64] to determine the Isospin mixing degree at high temperature for testing the restoration of the Isospin symmetry and by Milano group [2, 3] to study the temperature dependence of the phenomenon.
These experimental data, reported in Fig. 2.10, show a mass dependence (left panel) and a temperature dependence (right panel) but, anyway, their validity is limited by the error bar [21]. Moreover, there's no a systematic study of the same nucleus at different temperature values, that allows to clarify the α^2 temperature dependence and to have a comparison with the theoretical calculations (i.e. at zero temperature).

2.3.1 Isospin mixing from finite to zero temperature

By using the theoretical model of Sagawa, Bortignon and Coló ([4]), illustrated in 1.3.2, it is possible to extract the mixing probability α^2 for a nucleus at T=0, starting from (at least) two values of α^2 for the same nucleus at finite temperature. This has been the way proposed in the works of Ceruti, Corsi and Milano group to investigate the Isospin symmetry in the nucleus (N=Z=40) ^{80}Zr (see Fig. 2.11), the heaviest possible nucleus that can be produced using stable beams [2, 3, 27]. The mixing probability α^2, together with the Coulomb spreading width $\Gamma^{\downarrow}$, has been determined at T ~ 3 MeV in [2] ($\alpha^2_> = 1.3\% \pm 0.4\%$, $\Gamma^{\downarrow} = 10 \pm 3$ keV) and at T ~ 2 MeV in [3] ($\alpha^2_> = 4.6\% \pm 0.7\%$, $\Gamma^{\downarrow} = 12 \pm 3$ keV). The two results for the Coulomb spreading width are in good agreement, that confirms how this parameter corresponds to an intrinsic property of the system and does not strongly depend on its excitation energy [27]. Using eq. 1.20, reminding that $\Gamma^{\downarrow}$ is physically equivalent to $\Gamma^{\downarrow}_{IAS}$ (as discussed in sec. 1.3.2), the Isospin mixing probability at zero temperature has been extracted for the nucleus ^{80}Zr. This value, $\alpha^2_>(T = 0) = 4.6\% \pm 0.9\%$, is in good agreement with the theoretical prediction reported in [7], which represents an evidence for the validity of the theoretical model. In Fig. 2.12 the $\alpha^2_>(T)$ values obtained in these works are reported, together with the theoretical prediction. Furthermore, in [3] the $\alpha^2_>(T = 0)$ has been used to determine, for the first time, the δ_C correction parameter for the calculation of the CKM matrix element V_{ud}. This has been possible trough the Auerbach parametrization of δ_C (reported in sec. 1.4, eq. 1.24),

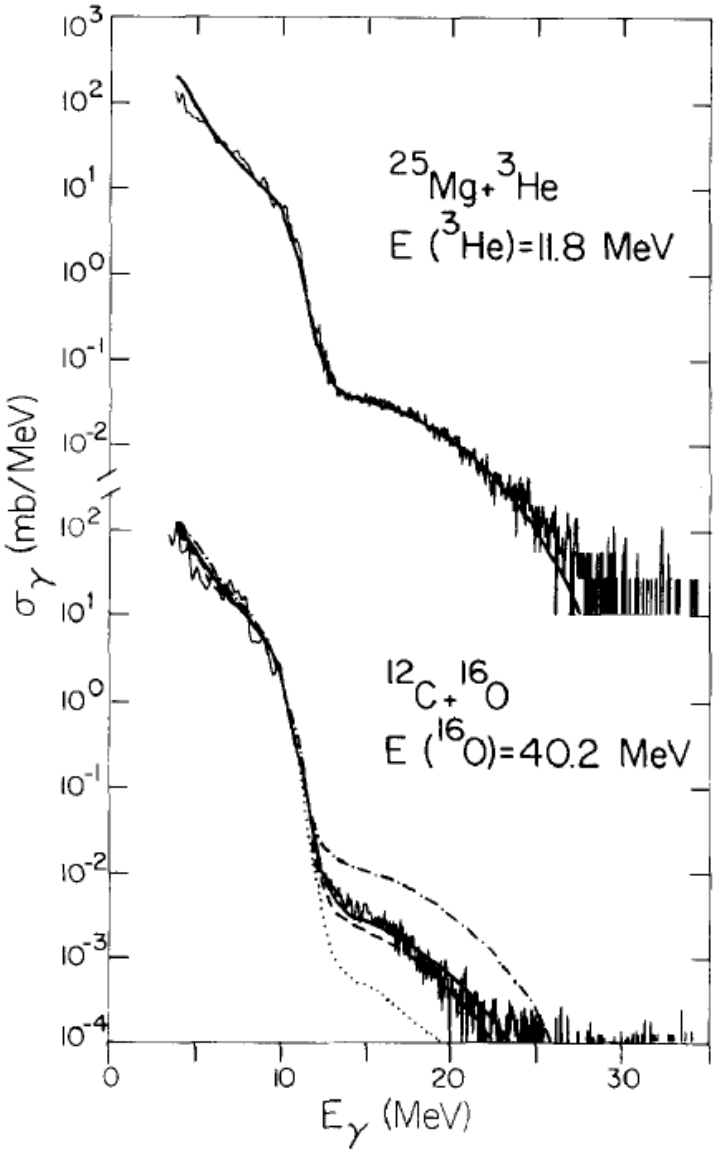

Figure 2.9: γ-ray spectra for the reactions ^{25}Mg + ^{3}He (I$\neq$0, top panel) and ^{12}C + ^{16}O (I=0, bottom panel). In the latter the Isospin mixing effect is evident. The dot-dashed curve corresponds to a full mixing, the dot curve to absence of mixing, while the dashed curve is the best fit to the experimental data [61].

which outlines its explicit relation with α^2. The result is consistent with the trend of the theoretical predictions and with an existing experimental result for another nucleus in

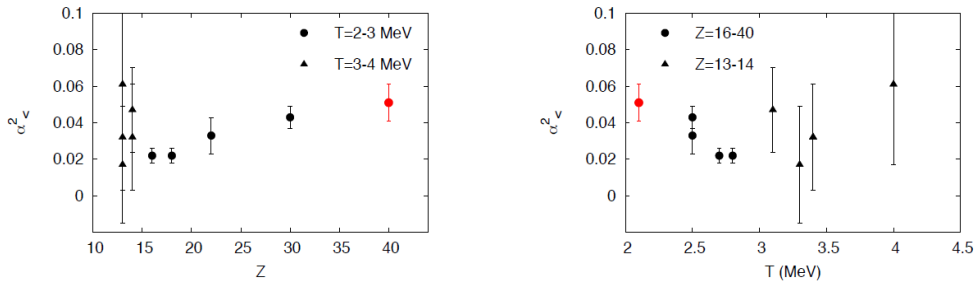

Figure 2.10: Systematics of $\alpha^2_<$ measured via GDR decay of the hot CN with Z=13-14 and T=3-4 MeV (triangles) and with Z=16-40 and T=2-3 MeV (dots). The left panel displays the dependence of $\alpha^2_<$ on atomic number Z, the right panel its dependence on nuclear temperature T. Taken from [65].

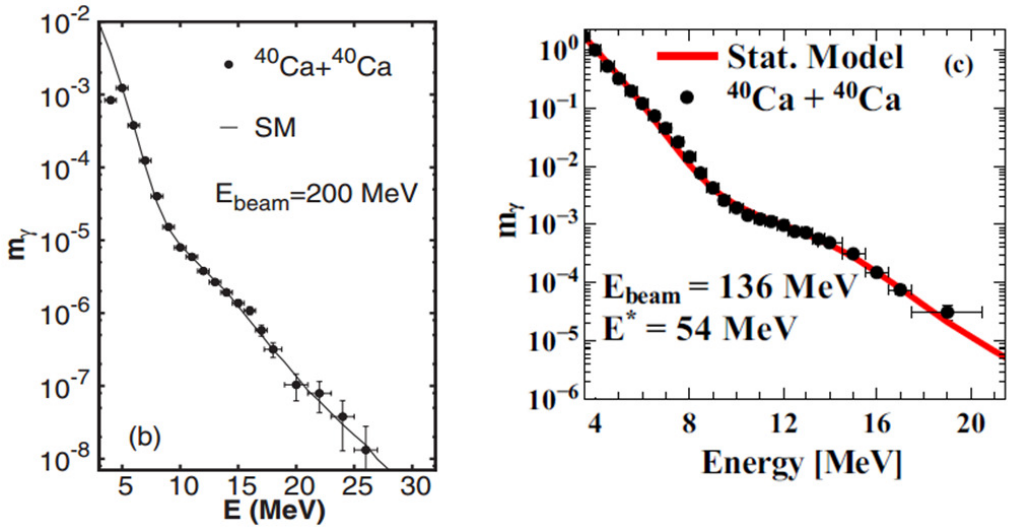

Figure 2.11: γ-ray spectra of ^{80}Zr at T ~ 3 MeV [2] (left panel) and at T ~ 2 MeV [3] (right panel): comparison between experimental data (the black dots) and statistical model calculation (the lines).

the same mass region (see Fig. 2.13).

In this thesis work a new experiment, performed by Milano group to investigate the Isospin symmetry in the nucleus ^{60}Zn via the γ-decay of the IVGDR, is presented. The final goal of this experiment will be to extract, as described above, the mixing probability at zero temperature and to obtain the value of δ_C parameter for ^{60}Zn. Such nucleus is interesting since, in its mass region, δ_C is expected to have a sudden increase (see Fig. 2.13). Additionally, in that mass region, other experimental results for the Isospin mixing are

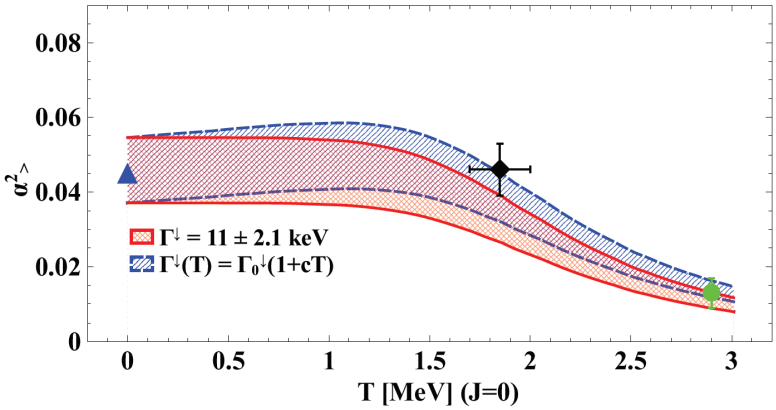

Figure 2.12: The Isospin mixing probability $\alpha^2_>$ as a function of temperature T obtained with the procedure of [4]. The red band correspond to $\Gamma^\downarrow_> = 11.0 \pm 2.1 keV$ (the average value between the $\Gamma^\downarrow_>$ obtained in [2] and [3]) constant with T. For the blue band, $\Gamma^\downarrow_>$ is assumed to vary slightly and linearly with T. the blu traingle is the theoretical value at T=0 [7], the green circle is the datum from [2] and the black diamond is obtained from [3]. Taken from [3].

present in literature, although they have been obtained with different experimental techniques [5, 6]. The determination of the Isospin mixing in ^{60}Zn at zero temperature will therefore provide both a validation of our experimental technique (through the comparison to the existent experimental data in the same mass region) and a validation of the theoretical model of Sagawa, Coló and Bortignon, by means of the comparison with the theoretical prediction [7].

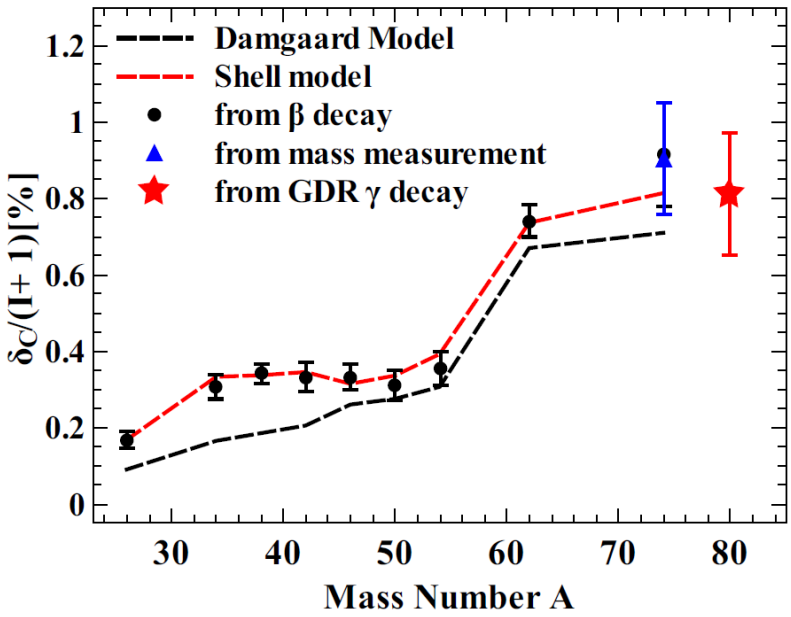

Figure 2.13: The Isospin symmetry breaking correction parameter δ_C as a function of the mass number A [3]. The dashed black lines refers to the Damgaard model prediction [37]. The dashed red lined refers to shell-model with Saxon-Woods radial wave function prediction [38]. The black circles and the blu triangle are the experimental points obtained from β-decay ([6]) and mass measurement ([36]) respectively. The red stars refers to [3]. It is to be noted that the quantity plotted on y-axis is $\delta_C/(I+1)$ since β-decay measurements are obtained for I=1, while the one for ^{80}Zr for I=0.

Part II

Development of dedicated detectors

CHAPTER 3

The PARIS project

In this chapter we will give a general overview about the PARIS project. First of all, we will have to identify the reason who led to create the PARIS collaboration, then we will describe the core of this project: the PARIS array. Due to its high efficiency and high granularity, this array can serve the dual purpose to be an high energy γ-ray detector and a multiplicity filter. For this reason it represents a suitable system to investigate the Isospin mixing by measuring the γ-decay of IsoVector Giant Dipole Resonance.

3.1 Aims of PARIS Project

The PARIS (acronym for *Photon Array for studies with Radioactive Ion and Stable beams*) collaboration [66] was formed in 2006 with the purpose to develop and build an innovative γ-array. The requirement is that this system operate as an energy-spin spectrometer, a calorimeter for high energy photons and a medium-resolution γ-detector [8]. Such a device will allow to improve the detection efficiency of γ rays, which constitutes an important experimental probe to many physics topics.

3.1.1 Overview on Physics Cases

Nuclear reactions induced by radioactive beams will be available in several facilities. This may lead to increase our understanding in the behaviour of the atomic nucleus.

Through fusion-evaporation reactions involving radioactive beams, the population of exotic nuclei under extreme condition of excitation energy and/or angular momentum can be reached. This will be of great benefit for the study of single-particle and collective phenomena at finite temperature, such as the Giant Dipole Resonance or exotic shape changes induced by fast rotation [8].
Moreover, the investigation on neutron-rich nuclei either via deep-inelastic or transfer mechanism will be permitted by means of very intense stable beams. Nuclear structure at the drip line can therefore be studied to give the strongest constraints on the interactions that govern nuclear matter far from stability. Probe of all these physics topics are energy, multiplicity and angular distribution of γ-rays de-exciting the nuclei of interest.

In order to achieve this ambitious physics program, some technical problems are to be overcome, such as events extraction from a high background due, for example, to the activity of the beam. A new generation of detection arrays is therefore necessary; PARIS belong to this generation [8].

3.2 PARIS Array

"PARIS is a large array of phoswich detectors expected to measure γ-rays over a wide range of energy from few hundred of keV to 40 MeV. It is envisaged to serve the dual purpose of a high-energy γ-ray spectrometer and a spin-spectrometer, capable of determining the multiplicity of low energy (~100 keV to few MeV) discrete γ rays associated with a specific reaction." [67]
In order to satisfy the requirement, PARIS array needs to be [68]:

- as efficient as possible in a wide energy range (up to 40 MeV),
- with a good energy resolution,
- with a sub-nanosecond time resolution to discriminate γ-rays against neutrons,
- with a high granularity,
- able to support a high counting rate (50 kHz).

The final structure of PARIS consist on an array of 216 phoswich detectors (see Fig. 3.1). In the original project, the PARIS phoswich consists of a cube (2″x2″x2″) of Lanthanum Bromide ($LaBr_3$:Ce) optically coupled to a parallelepiped (2″x2″x6″) of Sodium Iodide (NaI:Tl) of matching cross section. This is the phoswich we consider in the present work. Every detector is coupled with a 2″ diameter cylindrical photomultiplier tube (PMT), which collects the light generated in both the two crystals. A complete phoswich consists of a $LaBr_3$:Ce crystal, backed by a NaI:Tl scintillator, hermetically sealed in a single

aluminium can with a glass window to couple to the photomultiplier tube, as shown in Fig. 3.2 [69].

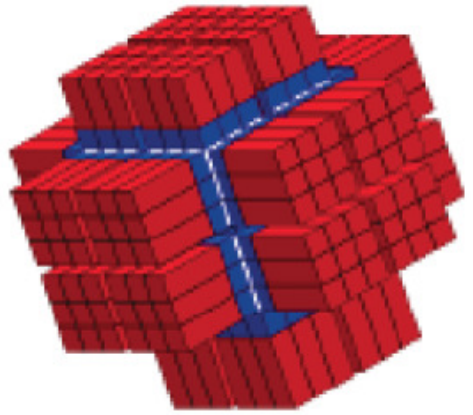

Figure 3.1: The complete PARIS array: 216 phoswich detectors in a (possible) cubic configuration. [70]

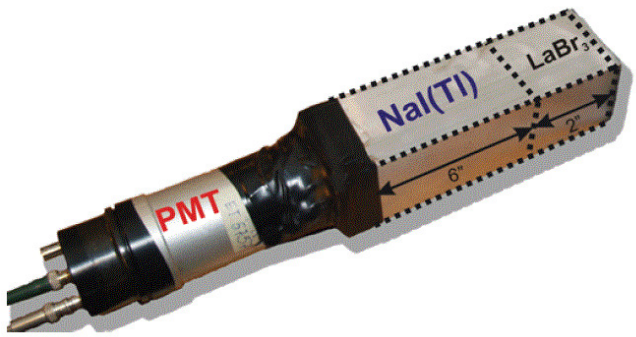

Figure 3.2: The $LaBr_3$:Ce(Ce)-NaI:Tl phoswich detector [71].

$LaBr_3$:Ce is a relatively new scintillator with a large potential in γ-rays spectroscopy. Indeed, it has a high efficiency, good energy resolution, excellent time resolution ($<$1 ns, depending on the size of the detector) and a high light output (63000 photons/MeV [72]). The decay times are generally quick with the fast components having a value between 15 and 66 ns depending on the Ce^{3+} concentration [73].
NaI:Tl is one of the most used scintillation detector; its best energy resolution at 662 keV is around 6-7 %, it has a good efficiency, a high light output (38000 photons/MeV), and a decay time of about 0.25 μs [74][73]. The relatively low production cost and the great

diffusion of this material make its production easier than many other kind of scintillator. A key aspect is the photomultiplier choice. PARIS collaboration identified the R7723-100 PM tube from Hamamatsu company as the best solution in order to satisfy the physics requirement. It has a photocathode efficiency of 35% and a transit time spread of 1.2 ns; the optimum gain value would be around $3{\cdot}10^4$ [71]. Clearly, the coupling between a cylindrical photomultiplier tube and a square scintillator implies a geometric loss in the light collection of about 20%. The effect is a slight deterioration in the energy resolution that, at 1 MeV, is estimated to be around 0.3-0.4%.

Each of the two different parts of PARIS phoswich have a specific function: the $LaBr_3$:Ce shell will provide timing and γ-rays multiplicity, whereas NaI:Tl is used for detection of high energy γ-rays and may acts as a Compton suppressor. Through the add-back technique, summing up the informations from both shells, it is possible to reconstruct the number and the total energy of incident photons.
Despite its self-activity due to the ^{138}La isotope presence in the crystal (0,09 %), $LaBr_3$:Ce crystal has superior performances than NaI:Tl. However, because of the high cost of $LaBr_3$ scintillators, a phoswich "is likely to be more cost effective for the use in the new high efficiency calorimeters" [73].

Nine phoswich detectors are combined together in a square close packed geometry, forming a PARIS cluster. To give an idea about the performances, Fig. 3.3 shows the results of efficiency and energy resolution simulations, performed using Geant4 code [75, 76], for a cluster.

The project is being carried out in different phases. During the first phase, one cluster (PARIS prototype) was constructed; the second and the third phases will be realized with the completion of respectively 4 cluster (PARIS demonstrator) and 12 cluster. At the end, in it's finite configuration, PARIS array will be composed by 24 cluster, covering 4π solid angle around the target [69]. Each consecutive phase will be realized only if the preceding one was validated by test measurements.
In Fig. 3.4 a schematic idea of the phases described above is depicted.

3.2.1 Phoswich Detectors

A phoswich, literally "phosphor sandwich", is a scintillation detection system consisting of two or more different scintillators, with dissimilar pulse line shape characteristic, optically coupled to each other and to a common photomultiplier tube [74]. The scintillators are chosen to have different decay times. In this way the shape of the output pulse from the PM tube depends on the relative contribution of scintillation light from the two scintillators. In most application, this difference in the pulse shape is used to discriminate events occurred in only one scintillators from those occured in both. Sodium Iodide

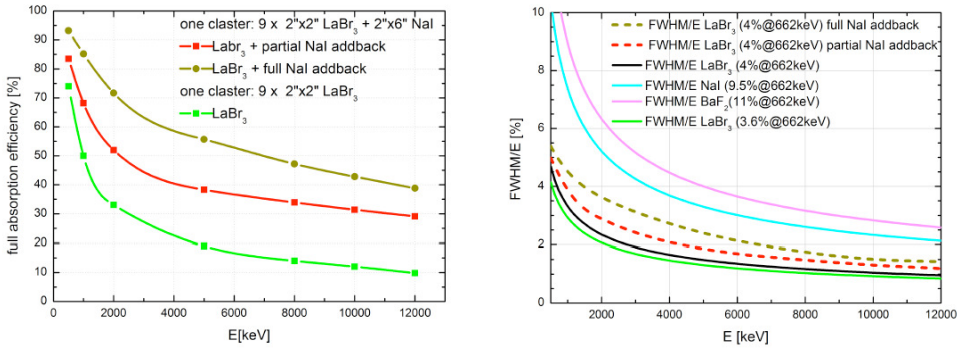

Figure 3.3: Left panel: simulations of relative photo-peak efficiency (when γ-rays were shining only on the central detector of the cluster) for one cluster made of 9 phoswiches after a full add-back procedure and a partial add-back (i.e. requiring always a $LaBr_3$:Ce signal to be present). For comparison, the efficiency for a case of a cluster made only with 9 $LaBr_3$:Ce 2″x2″x2″ crystals is also reported. Right panel: simulation of energy resolution for a cluster made of 9 LaBr−3:Ce crystals (with 3.6% and 4.0% resolution at 661 keV), cluster made of 9 NaI:Tl crystals and the resolution resulting from the add-back process (full and partial). For comparison, the energy resolution of large BaF2 crystals from the HECTOR array is reported. The simulations have been performed using Geant4 code [75, 76]. [70]

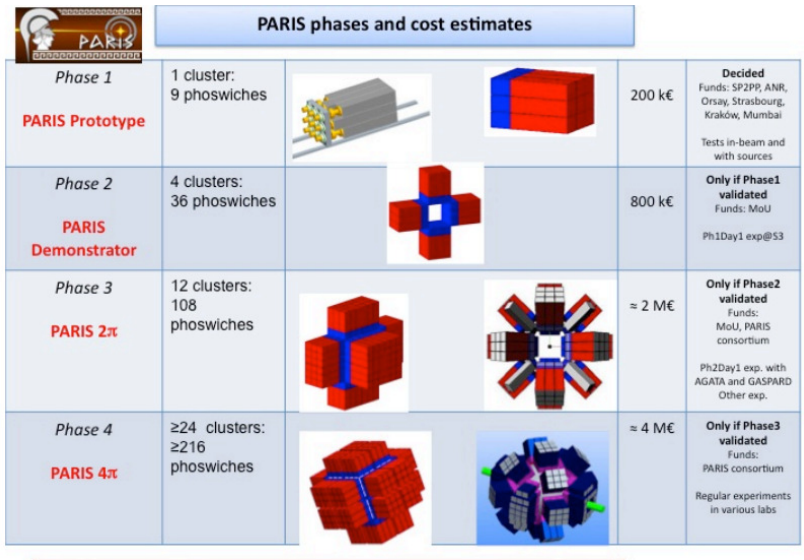

Figure 3.4: Schematic representation of the preliminary roadmap for the construction of the PARIS array. [70]

and Cesium Iodide are a typical combination of scintillators, due to their difference in the decay time (0.23 versus 0.68+3.34). Therefore pulses arising from only one crystal are easily distinguished from those with both components using the pulse shape discrimination method. Alternatively, separate electronic pulses may be derived from the PM tube signal [77]. Independent measurements of the energy deposited in each scintillator can be obtained without the need for a second PMT tube. A phoswich composed by a fast thin scintillator backed by a thick scintillator allows to simultaneously measure dE/dx and E for particles penetrating the detector [77].

An example of an existing phoswich detector is CEPA4 (CALIFA Endcap Phoswich Array), used for the simultaneous detection of high-energy protons and γ-rays from nuclear reactions with a reasonably good energy resolution [78]. Its prototype consists of four individual closely packed scintillator detectors, each one made of 4 cm of $LaBr_3$:Ce and 6 cm of $LaCl_3$:Ce optically coupled and with a common readout.

The innovative phoswich concept gives, ideally, the great advantage to fulfil the PARIS Physics cases and is, in addition, a relatively economic solution.

3.3 State of art

In 2015, despite the progress of the PARIS project, proven also by a number of proposals with PARIS prepared and approved, the main hindrance to finalize the PARIS Demonstrator (4 clusters) and the following phases has been the delay in the production and delivery of the phoswiches. 14 phoswich detectors, less than 2 clusters, were operational. Four more detectors had been returned to Saint Gobain company, the only manufacturer of $LaBr_3$:Ce-NaI:Tl phoswich on the market, because of ageing problems: a visible yellow crack appeared around the junction between $LaBr_3$:Ce and NaI:Tl, associated with deterioration of the energy resolution. The ageing appeared between 6 months and 1 year after the phoswich production.
In September 2015, Saint Gobain company sent information that it was decided to stop the production of phoswiches with the original design ($LaBr_3$:Ce and NaI directly coupled to each other) and not resume it in the future, since it was not able to find the reasons for this ageing phenomenon. Instead, the company would have focused on finalizing the production of the prototype of a phoswich with a new-proposed design having the two crystals components hermetically sealed and adding a quartz window between them. Two of this kind of phoswich are operational at the present time. Their energy resolution for the $LaBr_3$:Ce component, communicated by the Saint Gobain company, is $\sim$ 4.1% at 661.7 keV [79].

Simultaneously, the PARIS collaboration decided to start an R&D work on alternative solutions. One of the proposed ideas was to keep the original concept, two separate

layers of detectors: $LaBr_3$, read out by a Silicon photomultiplier (SiPM), and NaI:Tl, read out by a standard PMT. The groups of York, Krakow and Milano performed, in June 2015, the first test of a cubic 2"x2"x2" $LaBr_3$:Ce crystal coupled to an array of SiPMTs. The use of SiPM crystals coupled to a $LaBr_3$:Ce crystal has also been recently test in Milano [80].
In addition, the collaboration endorsed plans to test another solution: a new phoswich combination, $CeBr_3$-NaI:Tl, as an alternative to $LaBr_3$:Ce-NaI:Tl. The prototype of a $CeBr_3$-NaI:Tl has been prepared by Scionix company (see Fig. 3.5) and the test did not show, at the moment, any problems concerning the energy resolution and the ageing. The energy resolution values communicated by Scionix company to the PARIS collaboration are comparable with the ones associated to the $LaBr_3$:Ce-NaI:Tl phoswich: $<5\%$ for the $CeBr_3$ crystal and $<7.5\%$ for the NaI:Tl one at 661.7 keV [81].

At the moment the latter solution seems to be the most promising one. A new cluster of 9 phoswiches is now operational: it is composed by 7 $CeBr_3$-NaI:Tl detectors and 2 $LaBr_3$:Ce-NaI:Tl ones with the quartz window between the two crystals ($LaBr_3$:Ce and NaI:Tl). This cluster is being used, together with the $LaBr_3$:Ce-NaI:Tl one, for its first experimental campaign, at GANIL Laboratory (Caen, France). The first experiment, which concerns lifetime measurements of excited states in neutron-rich C and O isotopes [82], has been performed in July 2017.

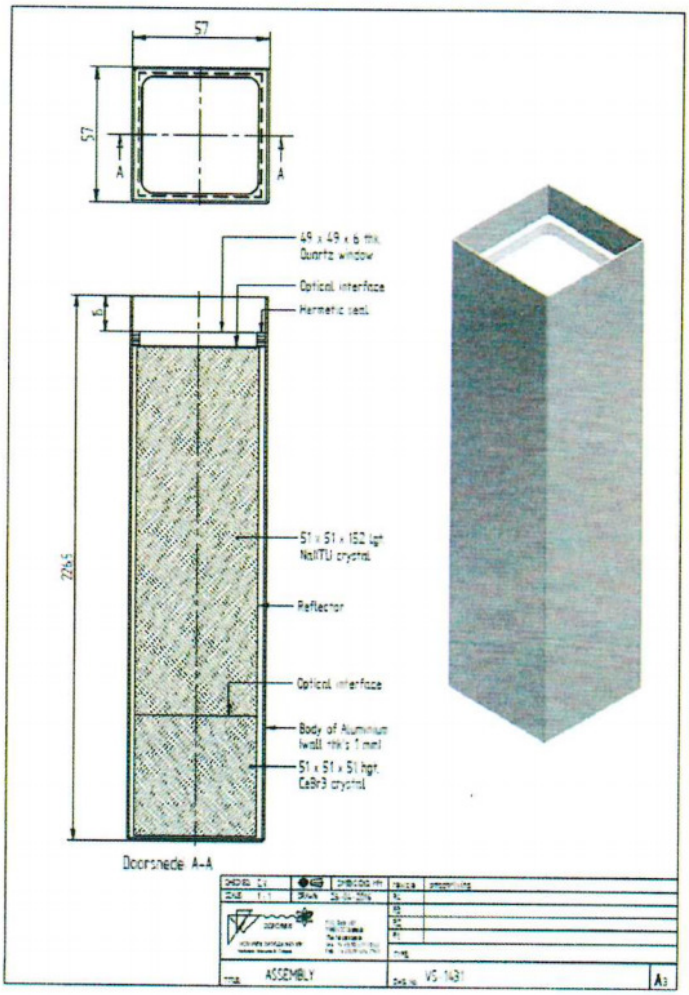

Figure 3.5: Technical details of the $CeBr_3$-NaI:Tl phoswich scintillation crystal for PARIS [81].

CHAPTER 4

PARIS Prototype characterization

Aim of this chapter is the analysis of the first PARIS prototype performances. At first the general properties of the PARIS phoswich will be illustrated and then two characterization tests will be presented. The first one, an in-beam test, took place at the ELBE bremsstrahlung facility (Dresden, DE) with the intent to study the cluster response to high-energy γ-rays and the time response in a high γ-ray background environment. The second one, performed in Milano, was a source test to analyse the events distribution inside the cluster.
The analysis code was written in C++ using the scientific software framework ROOT [83].

4.1 Analysis of the $LaBr_3$:Ce-NaI:Tl phoswich signal

A γ-ray, which interacts in a phoswich, involves the production of an electronic signal whose shape depends on the time constants of the crystal in which the γ ray deposits its energy. Figure 4.1 shows the pulse shape measured for a $LaBr_3$:Ce event, for a NaI:Tl event and for an event where the γ ray deposited its energy in both crystals (which will be called "Compton" event). For a fixed amount of energy deposited in the crystal, the NaI:Tl signal is approximately 7 times smaller and 6 times longer than the $LaBr_3$:Ce one.

The "Compton" signal has an intermediate shape between the two "pure" signals. Using a ^{60}Co source, it is evident that, for a single phoswich, the sum between the pulses relative to a 1332.5 keV Full Energy Peak (F.E.P.) event in $LaBr_3$:Ce and a 1173.2 keV F.E.P. event in NaI:Tl is, as it must be, identical to the pulse measured for the rare case in which, in the same event, a 1332.5 keV was fully stopped in $LaBr_3$:Ce and the other coincident ^{60}Co γ-ray of 1173.2 keV was fully stopped in NaI:Tl (see Fig. 4.2). The difference between the integrals of the two pulses in Fig. 4.2, indeed, is less then 2%. This guarantees the linearity of the phoswich system and allows to perform the add-back process and to use the "Compton" information. The first step of the analysis of a phoswich is to discriminate where the interaction occur. In our case, the discrimination method is provided by a dedicated NIM module, the so called "PARISPro" that we will describe in detail in sec. 4.2.4. It supplies two analogue shaped signals, one proportional to the amplitude and the other to the integral of the anode signal, which are sent to a peak sensing ADC. The identification technique we use is based on the 2D analysis, the "Amplitude vs Integral" matrix, whose axes refers to the homonym signals. As an example, the matrix shown in Fig. 4.3, associated to a single detector, shows the data acquired during a calibration measurement performed with the PARIS cluster (^{137}Cs and ^{60}Co sources). The two semi-diagonals in the matrix are related to events in which the energy is deposited in $LaBr_3$:Ce crystals or in NaI:Tl crystals only; in particular, the upper line refer to $LaBr_3$:Ce events, the bottom one to NaI:Tl. As the light yield in $LaBr_3$:Ce is larger than in NaI:Tl, the full energy peak events (indicated with circles in Fig. 4.3) in $LaBr_3$:Ce and in NaI:Tl do not have the same x value. Bounded by the two straight lines, we can see events in which the energy deposition is shared between the two scintillators of the same phoswich. The full energy peaks events in $LaBr_3$:Ce and NaI:Tl are connected by a diagonal ridge indicating those γ-rays which were fully stopped in one PARIS phoswich, but not in one crystal. It interesting to note that the matrix shows 'sum peak' events, i.e. events in which both the ^{60}Co γ-rays enter and interact in the phoswich. The two spots at x$\sim$450 and y$\sim$225 indicate the unlikely case where one ^{60}Co γ-ray is fully stopped in $LaBr_3$:Ce and the other penetrate the $LaBr_3$:Ce and it is fully stopped in the NaI:Tl crystal of the same phoswich.

In order to give an idea of the event distribution in a phoswich detector, Fig. 4.4 shows the results of a simulation performed by Michał Ciemała (Krakow group) in 2015, using GEANT4 code [75, 76]. The γ-radiation emitted by ^{60}Co (1173.2 keV and 1132.5 keV), ^{88}Y (898 keV and 1836 keV) and 9 MeV γ-rays have been simulated at a distance of 0.2 m from the cluster. In the simulation, the cluster detectors were wrapped with an Al can (1 mm thick). Considering only events characterized by γ-rays which release all the energy inside the detector (F.E.P.), the percentage occurred in $LaBr_3$ (red circles),

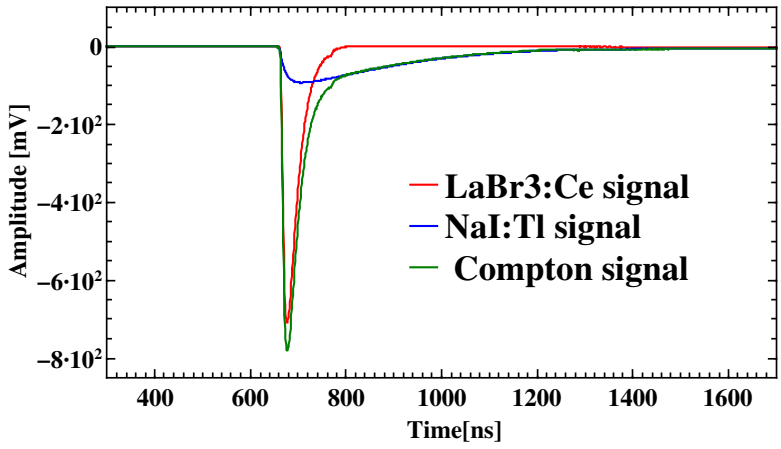

Figure 4.1: Pulse shapes measured in a PARIS phoswich: the red, blue and green pulses are referred to $LaBr_3$:Ce, NaI:Tl, and Compton signals respectively.

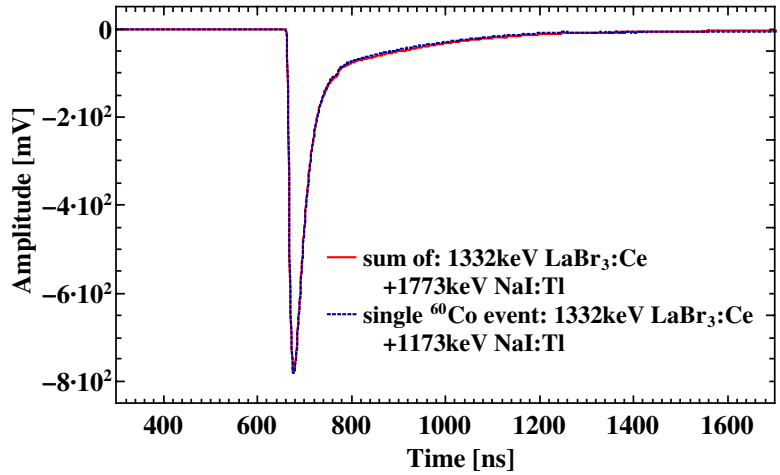

Figure 4.2: The figure shows the comparison between two signals: the first, in red, is obtained by summing a 1332.5 keV Full Energy Peak (F.E.P.) event in $LaBr_3$:Ce and a 1173.2 MeV F.E.P. event in NaI:Tl. The blue one is relative to an event in which a 1332.5 keV γ-ray from ^{60}Co has a F.E.P. in $LaBr_3$:Ce and the other (1173.2 keV) has a F.E.P. in NaI:Tl.

in NaI:Tl (blue squares) and in both, the Compton events, (green triangles) have been calculated. As one can see, the largest percentage of fully absorbed γ-rays is composed, over the whole energy range, by full energy peak events in $LaBr_3$, which is the first

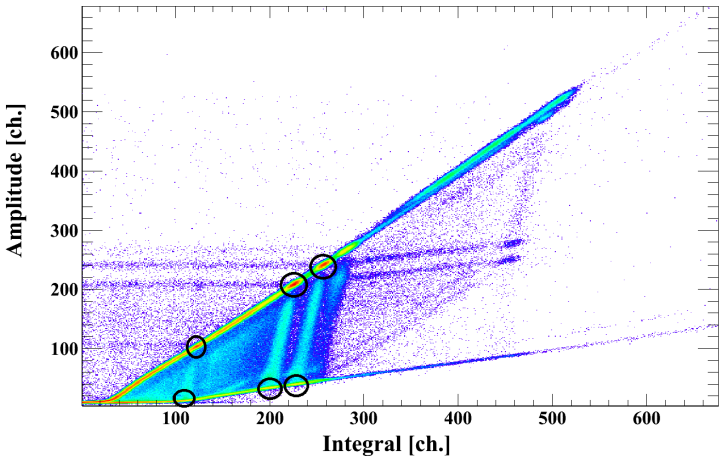

Figure 4.3: The "Amplitude vs Integral" matrix relative to detector in position 4 of the cluster (numbering in Fig. 4.10) when irradiated using ^{137}Cs and ^{60}Co sources. The upper line identifies the γ-rays which have deposited all their energy in the $LaBr_3$:Ce. The bottom line identifies the γ-rays which have deposited all their energy in the NaI:Tl. The γ-rays which have deposited their energy in both crystals are located between these two lines. The circles indicate the full energy peak events in $LaBr_3$:Ce and in NaI:Tl.

crystal that the radiation encounters. Such percentage, that is estimated to be around 90% at 1 MeV, slightly decreases with the γ-ray energy, being around 68% at 9 MeV. Above 9 MeV, it is expected to decrease as the energy increases. On the contrary, the NaI:Tl and the Compton percentages increase with the γ-energy, becoming significant above 1 MeV. The NaI:Tl percentage is expected to decrease for γ-ray of energy higher than ~10 MeV, as the Pair Production cross section increases with the gamma energy.

4.1.1 The energy spectrum

The energy spectrum of a PARIS phoswich cannot be produced by simply projecting on x-axis the "Amplitude vs Integral" matrix of Fig. 4.3. This is physically due to the different light yield of $LaBr_3$:Ce and NaI:Tl that leads an event of a specific energy to be associated to different axis channels, depending on the crystal in which the interaction occurs. As an example of this, Fig. 4.5 shows the projection on the x-axis of the "Amplitude vs Integral" matrix of Fig. 4.3.

Different solutions can be adopted to produce the energy spectrum. Starting from the "Amplitude vs Integral" matrix, two main approaches have been adopted by the different groups.

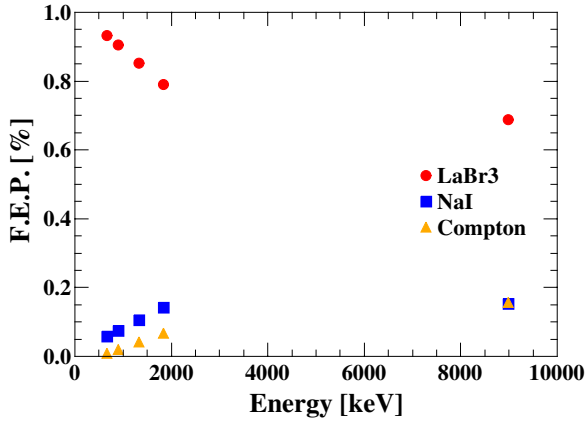

Figure 4.4: Simulated distributions of fully-absorbed events in the PARIS phoswich. The red circles, the blue squares and the yellow triangles refer to $LaBr_3$:Ce, NaI:Tl and Compton events respectively.

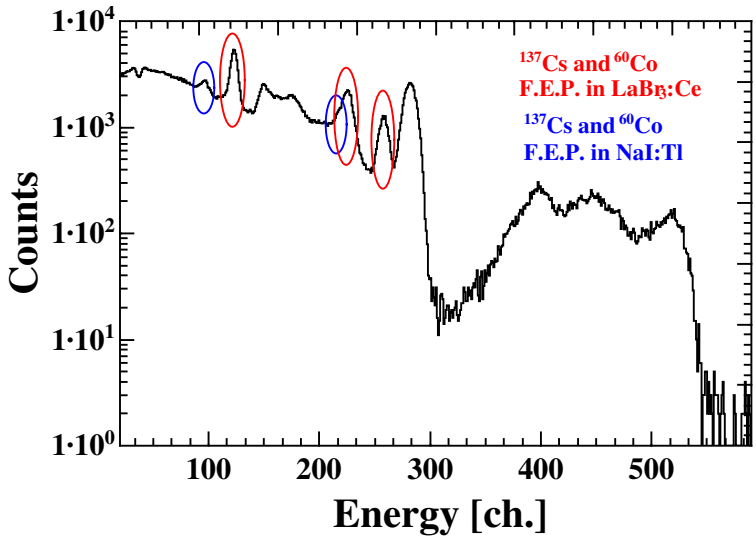

Figure 4.5: The projection on the x-axis of the "Amplitude vs Integral" matrix of Fig. 4.3. In this spectrum the 661.7 keV full energy peak in $LaBr_3$ and NaI:Tl are located at different channels: ~ 150 and ~ 105 respectively. In general same energy amount deposited in $LaBr_3$:Ce and NaI:Tl crystals is not associated to the same x channel.

One is based on the rotation, point by point, of the "Amplitude vs Integral" matrix, as in Fig. 4.6. The rotation angle is chosen in such a way that the F.E.P. corresponding to the same energy fall in the same x position, independently of the fact that the interaction oc-

curs in $LaBr_3$:Ce, NaI:Tl or in both. The energy spectrum is then built taking into account only the x-component in the new basis. Indeed, in this case, the x-axis value represents the energy deposited in the phoswhich.
Another possible approach is based on the fact that the events with full energy deposition in $LaBr_3$:Ce or NaI:Tl only form a line [84]. By the orthogonalisation process it is possible to change the basis to one where the energy deposited in $LaBr_3$:Ce and energy deposited in NaI:Tl part of the detector are used as versors (see Fig. 4.7) [84][85]. In this case, however the number of needed parameters is larger. This could result, due to uncertainties, in a more unstable method. The spectrum of the deposited energy E_{dep} is obtained by adding values of the x and y components (E_{dep} = x + y).

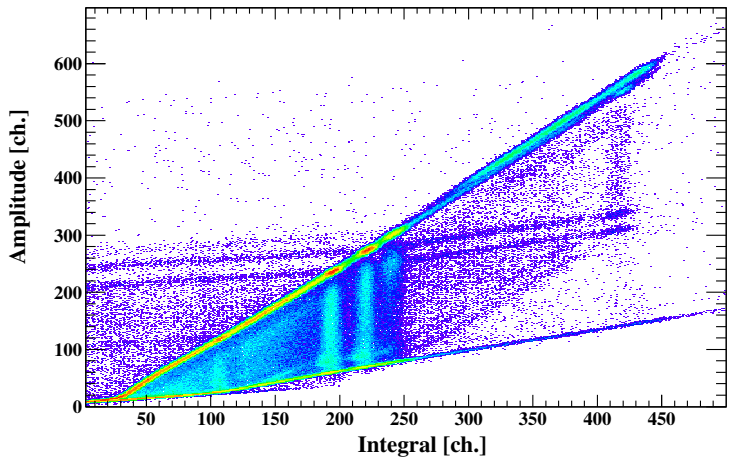

Figure 4.6: The rotated "Amplitude vs Integral" matrix relative to detector in position 4 (numbering in Fig. 4.10) of the cluster when irradiated using ^{137}Cs and ^{60}Co sources.

For this work, we use the first described method, based on the rotation. The definition of a rotation algorithm requires to extract the rotation angle from data, in such a way that the same "channel" corresponds to the same energy in $LaBr_3$:Ce and NaI:Tl (and so the straight lines in the Compton region are perpendicular to the x-axes). It is possible to deduce that the general rotation formula is:

$$tan\alpha = \frac{x_{LaBr_3} - x_{NaI}}{y_{LaBr_3} - y_{NaI}}, \tag{4.1}$$

where α is the rotation angle, and x_{LaBr_3}, x_{NaI} and y_{LaBr_3}, y_{NaI} are the coordinates (expressed in channels and corrected by any potential offset) of a Full Energy peak in $LaBr_3$:Ce and in NaI:Tl. Since $tan\alpha$ is extracted from experimental data, it is affected

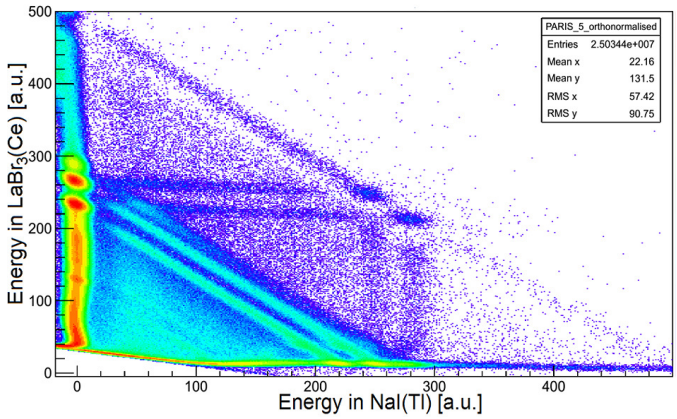

Figure 4.7: The orthogonalized "Amplitude vs Integral" matrix relative to the central detector of the cluster when irradiated using ^{137}Cs and ^{60}Co sources [84].

by error. This error shall be such as not to amplify the other errors. In other words, the applied transformation should not degrade the energy spectrum and, in particular, the energy resolution. Therefore, in order to evaluate the precision required in the determination of the rotation angle α, we calculated the FWHM at 1332.5 keV (as an example for $LaBr_3$:Ce crystal of detector #9) as a function of α. As one can see in Fig. 4.8, a total α variation of 0.02 rad ($\sim$ 10%) results in a variation on the FWHM at 1332.5 keV smaller than 4% (therefore only 40% of the error on the angle).

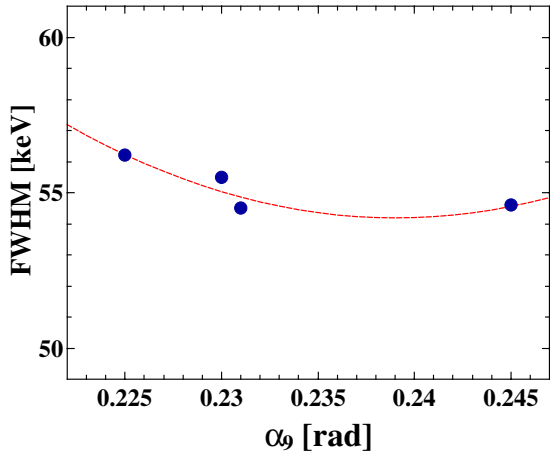

Figure 4.8: FWHM as a function of the rotation angle.

As an example of an energy spectrum, Fig. 4.9 shows the projection on the x-axis of the "Amplitude vs. Integral" matrix of Fig. 4.6.

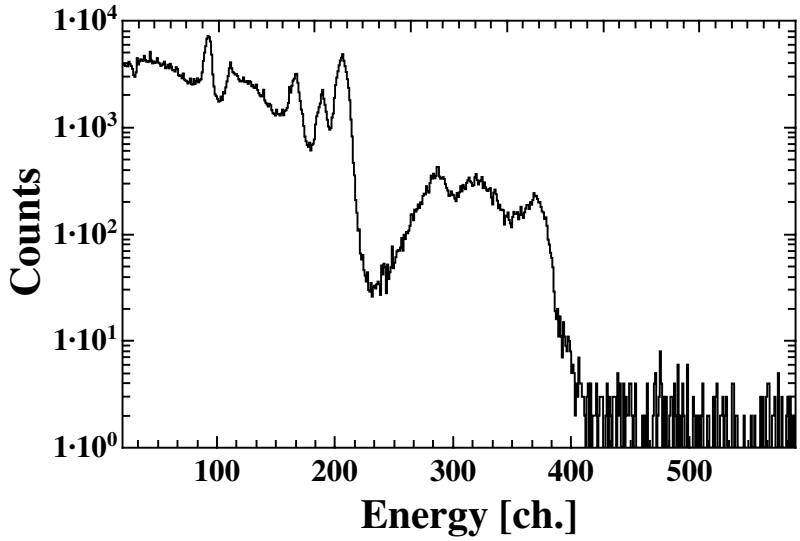

Figure 4.9: Energy spectrum of a PARIS detector, obtained by projecting on the x-axis the rotated "Amplitude vs Integral" matrix of Fig. 4.6.

4.2 ELBE Test

Until the end of 2012, only few phoswiches were delivered; five were fully tested in three different laboratory: Strasbourg, Orsay [86] and Krakow [71]. Signal analysis was conducted in a double way: both analogue and digital. We will only focus on the analogue mode, which is relevant for this work.

One of the firsts characterization test of the PARIS prototype, the first whole cluster, took place in December 2013 at the ELBE facility (Dresden, Germany). Fig. 4.10 is a picture of the cluster. The marked numbers refer to the detector positions. From now on, we will use this numbering. For each position number, the detector serial number, together with the high voltage values applied for the test, is listed in Tab. 4.1.

To study the detectors response to high-energy gamma-radiation it is not possible to use only radioactive sources, since these can emit gamma-rays up to only few MeV. A solution may be the production of high energy monochromatic gamma-rays from capture reactions using low-energy light-ions, proton and deuteron; a typical example of this kind of reaction is $^{11}B(p,\gamma)^{12}C$.

"The ELBE facility is ideally suited for characterizing γ-ray detectors up to high energy (16

Detector position	S/N	HV [V]
1	A5342	-1420
2	A3135	-1240
3	A4376	-1450
4	A4299	-1220
5	A4297	-1350
6	A4295	-1450
7	A3137	-1500
8	A4374	-1390
9	A4375	-1400

Table 4.1: Serial numbers S/N (column 2), and high voltage values (column 3) of cluster detectors. The position numbers, indicated in column 1, refer to Fig. 4.10.

MeV)" [87]. In order to measure detectors resolution, the generation of a nuclear resonance fluorescence (NRF) on a thick carbon target, combined with ^{11}B is needed. The beam time allocated to accomplish the complete characterization of the PARIS cluster was of two days.

Figure 4.10: The first PARIS cluster. The detectors position numbers are marked. Taken from [84].

4.2.1 NRF measurement

The process of nuclear resonance fluorescence consists of resonant excitation of definite states of a target nucleus by the absorption of electromagnetic radiation and the subsequent decay of these levels by re-emission of the equivalent radiation [88].

A typical effects of the high energy γ-rays interaction with a nucleus, which doesn't occur in other photon interaction, is the recoil of the nucleus, which involves an energy loss. Considering NRF reactions, therefore the emitted photon has not the same energy of the incident one (E_γ), and it is no longer able to excite a new resonance; it's energy is now:

$$\Delta E = E_\gamma - E_R, \tag{4.2}$$

where E_R is the recoil nucleus energy [89].
No tunable photon source, as in New SUBARU (Japan) and HigS (North Carolina) facilities, has been used in the present case to excite the nuclear resonance fluorescence. For this test it has been used the continuum electromagnetic spectrum from bremsstrahlung radiation produced using charged particles accelerators, in our case electrons.

4.2.2 ELBE Bremsstrahlung facility

The intense photon beam needed to realize the reaction described above was provided by the bremsstrahlung mechanism, generated by the slowing down of electrons, when they hit an appropriate material ("radiator") [90]. We used a 16 MeV electron beam of the superconductivity linear accelerator of ELBE. The bremsstrahlung photons were used to irradiate a target, made of ^{11}B-^{12}C. Fig. 4.11 shows a simplified picture of this process. An energy spectrum of a HPGe detector (used for monitoring), acquired during

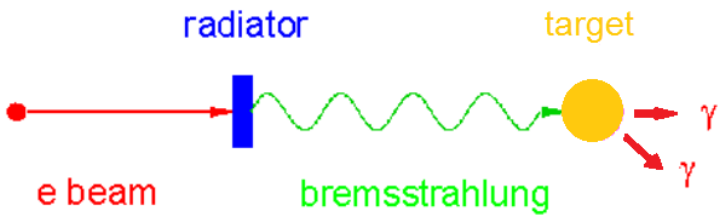

Figure 4.11: Sketch of Nuclear Resonance Fluorescence (NRF) experiment with bremsstrahlung. [88]

the experiment, is reported in Fig. 4.12: the γ-rays emitted from the ^{11}B-^{12}C target are visible.

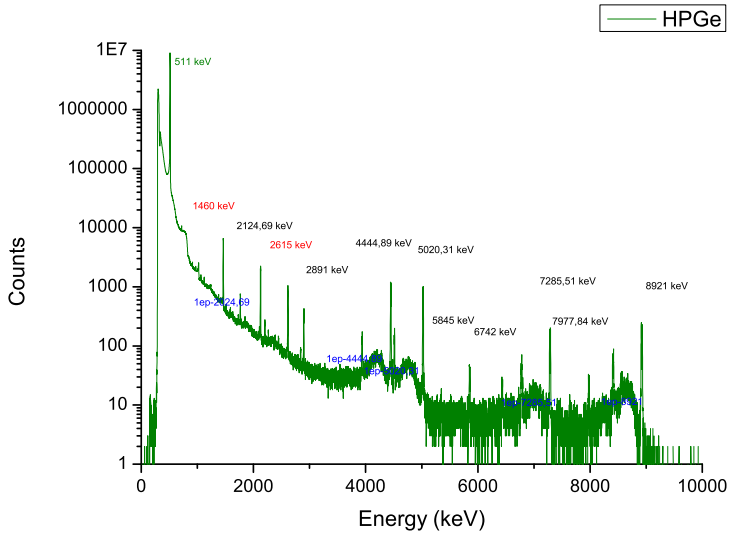

Figure 4.12: γ-ray energy spectrum of an HPGe detector (used for monitoring), acquired during the test. The γ-rays emitted from the ^{11}B-^{12}C target are marked in black (and their first escape peak energy in blue). The transitions written in red are relative to internal/natural radioactivity.

4.2.3 Experimental SET-UP

The set-up designed for ELBE NRF experiments with unpolarized and linearly polarized bremsstrahlung photon radiation is depicted in Fig. 4.13. At the beginning, a non-dispersive dipole/quadrupole magnetic system transports and focuses the electron beam onto a 25-50 mm Al bremsstrahlung radiator. The steering coils in front of the radiator control the polar and azimuthal incidence angles of the electron beam which can be changed in order to optimize the generation of linearly polarized photons. Passing through the radiator, the electrons are deflected by a 45° dipole magnet into a beam dump. Bremsstrahlung radiation is therefore collimated and directed onto the NRF target, located about 4 m downstream in the experimental hall. Such a geometrical configuration is designed to minimize background. Photons scattered off the NRF target, were detected by the PARIS prototype cluster (in Fig. 4.13 indicated with "CLUSTER detector"). The cluster was placed at 125° to the beam direction, at a distance of 35 cm. An important additional element, to be used as reference point during data analysis, is a HPGe detector, placed near and rotated by 90° angle with respect the cluster. The experimental area is separated from the electrons beam line with radiator chamber and a beam dump by a 1.6 m thick wall of concrete blocks; this shield, together with the 2.6 m long

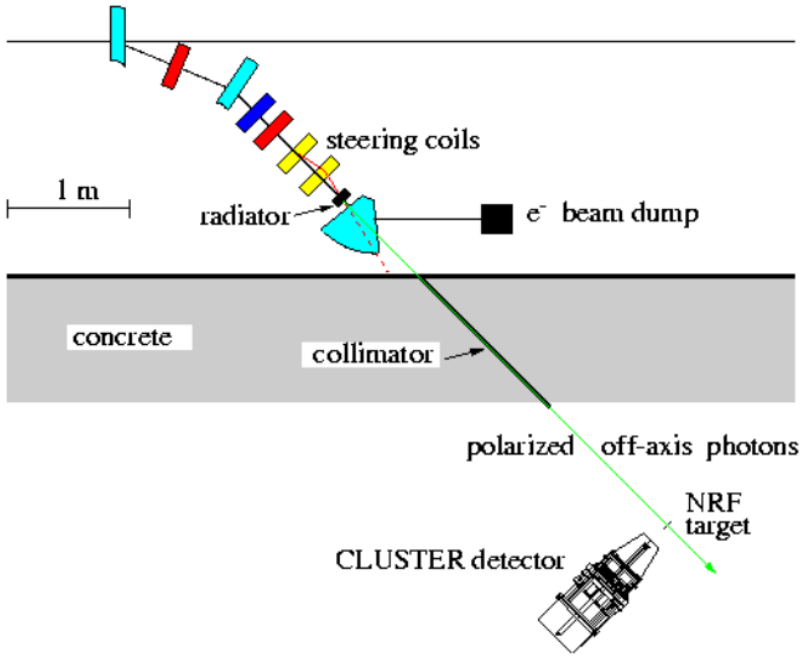

Figure 4.13: Polarized bremsstrahlung facility at ELBE: a scheme of the experimental set-up. [90]

collimator, reduces neutrons and photons backgrounds. It is possible to suppress the neutron background also by using time-of-flight techniques favoured by the large distance between radiator and NRF target and by the time structure of the electron beam. With an average beam currents of the order of 500 mA, photon fluxes of $5{\cdot}10^7$ photons per MeV·s for 7 MeV photons at E_{e^-} = 10 MeV are expected at the NRF interaction area. The energy deposition in the thin radiator foil does, thereby, not exceed about 30 W and is removed by water cooling.

4.2.4 The electronic read-out

For this test an analogue electronic chain and a standard VME data acquisition, based on the KMAX environment, were used [91]. The scheme of the analogue electronic chain is sketched in Fig. 4.14. The anode detector signal is split and sent to two dedicated NIM units, which we will call "PARISpro" (PP) and "Megamp" (MA). Both modules have been designed and realized by the INFN-Milano electronic group.
The PP unit provides as outputs an ECL time signal to a TDC and two analog shaped signals to a peak sensing ADC. One of signal sent to the ADC is proportional to the sig-

nal area, the second is proportional to the signal height. The two PP outputs have been used to identify where the events have deposited energy (in $LaBr_3$:Ce, in NaI:Tl or in both crystals).
The MA unit provides an ECL time signal with a threshold value which can be set at a lower value than in PP. The CFD unit used in both modules employed two very different shaping delay, in particular 56 ns (optimized for NaI:Tl pulse) in MA and 16 ns (optimized for $LaBr_3$:Ce pulse) in PP.
The time information was provided by two different TDC modules, one connected to MA time output and the other to the PP one. During the calibrations, the "Master Gate" (MG) was provided by the 'OR' output of the MA unit, i.e. from the signal of the 9 detectors using the lowest possible threshold (Trigger-1 in Fig. 4.14) while, during the measurement with the bremsstrahlung beam, the MG was given by the coincidence between the MA 'OR' and the beam RF (Trigger-2 in Fig. 4.14).
The "Start" signal of the TDCs was given by the MG and the individual detectors CFD outputs acted as a "Stop". Therefore, when Trigger-1 acted as "Master Gate", the time spectrum showed only auto-triggers. When Trigger-2 is selected, the time spectra represent the Time of Flight (TOF) measurement of the radiation (RF beam provide time information in the coincidence). It is important to remember that, as in phoswich detector the $LaBr_3$:Ce signal is approximately 7 times higher than the NaI:Tl one for the same deposited energy, the threshold energy value is very different depending on the event type.

PARISpro

PARISPRO is an evolution of a previous NIM module developed to disentangle γ rays and a charged particle interactions in BaF_2 and $LaBr_3$ detector on the base of differences between the peak amplitude and total area of detectors signals [92]. Such a module is suitable for the PARIS phoswich detector since interaction of γ rays in different parts of the detectors ($LaBr_3$, NaI or both) gives rise to completely different line shapes which add up linearly (see Fig.4.1). The module has 16 independent channels. Each channel is composed of three sections defined as Amplitude, Integral and Time information.
The Amplitude section is obtained by a analogue stretcher able to capture the peak of the signal independently of its leading edge; the signal is then shaped with a time constant of 0.4 μs.
The Integral section provides the total charge of the signal (which is proportional to the total energy deposited in the detector), and consists of a quasi-Gaussian shaper amplifier with a time constant of 1μs. The Amplitude of these two signals can be adjusted by selecting proper coarse and fine values.

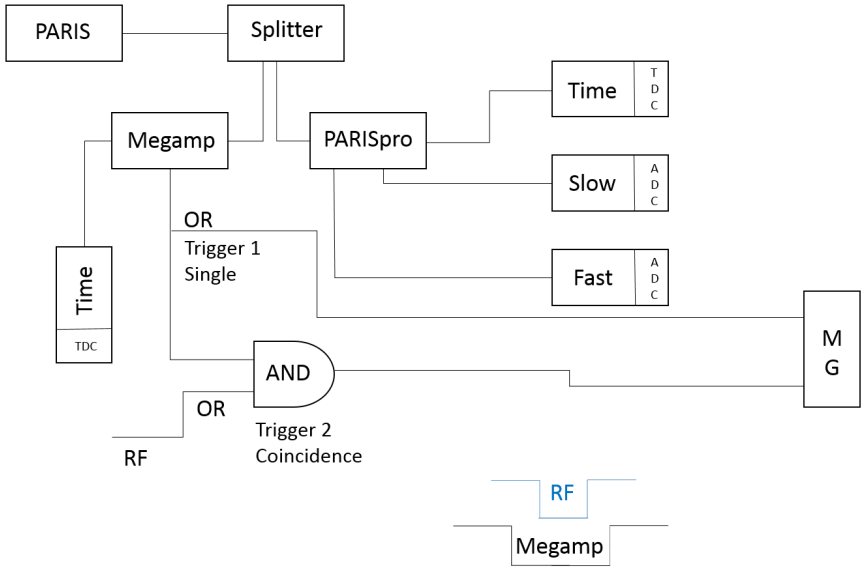

Figure 4.14: The scheme of the electronic chain.

The time information is given by a standard Constant Fraction Discriminator with an automatically walk compensation circuit. A five step 4 ns delay line allows user to properly adjust the delay according to different leading edge of the signals, during the ELBE experiment the delay was set to 16 ns.
As mentioned above, the NIM module houses sixteen channels, all the useful parameters like gain, CFD thresholds and participation to the trigger are programmable by means of a RS485 serial line. Set values are stored in a non volatile memory and are reloaded at the power-on.

MEGAmp

MEGAMP is a general purpose shaping amplifier module suitable for different types of detectors signals like the ones coming from fast scintillators or charge sensitive preamplifiers [93]. Even if it can provide several additional information, it was used in our setup as a low threshold CFD. This unit was optimized to provide the time information from the NaI:Tl part of the phoswich detector and to a a scaler to control rate of the events in each of the nine detectors of the cluster. During the ELBE experiment the CFD delay was set to 56 ns.

4.2.5 Energy calibration

Calibration was performed using two radioactive sources, ^{137}Cs (661.7 keV) and ^{60}Co (1173.2 keV and 1332.5 keV). A linear calibration was employed.

The extracted FWHM values for the 661.7 keV and 1332.5 keV lines in $LaBr_3$:Ce, NaI:Tl and Compton are shown, detector by detector, in Tab. 4.2. The relative error on the FWHM value is estimated to be 0.7% of the width. This value arises from the estimation on how statistical fluctuations and the peak fit procedure influence the FWHM values.

	FWHM [keV]					
	661.7 keV			**1332.5 keV**		
Detector position	**$LaBr_3$:Ce**	**NaI:Tl**	**Compton**	**$LaBr_3$:Ce**	**NaI:Tl**	**Compton**
1	32.7	57.4	47.1	47.9	65.0	54.5
2	31.6	54.6	43.8	43.4	74.6	56.2
3	40.2	52.7	44.4	54.3	67.0	56.6
4	29.3	48.8	50.2	42.5	64.3	54.7
5	39.0	47.5	47.4	52.4	65.4	61.3
6	36.0	53.2	51.4	49.7	65.9	55.8
7	33.8	52.0	42.9	46.5	61.9	54.6
8	36.4	45.6	49.5	49.8	64.4	57.3
9	34.8	49.1	44.7	48.0	68.0	54.5

Table 4.2: The values of FWHM (expressed in in keV) measured at 661.7 keV and 1332.5 keV for the γ-rays which deposited all their energy in $LaBr_3$:Ce, NaI:Tl and in both (Compton). The relative error on FWHM value is estimated to be 0.7% of the width.

Figure 4.15 displays the calibrated spectra of phoswich 3 when $LaBr_3$:Ce, NaI:Tl and "Compton" events are selected. It is interesting to note that the measured FWHM for the Compton events assumes values intermediate between those in $LaBr_3$:Ce and in NaI:Tl. This is consistent with the fact that Compton region contains the events in which energy deposition is shared between $LaBr_3$:Ce and NaI:Tl crystal. All the calibration residuals are of the order of 1 keV.

The average energy resolutions are around 5% for $LaBr_3$:Ce crystals and around 7.7% for NaI:Tl ones. For a $LaBr_3$ such energy resolution is higher than the typical energy resolution values of this kind of crystals, around 3-4%. This degradation cannot be explained by the geometric loss in the light collection, due to the coupling between a square crystal and a cylindrical PMT. The most reasonable explanation is the fact that the scintillation light produced by the $LaBr_3$ has to pass through the coupled NaI:Tl crystal before being detected by the photomultiplier tube, with a probable degradation.

The Area ratio (events number inside a peak) between NaI:Tl and $LaBr_3$:Ce peaks is approximatively 0.14 at 661.7 keV and 0.15 at 1332.5 keV in all detectors. These numbers highlights an aspect predicted by the simulation (see Fig. 4.4): a high percentage of the low energy γ radiation is fully absorbed in $LaBr_3$:Ce (more than 80% for γ-rays below 2 MeV).
The Area ratio between Compton and $LaBr_3$:Ce peaks is approximatively 0.05 at 661.7 keV and 0.09 at 1332.5 keV in all detectors. As the green curve of Fig. 4.15 evidences, indeed, the 661.7 keV "Compton" event is unlikely and the percentage of events which share the energy deposition between the two crystals increase with the γ energy.

Looking at the $LaBr_3$ energy spectrum of Fig. 4.15 (the red curve), it is possible to note some structures, an energy continuum in the region 800-1000 keV and a peak at ~1460 keV, which are not present in the NaI:Tl spectrum and barely visible in the Compton spectrum. The Lanthanum Bromide detector, indeed, is affected by internal radioactivity, due to the presence of ^{138}La and ^{227}Ac, a rare isotope (natural isotopic abundance of 0.09%) and a chemical homologue of La respectively.
The ^{138}La isotope, with a lifetime of 10^{11} years, undergoes β^- decay to ^{138}Ce or electron capture to ^{138}Ba. The β^- decay is responsible for the energy structure between 800 and 1000 KeV in the energy spectrum (see the red curve of Fig. 4.15). Such a structure is produced by the overlap of the full energy peak of a 789 keV γ-ray, emitted by ^{138}Ce, and the β continuum, due to the electron emitted during the decay. The electron capture process, instead, produces the energy peak at ~1460 keV. This peak, indeed, is characterised by the overlap of a 1436 keV γ-ray emitted during the electron capture and another peak at a distance of ~32 keV. This is approximatively the energy of the ^{138}Ba X-ray [94]. This "double-peak" overlaps also with the 1461 keV γ-ray due to the natural radioactivity of ^{40}K which, anyway, gives a contribution of less than 15% [94].
The ^{227}Ac produces a β continuum up to around 1400 keV, due to the decay of ^{211}Pb and ^{207}Tl (belonging to the ^{227}Ac decay chain) and an α activity responsible for an energy structure in the region 1.8-3 MeV, which is not visible in Fig. 4.15.

Since the NaI:Tl is not contaminated, none of the continuum energy structures described above is present. Only the 789 keV peak and the 1436 keV peak (overlapped with the 1461 keV from ^{40}K), coming from the $LaBr_3$:Ce crystal, are barely visible. In the Compton spectrum, characterised by events interacting in both the two crystals there is a very small evidence of the 1460 keV peak.

4.2.6 Time analysis

As previously mentioned, in the beam test at ELBE an energy continuous γ beam up to 16.7 MeV impinges on a ^{11}B-^{12}C target and then it is stopped by a lead shielded beam

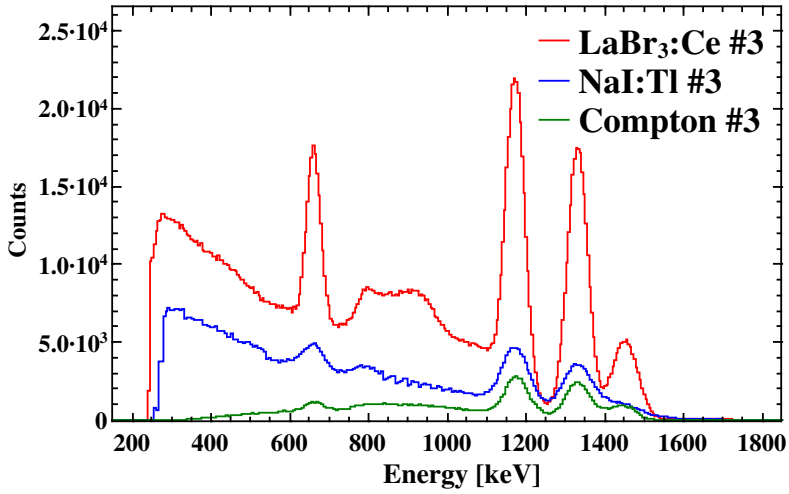

Figure 4.15: Energy spectra obtained projecting on the x axes the three different gated region of the "Amplitude vs Integral" matrix (detector in position #3). The red spectrum refers to $LaBr_3$:Ce events, the blue and the green ones are associated to NaI:Tl and to Compton events respectively.

dump. Together with the radiation generated by the de-excitation of the ^{11}B-^{12}C nuclear states, therefore, there is a very strong background mainly produced by 511 keV γ rays (from Pair Production inside the target or the beam dump) summed to a continuum mostly produced by Compton scattered γ rays from the beam in the target or from every material intercepted by the beam. An important goal of the analysis is therefore to develop a technique in order to eliminate such background. The structure of any $LaBr_3$:Ce or Compton spectra is dominated by the 511 keV peak, which contains about 75% of total events (see the black spectrum of Fig. 4.18). In order to suppress the background, a key aspect of the analysis is a suitable choice of the time condition. At first, it is worth to compare the time spectra of the 511 keV peak with the one relative to a ^{11}B transition, for example at 4444.81 keV (see the inset in the central panel Fig. 4.16 for $LaBr_3$:Ce crystal spectrum of detector 1). The two peaks fall in the same time region but their centroids are shifted of around 1 ns; therefore a narrow time gate (15 channels = 1.5 ns) on the transition allows to reduce the 511 keV events of an order of magnitude, without any important loss of statistic of the ^{11}B produced γ-rays. Such a time gate was identified for each of the nine detectors for $LaBr_3$:Ce and Compton events separately. The time resolution of the prompt peak in $LaBr_3$:Ce is of about 1 ns. The comparison between two spectra with and without the time condition is presented in Fig. 4.18 for $LaBr_3$:Ce; at low energy a time gate is fundamental in order to reduce the background, whereas, over about 4 MeV, there's no need for a time gate because we don't have high-energy

background.
In NaI:Tl the threshold corresponds to an energy value of ~2.8 MeV, higher than the $LaBr_3$:Ce one (~ 400 keV), and therefore 511 keV events do not contribute to the time spectra of NaI:Tl crystals: the gate here can be larger (here 25 channels = 2.5 ns), as shown in Fig. 4.17. The time resolution of the prompt peak in NaI:Tl is of about 2 ns.
It is worth to note that, for $LaBr_3$:Ce, we use the time information from PARISpro TDC and, for NaI:Tl, we use the time information from Megamp TDC.

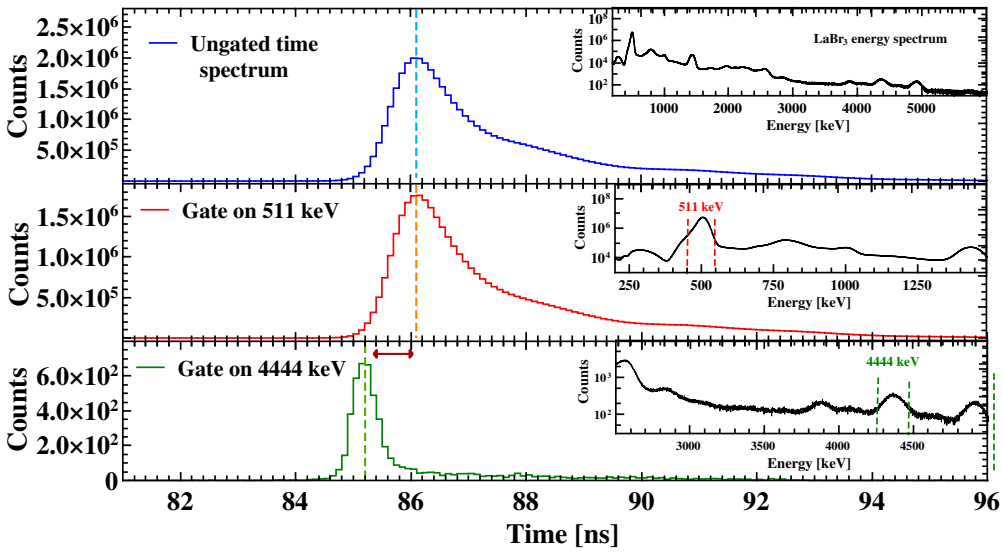

Figure 4.16: $LaBr_3$:Ce time analysis. Top panel: total time spectrum ($LaBr_3$:Ce + NaI:Tl) without any condition. In the inset the total energy spectrum of $LaBr_3$:Ce is shown. Middle panel: $LaBr_3$:Ce time spectrum of 511 keV events. In the inset the $LaBr_3$:Ce energy spectrum is shown with time gate on 511 keV peak. Bottom panel: time spectrum of 4444 keV events. The prompt peak has a time resolution of about 1 ns. In the inset the $LaBr_3$:Ce energy spectrum is shown with time gate on 4444 keV peak.

4.3 MILANO Test

In April 2015 at Milano University, another test has been performed to study the event distribution in the PARIS cluster. For this purpose, the following radioactive γ-ray sources have been used: ^{137}Cs (E_γ = 661.7 keV), ^{60}Co (E_γ = 1173.2 keV and 1332.5 keV), ^{88}Y (E_γ = 898 keV and 1836 keV) and Am-Be-Ni.

The Am-Be source can be used either as a γ-ray or a neutron source. It generates

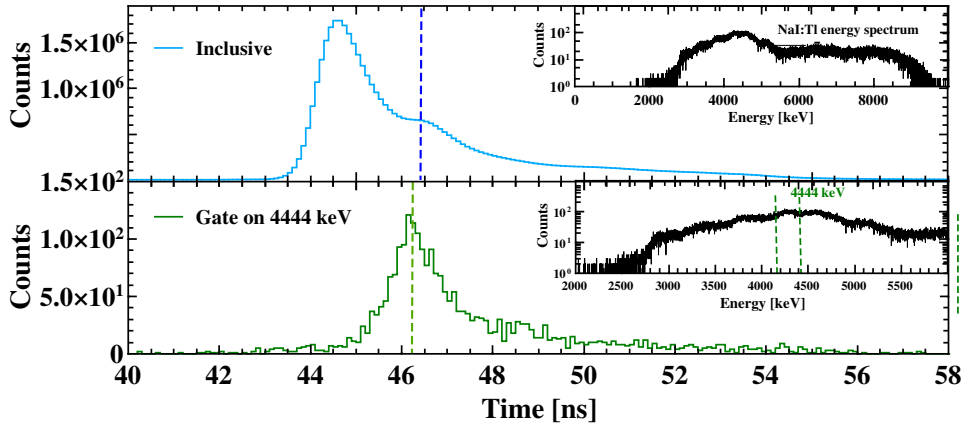

Figure 4.17: NaI:Tl time analysis. Top panel: total time spectrum ($LaBr_3$:Ce + NaI:Tl) without any condition. In the inset the total energy spectrum of NaI:Tl is shown. Bottom panel: time spectrum of 4444 keV events. In the inset the NaI:Tl energy spectrum is shown with time gate on 4444 keV peak.

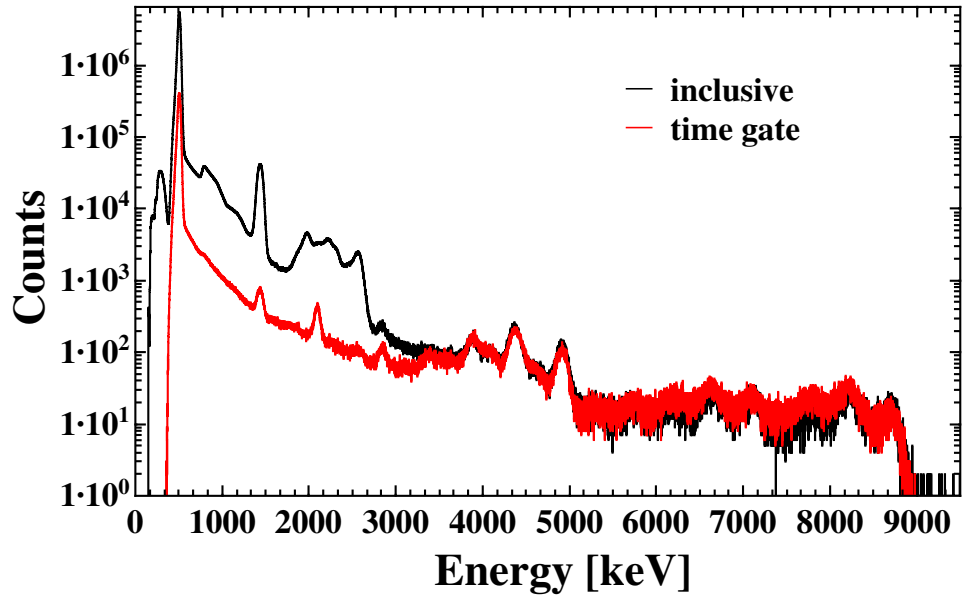

Figure 4.18: $LaBr_3$:Ce energy spectrum of ELBE test, without (black) and with (red) time condition. The spectrum in black is dominated by 511 keV peak.

neutrons of energy up to ~10 MeV by the following nuclear reactions:

$$^{241}Am \rightarrow {}^{237}Np + \alpha + \gamma + Q_{val}(5.637)MeV,$$

$$\alpha + {}^{9}Be \rightarrow {}^{12}C^{*} + n + Q_{val}(5.704MeV).$$

$^{12}C^{*}$ is populated in an excited state, with the consequent emission of γ-rays. The most probable state (more than 60%) is the first exited state (4.44 MeV). The Am–Be source was brought into contact with Ni sheets (Am-Be-Ni source), into a 3x3x7 cm hole drilled in a cylindrical shape paraffin wax. The neutrons from the Am–Be–Ni source were thermalized in the paraffin housing and then captured in Ni, producing γ-rays of energies up to 8.98 MeV.
For this test the same read-out system of ELBE test has been used: an analogue electronic chain and a standard VME data acquisition, based on the KMAX environment (see sec. 4.2.4).

4.3.1 Energy resolutions

A linear calibration has been employed using a ^{137}Cs and a ^{60}Co radioactive-sources. The energy resolution of the 9 detectors has been calculated and are reported in Tab. 4.3.

	FWHM [keV]			
	661.7 keV		**1332.5 keV**	
Detector position	**$LaBr_3$:Ce**	**NaI:Tl**	**$LaBr_3$:Ce**	**NaI:Tl**
1	34.1	49.6	47.7	65.1
2	36.3	53.8	47.1	64.9
3	29.4	52.7	41.7	65.0
4	35.8	52.2	49.6	64.1
5	32.3	51.1	44.3	62.0
6	33.1	48.9	43.0	64.1
7	34.1	46.4	47.5	63.2
8	38.1	56.3	54.7	68.6
9	33.2	53.3	48.4	63.7

Table 4.3: The values of FWHM (expressed in in keV) measured at 661.7 keV and 1332.5 keV for the γ-rays which deposited all their energy in $LaBr_3$:Ce and NaI:Tl. The relative error on FWHM value is estimated to be 0.7% of the width.

It is worth to note that, for ELBE and Milano tests, the cluster was composed by the same 9 detectors which, however, were arranged in a different way for the two tests. In other words, the position number (marked in Fig. 4.10 and indicated with "Detector

position" in the Tab. 4.2 and Tab. 4.3) may correspond to two different detectors for ELBE and Milano tests.

This calibration measurement has been performed in a laboratory, a more controlled environment than the ELBE experimental hall. Anyway, as one can see in Tab. 4.3, the FWHM values are comparable with the ones found during the ELBE test. The average energy resolutions are around 5% for $LaBr_3$:Ce crystals and around 7.5% for NaI:Tl ones. This confirms the degradation of $LaBr_3$:Ce resolutions, probably due to the fact that the light produced in $LaBr_3$:Ce has to pass trough 6" of NaI:Tl before reaching the PMT.

4.3.2 Event distribution analysis

The study of the events distribution inside the single phoswich and the cluster is a key aspect of the characterization. We assert that an event has "fold n" (F_γ=n) if n detectors register a non zero energy value in a defined time window.
For a single phoswich, we analysed the distribution of the full energy peak events, when the γ-ray energy is completely released inside the detector. For this test, we used ^{60}Co, ^{88}Y and Am-Be-Ni source placed at 20 cm from the cluster. We considered three different classes of full energy peak events: $LaBr_3$:Ce, NaI:Tl and Compton ones. It is worth to note that the Compton events in a single phoswich are associated to interaction in two crystals ($LaBr_3$:Ce and NaI:Tl), so they could not literally be full energy peak events. However, since they are treated as a specific class of events, different from $LaBr_3$:Ce and NaI:Tl ones, we call "Compton full energy peak event with F_γ=1" an event in which the γ-ray energy is completely released in a single detector, but shared between $LaBr_3$:Ce and NaI:Tl crystals. Therefore, for the cluster, the maximum measurable fold is F_γ = 9 (the number of detectors).
The result of this analysis is illustrated in Fig. 4.19. As one expects, in the energy region 0-5 MeV the biggest part of this kind of events occurs in $LaBr_3$:Ce crystals, since it is the first one that the γ-ray impinges on. Below ~1 MeV $LaBr_3$:Ce full energy peak events are around 80% and they decrease with the energy up to around 60% at 4.4 MeV. The number of NaI:Tl full energy peak events, on the contrary, increase with the energy. The Compton events constitute the smallest fraction of events, which becomes just significant above 2 MeV.
Our results have been compared with the simulation, previously illustrated in Fig. 4.4, performed by Michał Ciemała (Krakow group) in 2015, using the software GEANT-4 [75, 76]. As one can see in Fig. 4.20, experimental data and simulations follow the same trend as a function of the γ-ray energy even though it seems that the simulations overestimate the full-absorption in $LaBr_3$:Ce crystal.

For each crystal, we determined the percentage of full energy peak events in it,

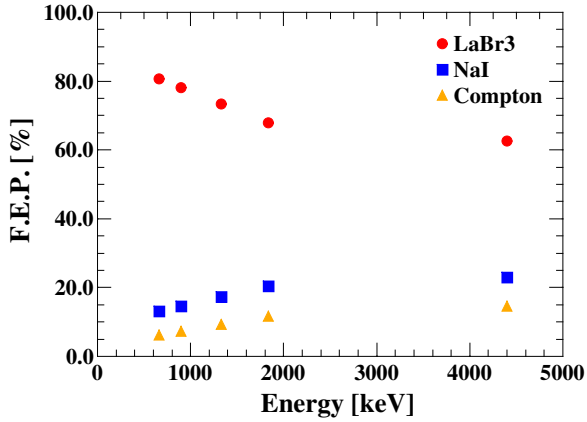

Figure 4.19: Full energy peak events distributions in a single PARIS phoswich. The red circles, the blue squares and the yellow triangles refer to $LaBr_3$:Ce, NaI:Tl and Compton events respectively.

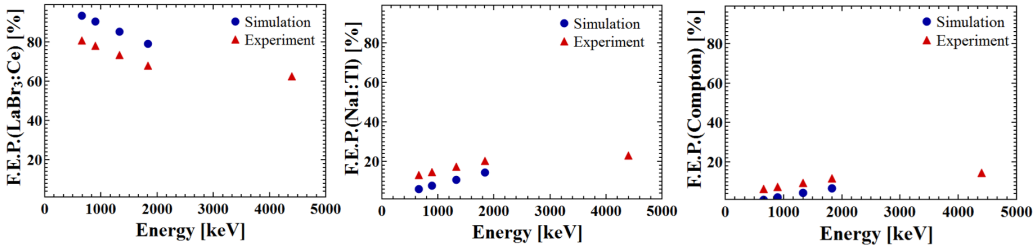

Figure 4.20: $LaBr_3$:Ce (left panel), NaI:Tl (central panel) and Compton (right panel) full energy peak (F.E.P.) events distribution in a single PARIS phoswich: comparison between experimental data (red triangles) and simulation (blue circles).

$\#F.E.P.(F_\gamma = 1)$, over the total events of γ-rays fully absorbed by the cluster detectors (any fold) that involve the considered crystal, $\#F.E.P.(F_\gamma \geqslant 1)$. For the sake of simplicity, we defined K:

$$K = \frac{\#F.E.P.(F_\gamma = 1)}{\#F.E.P.(F_\gamma \geqslant 1)}. \tag{4.3}$$

The determination of K has been performed, as a function of the energy between 0.662 and 8.98 MeV. We considered $LaBr_3$:Ce or NaI:Tl "pure" events, i.e. events associated to single or multiple interactions occurred all in $LaBr_3$:Ce crystals or all in NaI:Tl ones respectively. This is because the two crystal can be used for different purposes. For instance, only the $LaBr_3$:Ce crystal provides a good energy resolution. Therefore, to have a good energy resolution, in add-back process only $LaBr_3$:Ce "pure" are to be considered.

NaI:Tl interactions, indeed, would degrade the resolution. It should be used where a good resolution is not needed, as, for instance, for the measurement of the IVGDR γ-decay.

The K values, as a function of the energy, are reported in Fig. 4.21 for $LaBr_3$:Ce (left panel) and NaI:Tl (right panel) "pure" events. As expected, in both $LaBr_3$:Ce and NaI:Tl case K decreases with the energy and this effect is mostly evident for the crystal in the central position (ph # 5 in Fig.), since it has the largest number of neighbours, then in the crystals placed on the sides (ph # 2, 4, 6, 8 in Fig.) and it affects much less the crystals on the corners (ph # 1, 3, 7, 9 in Fig.), which have only two neighbour detectors. With the increasing of the energy, the K dependence on the number of neighbour detectors becomes more evident. This is clearly visible especially for $LaBr_3$:Ce events (see the left panel of Fig. 4.21).

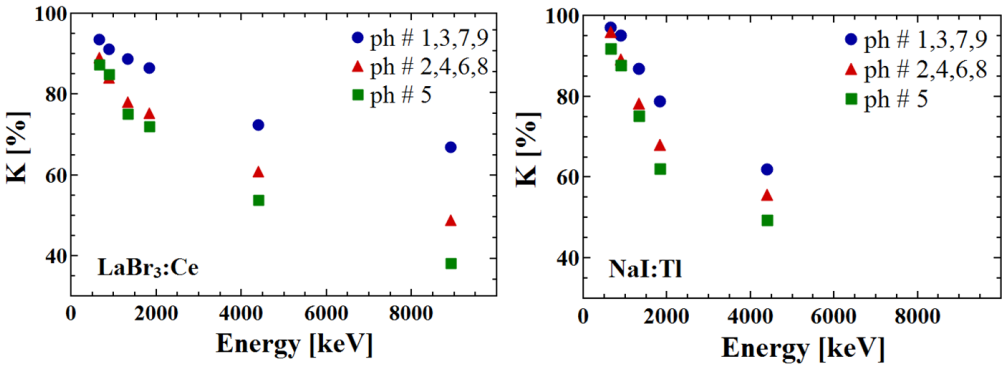

Figure 4.21: The K value (eq. 4.3) as a function of the γ-ray energy for $LaBr_3$:Ce "pure" events (left panel) and NaI:Tl "pure" events (right panel). In both the two cases, K decreases with the energy. This is mostly evident for the central detector, #5, which has the highest number of neighbour detector.

It is also interesting to analyze "multiple" scattering between the cluster detectors. The study was conducted considering the $LaBr_3$:Ce and the NaI:Tl "pure" events with fold higher than 1. Fixing a single crystal ($LaBr_3$:Ce or NaI:Tl) in which a "multiple" γ-ray interacted, we want to know in which crystals (of the same type) the other interactions occur. This is shown, detector by detector, in Fig. 4.22, which depicts nine front sections of the PARIS cluster. There are no significant difference between $LaBr_3$:Ce and NaI:Tl cases, as shown quantitatively in Fig. 4.23. Whatever is the crystal considered (represented by a white square in Fig. 4.22), the largest number of "multiple interactions" occurs in detectors who have a common side with it. Also detectors sharing a vertex register a significant interactions number. Overall, the detectors surrounding the

reference one collect around 99% of "multiple" γ-rays, in the case of energy up to 4.4 MeV.

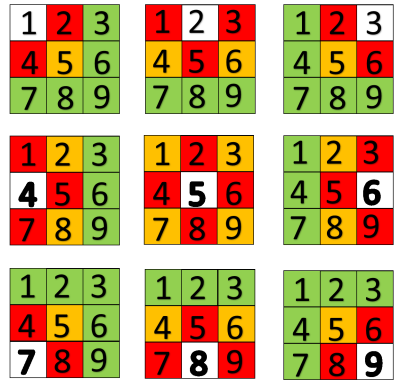

Figure 4.22: Analysis of "multiple" γ-rays scattering for source-data up to 4.4 MeV. White detector is the reference one: an interaction occurs there. The other detectors color depends on how many interactions (belong to the same γ-ray) are collected inside them. The highest interactions percentage is shared between red detectors that, together with the yellow ones, reach 99%. Green detectors collect a negligible residual γ-rays percentage.

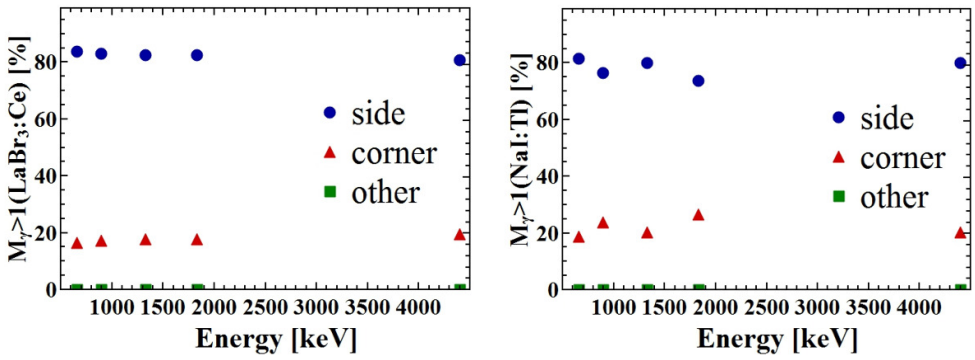

Figure 4.23: The spatial distributions of $LaBr_3$:Ce (left panel) and NaI:Tl (right panel) "pure" multiple events in the cluster. For both the two cases, the scattering occurs almost totally among crystals which share a side (around 80%) or a corner (around 20%). Green detectors collect a negligible residual γ-rays percentage.

CHAPTER 5

The CLYC scintillator detectors: efficiency measurements

In this chapter we will present a measurement of the fast neutron detection efficiency for two samples of CLYC scintillator detectors. As will be explained, such detectors could be ideal candidates for the Isospin mixing investigation via the γ-decay of Giant Dipole Resonance, because of their capability to identify, measure and therefore separate (high-energy) γ-radiation and neutrons. For this reason, a complete characterisation of these detectors is necessary and, in particular, the efficiency represents a key parameter in the planning of future measurements.

5.1 The CLYC scintillator

The search for high performing scintillators materials has had a great development in the lasts 20 years [95]. In this framework, the Elpasolite, discovered about 15 years ago [96], are a promising class of scintillators characterised by good energy and time resolution and high linearity, in particular at low energy. Examples of scintillators belonging to this class are the Cs_2LiYCl_6:Ce (CLYC), $Cs_2LiLaCl_6$:Ce (CLLC) and $Cs_2LiLaCl_6$:Ce (CLLB). Among them, the CLYC scintilators are very interesting detectors, due to their capability to identify and measure both neutrons and γ-rays. They are characterised by a density

of 3.3 g/cm^2, a light yield of ~20000 photons/MeV and an excellent proportionality between the energy deposited and the light output. The γ energy resolution at 662 keV is $< 5\%$ [97–107].

The CLYC scintillators can detect both fast and thermal neutrons. As will be discussed in sec. 5.3, the thermal neutron detection capability arises from the presence of ^{6}Li. It is therefore possible to control the thermal neutron sensitivity by the selection of ^{6}Li or ^{7}Li enrichment. In particular, a ^{6}Li enriched CLYC, that we will call CLYC-6, has a high sensitivity to thermal neutron, while a ^{7}Li enriched CLYC, that we will call CLYC-7, is practically not sensitive to thermal neutrons and therefore it allows a better detection of fast neutrons.

The neutron energy resolution has been measured, for example, in [108] for CLYC-6 and CLYC-7 scintillators as a function of the neutron energy. It was found that it is rather constant with the energy and it ranges between 7.5% and 10.2% (see Fig. 5.1). Similar results have been also obtained in [109]. The measured energy resolution is larger than the one expected for γ-rays of the same energy. The reason of that is not clear and a detailed study of the reaction mechanism is needed.

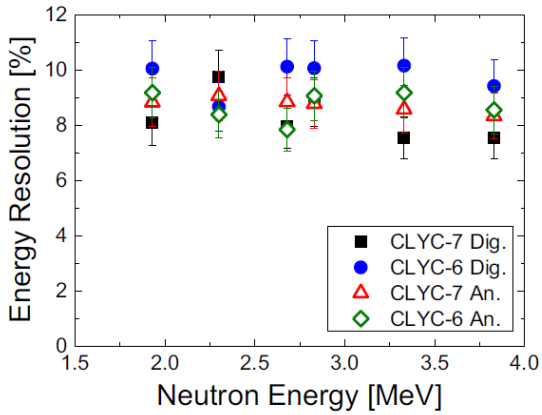

Figure 5.1: Neutron energy resolution of CLYC-7 (black squares and red triangles) and CLYC-6 (blue circles and green diamonds) measured with two different acquisition system: an analog one (red triangles and green diamonds) and a digital one (black squares and blue circles). Taken from [108].

In nuclear physics experiments, especially in case of radioactive beams, there is a great interest in the fast neutron identification and neutron spectroscopy [108]. The energy of the fast neutrons, until now, has been measured using the time of flight (TOF) technique. Since in nuclear structure experiments the typical energy range of the neutron is ~1-10 MeV, the TOF method requires thin detectors and a flight path between target and detector of at least 70 cm. Due to the general low intensity of the radioactive

beams, however, small target-detector distances are necessary. A short distance allows to increase the subtended solid angle, without the use of a large number of detectors. Indeed, it is worth to remember that approximately ten times more detectors are required to cover the same solid angle if the detector-target distance is increased from 20 to 70 cm. The possibility to identify neutrons through PSD and to measure the energy of the fast neutrons using the detector energy signal allows a small target-detector distance.
The Isospin mixing measurement via the γ-decay of IVGDR in self-conjugate nuclei heavier than ^{80}Zr demands the use of radioactive beams and thus of small target-detector distances. Furthermore, to measure the IVGDR decay the capability to discriminate γ-rays from neutrons is an essential requirement. To fulfil all of these conditions, a CLYC scintillator array seems to be a unique solution.

In this sense, a complete knowledge of the CLYC scintillator detectors is required. In this chapter, we will focus on CLYC neutron detection and, in particular, on the fast neutron detection efficiency measurement. This falls within a context of a complete CLYC characterization work.

5.2 Neutron/γ-ray discrimination with PSD technique

One of the most interesting features of the CLYC scintillator detectors is the possibility to use the pulse shape discrimination (PSD) technique to identify the nature of the interacting radiation and, in particular, to distinguish neutrons and γ-rays from their difference in the scintillation decay response. The gamma trace, indeed, contains a fast component of photons originated by the CVL (core to valence luminescence), with a short decay time, together with a slowly decaying component of scintillation light channelled through the Ce^{3+} ions. The neutron trace, instead, is characterized by a much slower decay time constants [110]. An example of the pulse line-shapes produced by a γ-ray and by a neutron are shown in Fig. 5.2.

The neutron/γ-ray discrimination is performed by comparing the charge integrated over two regions of the digitised pulse [102]. The PSD ratio R is given by the formula:

$$R = \frac{A[W_2]}{A[W_1] + A[W_2]},$$

where $A[W]$ is the integral of the signal samples, over the two different time windows: $W1$, at the beginning of the signal, and $W2$, on the signal decay. For instance, for the efficiency measurement described in sec. 5.4 the following integration windows have been used: $W1$, from the onset to 80 ns, and $W2$, from 100 ns to 600 ns [95]. Fig. 5.3 shows a typical PSD matrix of CLYC-6, where the x axis is the total deposited energy (obtained by integrating the signals from the onset up to 3 μs) and the y axis is the PSD

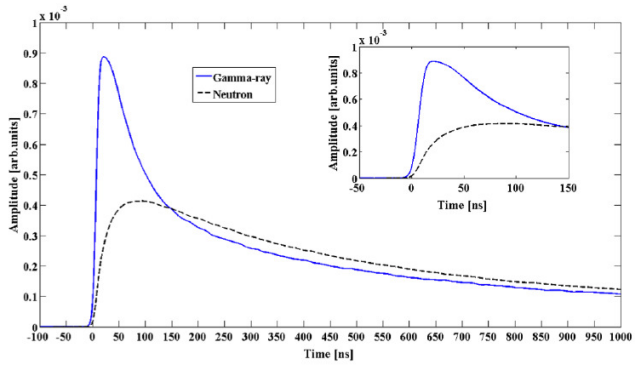

Figure 5.2: Comparison between a signal produced by a γ-ray (blue full line) and a signal produced by a neutron n (black dashed line). Adapted from [110]

ratio, R. Two main event groups can be observed in the matrix: one with $0.9 \leqslant R \leqslant 0.95$, corresponding to neutron events, and a lower one, with $0.8 \leqslant R < 9.0$, corresponding to γ rays.

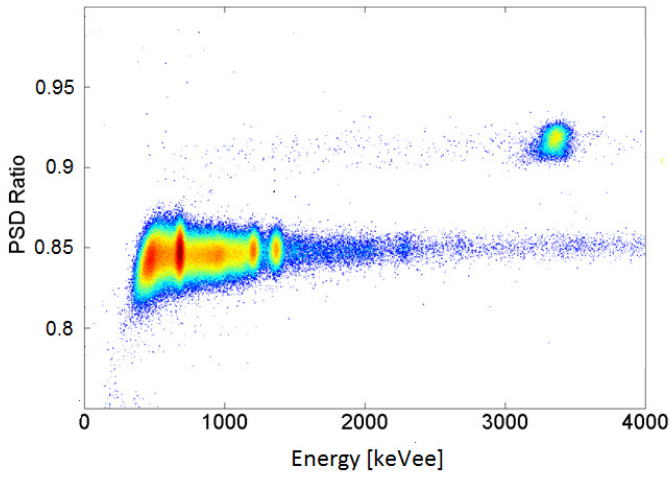

Figure 5.3: A typical PSD matrix for CLYC-6: x and y axes show the total deposited energy and the PSD ratio R respectively. Two groups of events can be identified in the matrix: the upper one ($0.9 \leqslant R \leqslant 0.95$) corresponds to neutron events and the lower one ($0.8 \leqslant R < 9.0$) to gamma events. Adapted from [95]

5.3 Neutron interaction mechanism

The fast neutron detection capability of the CLYC scintillators arises mainly from the presence of ^{35}Cl, through the reaction mechanisms ^{35}Cl(n,p)^{35}S and ^{35}Cl(n,α)^{32}P, in which ^{35}S and ^{32}P are populated in the ground state or in an excited state. It is important to say that, for the sake of simplicity, in this work we will consider the reaction channels that populate the ground state and the first two excited states of ^{35}S and ^{32}P.
In CLYC-6, the presence of ^{6}Li isotope increases the neutron detection capability via the reaction ^{6}Li(n,t)α, especially in the thermal neutron region: the cross section value for the absorption of a thermal neutron is about 940 b, while the value for the absorption of 1 MeV neutron is ~0.2 b.
Fig. 5.4 shows the cross sections of the mentioned channels as a function of E_n, the neutron incoming energy [111].

It follows that a neutron with energy E_n will be detected via different reaction channels, each one resulting in a different measured effective energy E_{eff}. The scintillator light output due to the interaction of energetic particles (p, α or t) is proportional to the incident neutron energy E_n corrected by the Q−value of the corresponding reaction channel and by the quenching factor. Following the notation adopted in [111], we define Q_M as the mass difference Q−value, and Q_I as the Q−value for the excited states of the residual nuclei (Q_I=Q_M-E^*). Therefore, the measured effective energy E_{eff} in terms of MeV electron equivalent (MeVee) is expected to be:

$$E_{eff} = (E_n + Q_{M,I}) \cdot f_{quenching}, \tag{5.1}$$

where $f_{quenching}$ is the detector quenching factor and depends on the particle type: it is estimated to be ~0.9 for protons, and ~0.5 for α particles [101]. Since we measure both tritium and alpha particle, $f_{quenching}$ ~0.7 has been used for ^{6}Li(n,t)α [101]. To better understand the concept, Tab. 5.1 lists the measured effective energies E_{eff} for three given E_n values ($E_n^{thermal}$=0.025 eV, E_n=1 MeV and E_n=5 MeV). As one can see, a neutron with E_n = 1 MeV, for instance, will be seen with six different measured energies, from 0.040 MeV to 4.055 MeV, corresponding to the various reaction channels it has undergone.

5.4 Fast neutron detection efficiency

A measurement of the fast neutron detection efficiency was performed at L.A.S.A. Laboratory of INFN (*Istituto Nazionale di Fisica Nucleare*) and University of Milano in March 2015 for two cylindrical samples of CLYC scintillators, both 1"x1" in size. One sample is enriched with more than 99% of ^{7}Li (CLYC-7) and the second one with about 95% of ^{6}Li

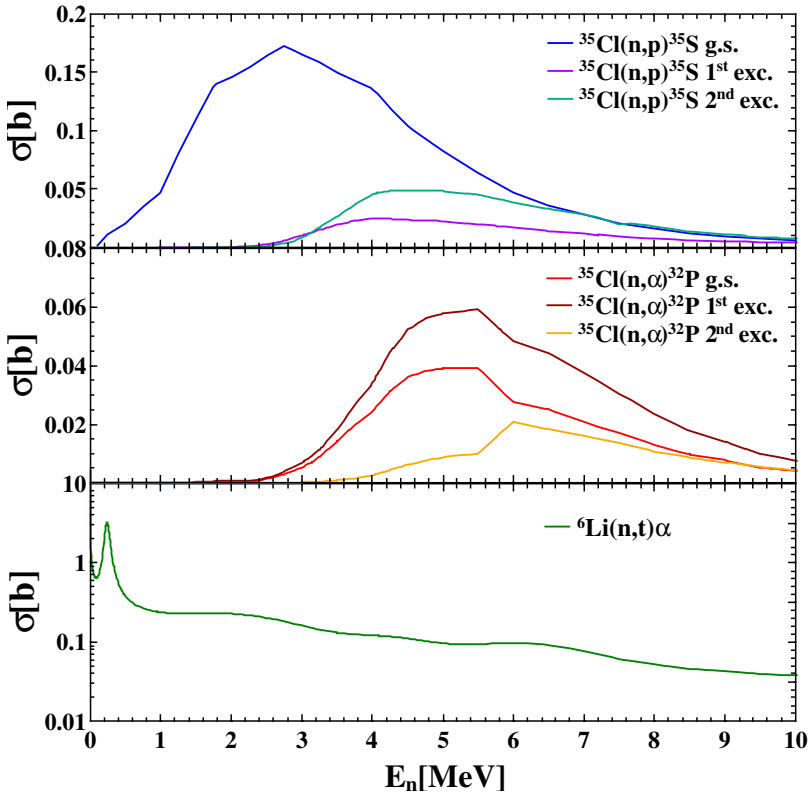

Figure 5.4: Cross sections of the different reaction channels considered [111]. Top panel: ^{35}Cl(n,p)^{35}S with the population of ^{35}S in the ground state and the first two excited states. Middle panel: ^{35}Cl(n,α)^{32}P with the population of ^{32}P in the ground state and the first two excited states. Bottom panel: ^{6}Li(n,t)α channel. It is to be noted that the cross section value for this neutron absorption reaction at E_n=0.025 eV is about 940 b.

reaction channel		$Q_{M,I}$ [MeV]	$f_{quenching}$	E_{eff} [MeVee]		
				$E_n^{thermal}$	E_n = 1 MeV	E_n = 5 MeV
^{35}Cl(n,p)^{35}S	g.s.	0.615	0.9	0.554	1.453	5.054
	1st exc.	-0.956	0.9	/	0.040	3.276
	2nd exc.	-1.376	0.9	/	/	3.262
^{35}Cl(n,α)^{32}P	g.s.	0.938	0.5	0.469	0.969	2.969
	1st exc.	0.860	0.5	0.430	0.930	2.93
	2nd exc.	0.425	0.5	0.213	0.713	2.713
^{6}Li(n,t)α	g.s.	4.793	0.7	3.355	4.055	6.855

Table 5.1: Conversion from the neutron incoming energy, E_n, to the effective measured E_{eff} energy in MeVee, for the seven different reaction channels considered, using eq. 5.1. The $Q_{M,I}$ and $f_{quenching}$ values are listed in columns 2 and 3 respectively. The effective measured energy values E_{eff}, listed in columns 4, 5 and 6 correspond to a thermal neutron $E_n^{thermal}$, a neutron with energy E_n = 1 MeV and one with E_n = 5 MeV respectively.

(CLYC-6).
A calibrated ^{241}Am-Be source was used. Its nominal activity was 1 Ci, which corresponds to a neutron emission per second of $2.4 \cdot 10^6$. Such a source generates neutrons of energy up to ~10 MeV [112] through the following nuclear reactions:

$$^{241}Am \rightarrow {}^{237}Np + \alpha + \gamma + Q_{val}(5.637)MeV,$$

$$\alpha + {}^{9}Be \rightarrow {}^{12}C^{*} + n + Q_{val}(5.704MeV).$$

The ^{241}Am-Be source neutron continuum spectrum is shown in Figure 5.5 [112].

To estimate the efficiency, the neutron flux $\Phi_{n\ measured}$ was measured varying, for each detector, the source-detector distance $d_{d\text{-}s}$ and consequently the solid angle Ω. Different measurements was performed:

- for CLYC-6 at $d_{d\text{-}s}$ = 0.775 m, 1.0 m, 1.2 m and 1.4 m,
- for CLYC-7 at $d_{d\text{-}s}$ = 1.0 m and 1.4 m,
- a background measurement for each crystal.

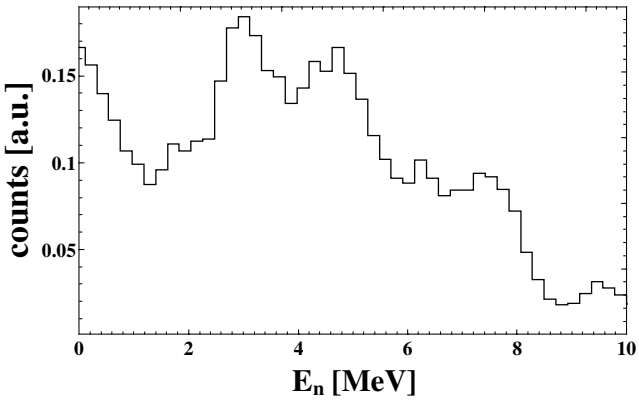

Figure 5.5: ^{241}Am-Be source neutron continuum emission spectrum [112]. The error (for each bin) estimated by the authors is ~4%.

The electronic read-out

A digital acquisition was used, which allows to perform the Pulse-Shape-Discrimination. The CLYC scintillators were coupled to HAMAMATSU R6233-100Sel photomultiplier tubes (PMT) and to two standard HAMAMATSU voltage dividers (VD), E1198-26 and E1198-27. The PMTs were powered at 800V (CAEN-N1470AL). A pulser (10 Hz) was employed in the acquisition, for the dead time estimate.

The anode signal was split using a custom module which also amplify the signal by a factor ~4. One copy was sent to a 12 bit, 600 MHz LeCroy waverunner HRO 66Zi oscilloscope and digitized and the second one to a Logic FAN-IN FAN-OUT module, a NIM unit which performs the OR function. The trigger was made by the OR between the detector used (CLYC-6 or CLYC-7) and the pulser. A simple scheme of the electronic chain is sketched in Fig. 5.6.

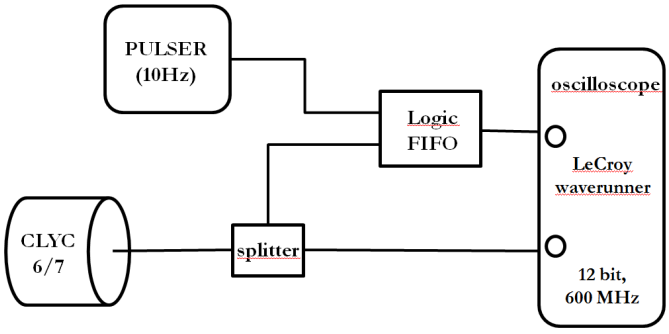

Figure 5.6: Scheme of the acquisition.

The thresholds used during the experiment correspond to γ-ray energy values of ~0.85 MeV and ~1.45 MeV for CLYC-6 and CLYC-7 respectively.

5.4.1 Predicted efficiency

As previously explained (see sec. 5.3), in a CLYC scintillator a neutron with energy E_n is detected via different reaction channels, each one resulting in a different measured effective energy E_{eff}. As a consequence, the measured energy spectrum can be viewed as an overlap of different contributions, each one associated to a reaction channel. An estimate of each contribution has been obtained by weighting the ^{241}Am-Be source neutron emission spectrum of Fig. 5.5 to the corresponding cross section. An example of a contribution, corresponding to ^{35}Cl(n,p)^{35}S which populates ^{35}S in the ground state, is shown in Fig. 5.7. The resulting spectrum (bottom panel) has been then shifted by the reaction $Q_{M,I}$ and compressed by the associated quenching factor $f_{quenching}$. The ^{6}Li contribution has also been scaled down by a factor ~4.74. This is because, in a Cs_2LiYCl_6:Ce molecule, there are 6 atoms of Cl for each atom of Li and the isotopic abundance of ^{35}Cl and ^{6}Li, in the present case, are ~75% and ~95% respectively. The top panel of Fig. 5.8 shows the various contributions to the total spectrum.

The CLYC-7 total spectrum, reported in panel d) of Fig. 5.8, is the sum of all the ^{35}Cl reaction channels, while CLYC-6 total spectrum, reported in panel e) of Fig. 5.8, includes also the ^{6}Li channel.

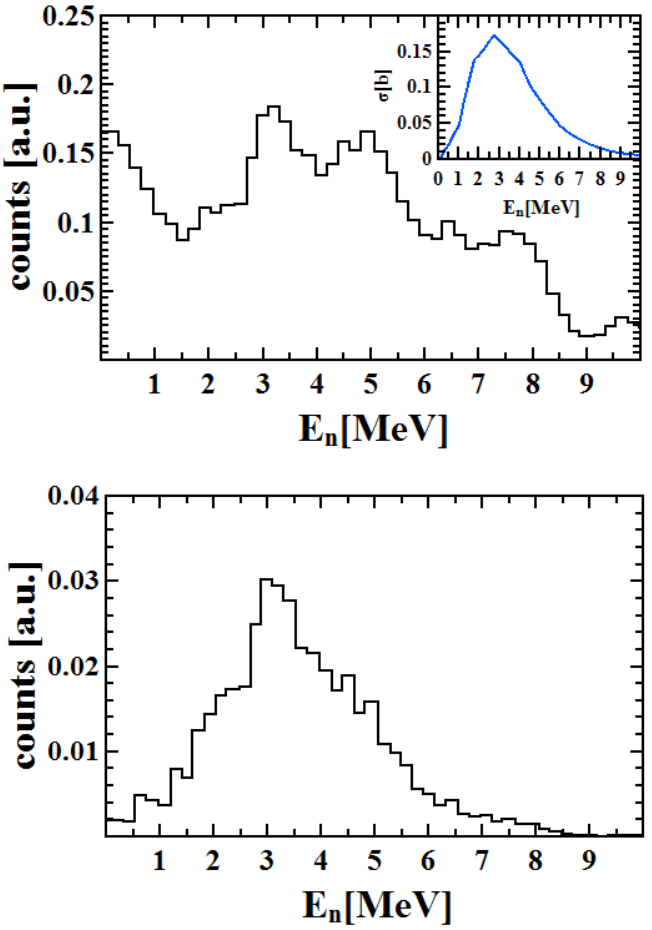

Figure 5.7: Top panel: ^{241}Am-Be source spectrum [112]. In the inset the cross section of ^{35}Cl(n,p)^{35}S, to the ground state of ^{35}S, is reported. Bottom panel: ^{241}Am-Be source spectrum weighted on that cross section.

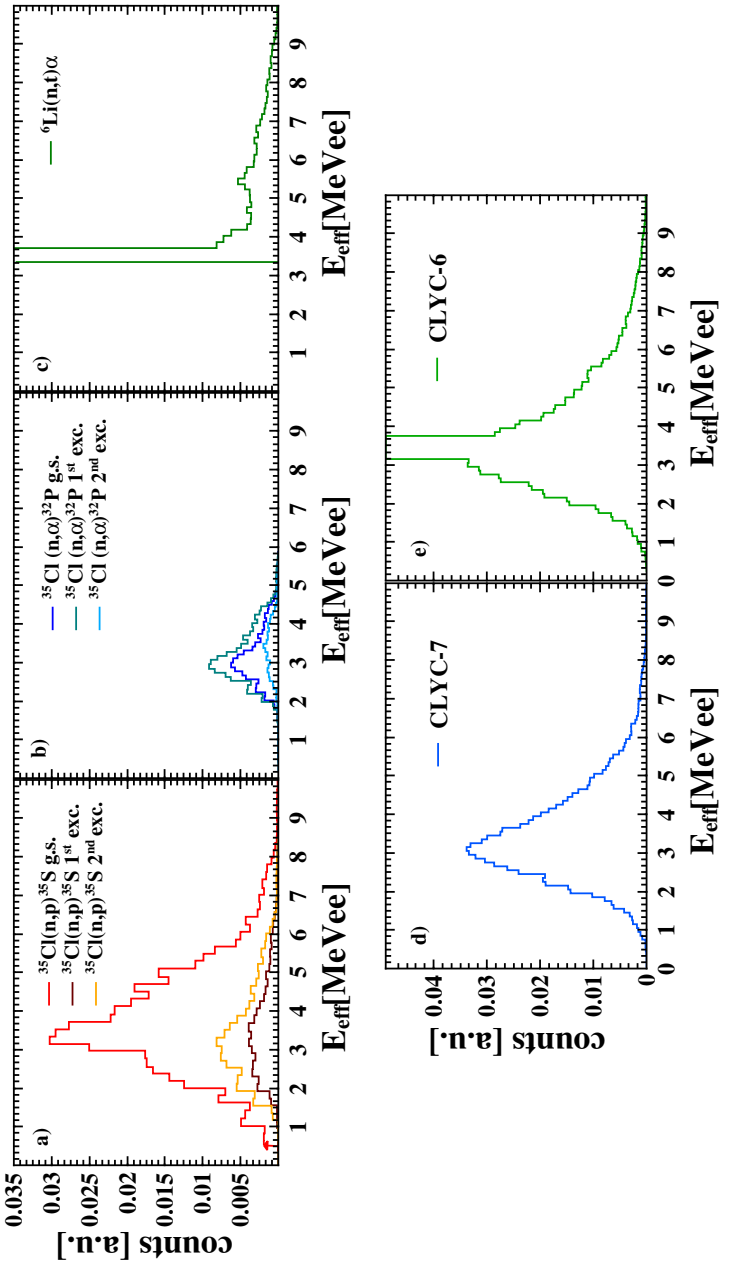

Figure 5.8: Top panel: Contributions to the total neutron spectrum associated to the different reaction channels, in terms of E_{eff}. Panels a), b) and c) show the contributions corresponding to ^{35}Cl(n,p)^{35}S, ^{35}Cl(n,α)^{32}P, and ^{6}Li(n,t)α respectively. Bottom panel: expected spectra of CLYC-6 (panel e)), obtained by summing all the seven contributions due to neutron absorption on ^{35}Cl and ^{6}Li, and CLYC-7 (panel d)), obtained by summing the contributions due to neutron absorption on ^{35}Cl only.

All of these considerations has enabled us to predict the efficiency for the two CLYC scintillators. Defining I_i the ^{241}Am-Be neutron source intensity associated to an energy range $\triangle E_i$ (note that $\sum_i I_i$=1) and $\sigma_{c,i}$ the cross section of the reaction channel c associated to $\triangle E_i$, the predicted efficiency ε_{pred} can be written as:

$$\varepsilon_{pred} = h \cdot \sum_c K_c \cdot n_c \cdot \sum_i (I_i \cdot \sigma_{c,i}), \tag{5.2}$$

where h is the CLYC thickness (1″) and K_c represents the relative amount of Cl and Li in a CLYC molecule. It assumes the value $\frac{6}{10}$ for the Cl reaction channels and $\frac{1}{10}$ for the Li (^{6}Li) channel. n_c is the particle volumetric density of ^{35}Cl or ^{6}Li:

$$n_c = \left(\rho_c \cdot \frac{N_{Av}}{A}\right) \cdot i_c, \tag{5.3}$$

where ρ_c is the mass density of the target, i_c is its isotopic abundance and N_{Av} and A are the Avogadro's constant and the mass number respectively.

Tab. 5.2 lists the predicted values of fast neutron detection efficiencies up to 10 MeV for CLYC-6 and CLYC-7. For the case of CLYC-6, the ^{6}Li contribution has been added from E_{eff} = 3.6 MeVee to E_{eff} = 10.0 MeVee, to neglect the thermal neutron energy region.

	ε_{pred}(%)
CLYC-6	1.20
CLYC-7	0.93

Table 5.2: Prediction of the fast neutron detection efficiency up to 10 MeV, obtained using eq. 5.2, for CLYC-6 and CLYC-7.

It is important to point out that the values in Tab. 5.2 are not given with an error bar as there are no tabulated errors for the cross sections of the different channels (they are calculated). Since for the spectrum of Fig. 5.5 an uncertainty of 4% is reported, we estimated that the predictions could have an error of ~10%.

5.4.2 Measured efficiency

The neutron detection efficiency ε is defined as:

$$\varepsilon = \frac{\Phi_{n\ measured}}{\Phi_{n\ emitted}}. \tag{5.4}$$

$\Phi_{n\ emitted}$ and $\Phi_{n\ measured}$ are the neutron flux emitted by the source and the measured neutron flux respectively. The emitted flux is:

$$\Phi_{n\ emitted} = A_n \cdot \triangle\ \Omega(\%),$$

where A_n is the number of neutrons emitted from the source over the whole neutron energy range per second, and $\triangle\ \Omega$ the solid angle covered by the detector.

Four different energy regions of the measured energy spectrum have been considered separately: *threshold*-energy (0.85-1.45 MeVee), *low*-energy (1.45-3.06 MeVee), *thermal*-energy (3.06-3.56 MeVee) and *high*-energy (3.56-10.0 MeVee). The efficiency ε is calculated as:

$$\varepsilon = S_{\text{threshold}} + S_{\text{low}} + S_{\text{thermal}} + S_{\text{high}}, \tag{5.5}$$

being S_k the corrected integral of the measured energy spectrum over the k-energy region, normalized by the total flux $\Phi_{n\ emitted}$:

$$S_k = \frac{n^k_{\text{tot}} - n^k_{\text{background}}}{\Phi_{n\ emitted}}.$$

The number of detected neutrons n^k_{tot}, i.e. the integral of the neutron measured spectrum over the k-energy region, and the number of neutrons from the background in the same region k $n^k_{\text{background}}$ are both corrected by the corresponding dead time.

The analysis has been performed using the software MATLAB [113]. The experimental neutron energy spectra of CLYC-6, CLYC-7 and the neutron background spectrum of the CLYC-6 are reported in Fig. 5.9 in the top, central and bottom panels respectively. Looking at the top panel, it is clear that the yellow area, the *thermal*-energy region, is completely dominated by the thermal neutron peak. This area has been determined as $\pm 5\sigma$ (being σ the standard deviation) around the centroid of the thermal neutron experimental peak of the CLYC-6 background spectrum.

S_{low} and S_{high} have been determined, for each distance, for the two detectors and are shown in Fig. 5.10.

In the *thermal*-energy region, an estimate of S_{thermal} can be obtained only for CLYC-7. Indeed the CLYC-6 spectrum is completely overwhelmed by thermal neutrons due to the presence of ^{6}Li. In CLYC-7 the contribution of ^{6}Li, considering its isotopic abundance of 1% and the amount of Li in a Cs_2LiYC_6:Ce molecule and the ^{6}Li cross section, is negligible. The S_{thermal} value is $0.15\% \pm 0.02$.

As indicated in sec. 5.4, in the *threshold*-energy region we have only CLYC-6 measurements. The $S_{\text{threshold}}$ value is $0.08\% \pm 0.01$.

For the two detectors, the S_k values are reported in Tab. 5.3.

In the error evaluation, we took into account that it is not possible to precisely determine the crystal radius and the crystal-source distance, since the crystals are encapsulated. This provide a possible systematic error estimated to be 0.001 m on the first and 0.01 m on the second one. The total error bars in Tab. 5.3 and Fig. 5.10 include also the statistical error.

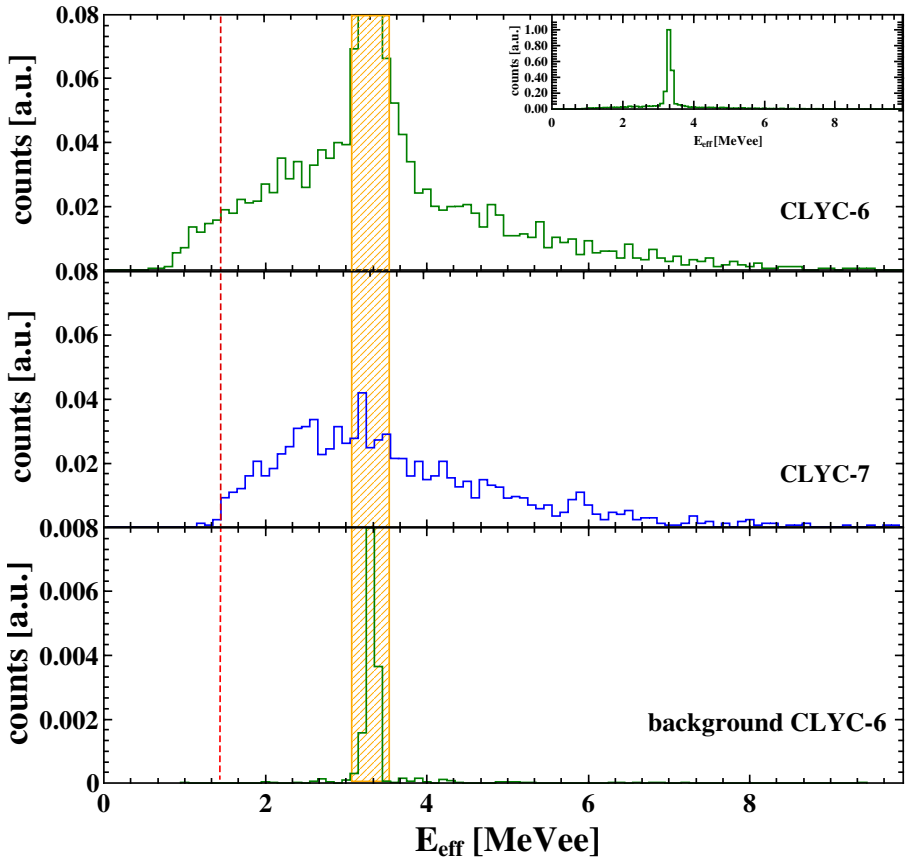

Figure 5.9: Top panel: CLYC-6 measured neutron energy spectrum ($d_{d\text{-}s}$ = 1.0 m). In the effective energy region between 3.06 and 3.56 MeVee, the spectrum is dominated by thermal neutron peak, due to the presence of ^{6}Li. In the inset the whole spectrum (CLYC-6, $d_{d\text{-}s}$ = 1.0 m) is shown. Central panel: CLYC-7 measured neutron energy spectrum ($d_{d\text{-}s}$ = 1.4 m). Bottom panel: Measured background spectrum of CLYC-6 detector. The yellow rectangle underlines the thermal energy region.

	$S_{threshold}$(%)	S_{low}(%)	$S_{thermal}$(%)	S_{high}(%)
CLYC-6	0.08 ± 0.01	0.47 ± 0.04	/	0.53 ± 0.04
CLYC-7	/	0.41 ± 0.05	0.15 ± 0.02	0.31 ± 0.05

Table 5.3: S_k values for CLYC-6 and CLYC-7. S_{low} and S_{high} are the average values between the ones obtained by all the distances.

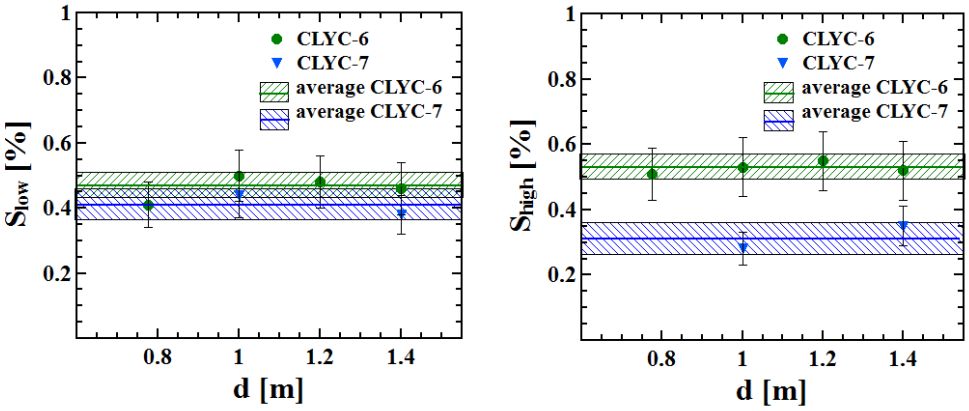

Figure 5.10: S_{low} (left panel) and S_{high} (right panel) for the different source-detector distances d for CLYC-6 and CLYC-7. The average values with their error bars are represented by the lines and the hatched areas respectively.

In the low energy region, the S_{low} values are consistent for CLYC-6 and CLYC-7, within the error bar.

In the high energy range, the difference between the two S_{high} values is mainly due to the presence, only in CLYC-6, of ^{6}Li, that enhance the neutron detection capability. To estimate ^{6}Li contribution to the CLYC-6 efficiency above 3.56 MeVee, one has to take into account the relative amount of Li and Cl and the isotopic abundances of ^{35}Cl and ^{6}Li in the crystal, the ^{241}Am-Be source intensity and the cross sections [114]. In the present case the contribution of ^{6}Li to the CLYC-6 efficiency in the high energy region (S_{high}) is estimated to be ~25%. Subtracting this contribution to S_{high} of CLYC-6, one obtains the value 0.40% which is comparable to the CLYC-7 value within 2σ.

The fast neutron detection efficiency ε can now be determined for each detector by summing all the S_k contributes (see eq. 5.5). In *threshold*, *low* and *thermal* regions, there's no reason to consider CLYC-6 and CLYC-7 different in the detection of fast neutron. Hence, the $S_{threshold}$ value, calculated for CLYC-6, can be used also for CLYC-7. Similarly, the $S_{thermal}$ value, calculated for CLYC-7, can be use also for CLYC-6. The fast neutron detection efficiency ε values, for CLYC-6 and CLYC-7, are listed in Tab. 5.4. Such values are consistent, within the error bar, with the ones predicted using eq. 5.2 (see Tab. 5.2).

	ε(%)
CLYC-6	1.23 ± 0.06
CLYC-7	0.95 ± 0.07

Table 5.4: Fast neutron detection efficiency values for CLYC-6 and CLYC-7. The two values refer to the whole energy range considered in this work (~0.85-10 MeVee).

5.4.3 Discussion

The comparison between measured and predicted spectra, without any normalization, is reported in Fig. 5.11, for CLYC-6 (top panel) and CLYC-7 (bottom panel). For both CLYC-6 and CLYC-7 we note a discrepancy at low energy (below ~3 MeV). This can be due to the fact that, in our prediction, we have neglected the contribution of the ^{35}Cl reaction channels which leave the residual nucleus in an excited state higher than the second. Due to Q_I reasons, indeed, the contribution to the measured energy spectrum associated to such reaction channels is mainly at low effective energy (see eq. 5.1). Anyway, the experimental and predicted spectra follow the same trend. This represents an important validation of our experimental fast neutron detection efficiency values, shown in Tab. 5.4.

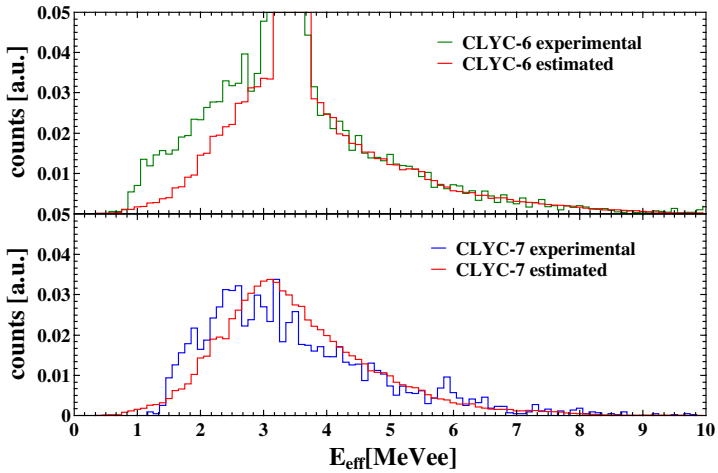

Figure 5.11: Comparison between the expected and measured total neutron spectra. The top panel shows the comparison for CLYC-6. The expected spectrum (red) is obtained by summing the contributions due to ^{35}Cl(n,p), ^{35}Cl(n,α) and ^{6}Li(n,t)α reactions of Fig. 5.8. The bottom panel shows the comparison for CLYC-7. The expected spectrum (red) is obtained by summing the contributions due to ^{35}Cl(n,p) and ^{35}Cl(n,α) reactions of Fig. 5.8.

The fast neutron detection efficiency for CLYC scintillators has been also discussed in [106, 109, 115]. In [106], a direct measurement of the fast neutron detection efficiency

for a CLYC detector, 1"x1" in size, with a natural Li concentration is presented. That efficiency, calculated as a function of the neutron energy, refers to the reaction channel ^{35}Cl(n,p)^{35}S which leaves the residual nucleus in the ground state. For a 4 MeV neutron, the efficiency value reported is 0.3%.
In [109], the intrinsic neutron detection efficiency of a CLYC-7 from 0.5 to 20 MeV has been calculated using MCNPX [116] for a 1" thick spherical shell of CLYC material with an isotropic, mono-energetic neutron source at its center. In this work, two kind of fast neutron detection efficiency have been considered, as a function of the energy: the one associated to the reaction channel ^{35}Cl(n,p)^{35}S which leaves the residual nucleus in the ground state and the total efficiency. For a 4 MeV neutron, the total efficiency value reported is 1.2%.
In [115], the neutron detection efficiency of a CLYC-6, 2"x2" in size, from 2 up to 6 MeV has been measured.
These results are not directly comparable (each other and with our results), due to the different condition considered (CLYC size, Li enrichment etc.). Anyway, they give a (coherent) idea on the order of magnitude, ~1%, of the CLYC fast neutron detection efficiency.

Part III

Study of Isospin symmetry in ^{60}Zn

CHAPTER 6

The experiment

In this chapter we will discuss the details of the experiment, performed in June 2016 at the Laboratori Nazionali di Legnaro of INFN (LNL-INFN, PD, Italy), with the aim to measure the Isospin symmetry in the nucleus ^{60}Zn. The complex experimental setup, composed by different detection arrays, will be then described, together with the data acquisition system.

6.1 Planning of the experiment

Aim of this experiment is to study the temperature dependence of the Isospin mixing in the nucleus N=Z ^{60}Zn, in order to extract the mixing probability at zero temperature. As previously discussed (see sec. 2.3.1), ^{60}Zn is in an interesting mass region: around A~60, δ_C is expected to have a sudden increase. Moreover, this nucleus allows to validate our experimental technique by the comparison of our Isospin mixing result with other existent experimental results for nuclei in the same mass region obtained with different techniques. The theoretical calculations (see Fig. 1.2 and [7]) predict, for ^{60}Zn, an Isospin mixing effect at zero temperature of ~2%.

To form the compound nucleus ^{60}Zn in a I=0 state, the following fusion-evaporation

reaction among self-conjugate nuclei was used:

$$^{32}S + ^{28}Si \rightarrow ^{60}Zn^{*}. \tag{6.1}$$

A crucial point of the experiment planning is the choice of the CN temperature and thus the selection of the beam energy, which should correspond to a reasonable fusion cross section value. Figure 6.1 shows the temperature behaviour as a function of the beam energy. The temperature T has been calculated in a simple way:

$$T = \sqrt{\frac{E^{*} - E_{IVGDR}}{a}}, \tag{6.2}$$

where E_{IVGDR} is the IVGDR centroid energy value and a is the level density parameter. We used E_{IVGDR}=16 MeV (from the systematics [117]) and a=(60/8.5). The CN excitation energy E^{*} = E_{CM} + Q is the sum of the center of mass energy E_{CM} and the reaction Q value, with Q = 6.68 MeV for the present case. The center of mass energy is obtained from:

$$E_{CM} = E_{beam}\frac{m_t}{m_p + m_t}, \tag{6.3}$$

being m_p and m_t the projectile (i.e. the beam) and the target masses respectively. It should be noted that eq. 6.2 gives just an indication of the temperature T. A more precise calculation of T, which will take into account the CN angular momentum, will be performed in the analysis.

Figure 6.2 show the fusion cross section values, calculated according to the Bass Model with PACE4 code [118, 119], as a function of the beam energy.

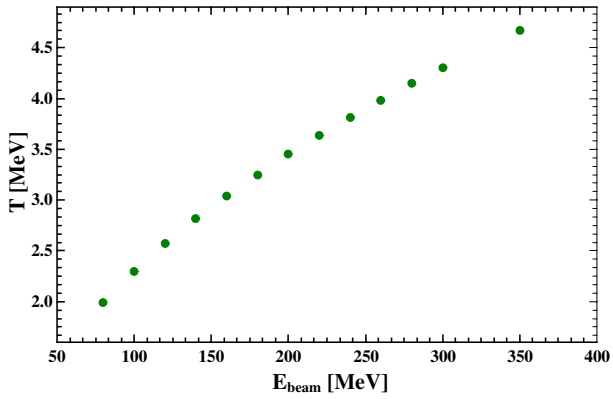

Figure 6.1: Temperature of the compound nucleus ^{60}Zn as a function of the beam energy E_{beam}.

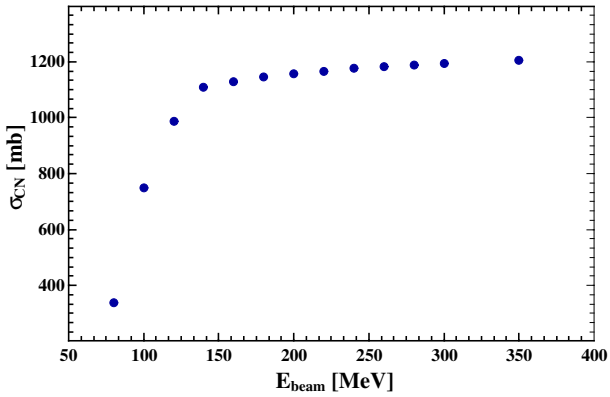

Figure 6.2: Fusion cross section of the reaction $^{32}S + ^{28}Si$ as a function of the beam energy E_{beam} (PACE4 calculation code [118, 119]).

It is worth to remember that (at least) two experimental measurements of the Isospin mixing probability α^2 at two different temperatures are required to extract the mixing probability at zero temperature, α^2(T=0), using the theoretical model of Sagawa, Bortignon and Coló ([4]), illustrated in sec. 1.3.2.

A measurement at high temperature, T>3.5 MeV, would be very interesting since it allows to experimentally test the Wilkinson hypothesis of the Isospin symmetry restoration. However, the compound nucleus formation at so high temperature would imply the opening of many evaporation channels and this would make the data analysis extremely complicated. On the other hand, low temperature values correspond to small cross sections that require long beam time. Taking into account all of these considerations, the two T values (and thus beam energies E_{beam}) we chose are reported in Tab. 6.1 with the corresponding fusion cross sections σ_{fus}, excitation energies E^* and average angular momenta $\langle J \rangle$ of the compound nucleus ^{60}Zn.

$^{32}S + ^{28}Si \rightarrow ^{60}Zn^*$				
E_{beam} [MeV]	T[MeV]	σ_{fus} [mb]	E^* [MeV]	$\langle J \rangle$ [$\hbar$]
86	**2.1**	487	47	14
110	**2.4**	884	58	21

Table 6.1: Main features of the reaction $^{32}S + ^{28}Si \rightarrow ^{60}Zn^*$: beam energies E_{beam} and temperature values T selected with the corresponding fusion cross sections, CN excitation energies E^* and CN average angular momenta $\langle J \rangle$.

The Isospin mixing probability, the subject of our measurement, is a small size quantity. For this reason, we need a reference reaction for the data analysis, leading to a

similar nucleus at the same excitation energy, but in a I≠0 state (N≠Z). We chose the following fusion-evaporation reaction:

$$^{32}S + ^{30}Si \rightarrow ^{62}Zn^{*}. \tag{6.4}$$

The IVGDR γ-decay of the nucleus ^{62}Zn, indeed, is practically not affected by the Isospin mixing and, from the comparison of data from the two reactions, it is possible to eliminate the uncertainties related to the IVGDR and statistical model parameters [120].
The two beam energies selected for this reaction, in order to populate ^{62}Zn at the same excitation energies of ^{60}Zn, are reported in Tab. 6.2 with the corresponding T, σ_{fus}, E^* and $\langle J \rangle$ parameters.

$^{32}S + ^{30}Si \rightarrow ^{62}Zn^{*}$				
E_{beam} [MeV]	T[MeV]	σ_{fus} [mb]	E^* [MeV]	$\langle J \rangle$ [ħ]
75	**2.1**	312	47	11
98	**2.4**	815	58	20

Table 6.2: Main features of the reaction $^{32}S + ^{30}Si \rightarrow ^{62}Zn^{*}$: beam energies E_{beam} and temperature values T selected with the corresponding fusion cross sections, CN excitation energies E^* and CN average angular momenta $\langle J \rangle$.

The analysis of this experiment is based on the statistical model, discussed in Part I. In particular, we assume that the statistical model parameters to describe the decay of ^{60}Zn and ^{62}Zn are the same. To ensure the validity of such assumption the average temperature, mass and shape of the two compound nuclei must be similar. The condition on mass is fulfilled by choosing two CN with A=60 and A=62, which can be considered equal in the statistical decay description. The condition on temperature is experimentally fulfilled by a suitable choice of the beam energy to use (see Tab. 6.1 and Tab. 6.2). Under these conditions, the IVGDR parameters (centroid energy, width and strength) can be considered to be the same.

Concretely, concerning the data analysis, we need at first to perform a complete study of the reactions used. It mainly consists in the analysis of the residual nuclei distribution and in the identification of the CN angular momentum distribution. This reaction analysis allows to check that the experimental data are well reproduced by the statistical model calculations, performed by using CASCADE code [121, 122]. This code will be used to extract the IVGDR parameters of ^{62}Zn (which are supposed to be the same for ^{60}Zn). Finally, we analyse the γ-decay spectrum of ^{60}Zn to deduce the Isospin mixing probability, which is now the only free parameter.

Three linearised simulated γ-decay spectra of ^{60}Zn (T~2.1 MeV) are reported in Fig. 6.3. They correspond to three different Isospin mixing conditions: absence of mixing (in

green), 2% of mixing (in red) and large mixing (in blue). Such spectra were obtained by dividing the simulated CN γ-decay spectrum by a statistical spectrum in which the E1 transition probability has a constant value (instead of the standard Lorentzian form). The simulations have been performed with CASCADE code.

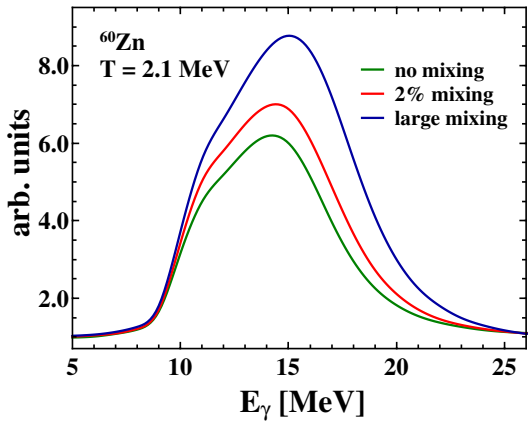

Figure 6.3: Linearised simulated spectra of ^{60}Zn (T~2.1 MeV) in the IVGDR region. They refer to three different Isospin mixing conditions: absence of mixing (in green), 2% of mixing (in red) and large mixing (in blue). The simulations have been performed with CASCADE code.

There are several statistical model calculation codes commonly used. In this work PACE4, GEMINI++ [123, 124] and CASCADE codes, based on the Hauser-Feshbach theory ([125]), are mentioned.

PACE4 and GEMINI++ use a Monte-Carlo procedure to determine the decay sequence of an excited nucleus. PACE4 is mainly indicated for the description of particle evaporation, while GEMINI++, which is also used for charged particles decay and fission-fragment emission, has been recently implemented to describe the possibility of γ-ray emission from the IVGDR [124].

The program CASCADE also performs evaporation calculations based on the statistical theory of compound nucleus reactions. Its original version (written by F. Puhlhofer) has been modified by M. N. Harakeh and then by the Washington University group according to the Isospin formalism of Harney, Richter and Weidenmüller (see sec. 1.3.1). Since it can include the Isospin formalism, CASCADE will be the code used in the analysis to deduce the Isospin mixing probability. The versions considered here (non Monte Carlo) include the Reisdorf level-density parameterization.

6.1.1 Experiment description

The experiment, proposed and accepted in February 2016, was performed at the Laboratori Nazionali di Legnaro (LNL, PD, Italy) of INFN in June 2016.
The two compound nuclei ^{60}Zn and ^{62}Zn were formed using a ^{32}S bunched beam, of intensity $I_{beam} \approx 2$ pnA, which impinged on a self-supporting targets of ^{28}Si (400 $\mu g/cm^2$) or ^{30}Si (350 $\mu g/cm^2$). The bunching of the beam was 800 ns. Moreover, in order to perform a high-energy calibration, the reaction $^{11}B + d \rightarrow^{12} C^* + n$ was used. It excites a resonance state in ^{12}C which decays with a 15.1 MeV γ-ray.
The ion beams were provided by the TANDEM tandem linear accelerator complex.
The total beam time, of 15 days, was divided as follow:

- 5 days for $^{32}S +^{28} Si \rightarrow^{60} Zn^*$ with E_{beam} = 86 MeV
- 2.5 days for $^{32}S +^{28} Si \rightarrow^{60} Zn^*$ with E_{beam} = 110 MeV
- 4 days for $^{32}S +^{30} Si \rightarrow^{62} Zn^*$ with E_{beam} = 75 MeV
- 2.5 days for $^{32}S +^{30} Si \rightarrow^{62} Zn^*$ with E_{beam} = 98 MeV
- 1 day for $^{11}B + d \rightarrow^{12} C^* + n$ with E_{beam} = 45 MeV

6.2 The experimental set-up

The main requirements for this experiment are the measurement of the γ-decay of IVGDR (high-energy γ-rays), to extract the mixing probability α^2, and the identification of the residual nuclei populated during the CN evaporation (low-energy γ-rays), to properly tune the statistical model. To fulfil these demands, a complex experimental set-up was used. It consisted in two main parts (see Fig. 6.4): an array of 25 HPGe detectors, called GALILEO [126], coupled to an array of 10 $LaBr_3$:Ce [72] scintillator detectors. In addition, two ancillary apparatuses were employed: an array of 40 Silicon detectors in $\triangle$E-E telescopes configuration, EUCLIDES [127, 128], and an array of 15 BC501A scintillator detectors, Neutron Wall [129].

6.2.1 GALILEO array

GALILEO is an Italian project active at Laboratori Nazionali di Legnaro (LNL-INFN). Its goal is to be an advanced device to address the hot topics of the present nuclear structure research [130] with the available stable beams and with the radioactive beams which will be provided, in the near future, by the facility SPES [131]. The GALILEO project, in its final configuration, will consist in a 4π high-resolution γ-ray spectrometer [126] composed

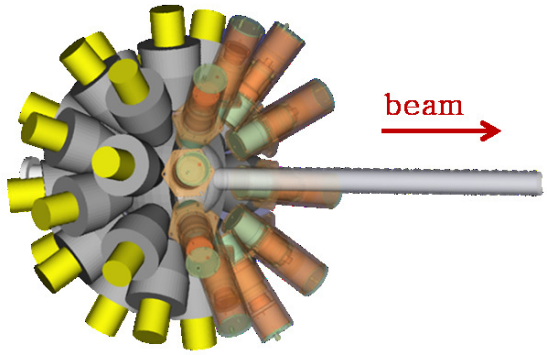

Figure 6.4: Scheme of the main parts of the experimental set-up: GALILEO array, placed at 90° and backward with respect to the beam line direction and the 10 $LaBr_3$:Ce detectors, at 70° with respect to the beam line direction.

by 30 High-Purity-Germanium (HPGe) tapered detectors from the previous GASP array, together with their anti-Compton shields, and 10 triple clusters of HPGe detectors realized with the capsules of the previous EUROBALL array. The geometry of the array was designed to maximize the photo-peak efficiency under typical in-beam medium-high γ-ray multiplicity conditions, achieving a value of about 8% [132]. The HPGe detectors are surrounded by anti-Compton shields, consisting of Bismuth Germanium Oxide (BGO) scintillators, in order to implement Compton suppression technique and reach, for the whole array, a peak-to-total ratio of 50%. An important requirement in the design is to allow for an easy integration of possible ancillary detectors, such as light charged particles detectors, scintillators, neutron detectors etc..

During the time of the experiment, GALILEO was in its first building phase. It consisted in 25 single GASP HPGe detectors (with the anti-Compton shield), arranged on 4 different rings: 5 detectors placed at 152°, 5 at 129°, 5 at 119° and the last 10 at 90° (central ring) with respect to the beam line. The detectors are placed at a distance of 22.5 cm from the target. A front-view of the 25 GALILEO detectors is shown in Fig. 6.5.

6.2.2 Readout electronics

The HPGe detectors are read out by custom advanced charge-sensitive resistive feedback preamplifiers. To reduce the numbers of signals (channels) to digitize, the electric signals from the BGO scintillators surrounding each HPGe are summed and gain-

Figure 6.5: A GALILEO array (25 HPGe) picture taken from the beam dump. The central ring, with the 10 HPGe detectors, is visible, and it hides the 15 other detectors. Taken from [126].

matched, producing a single analog signal for each BGO groups. The BGO-HPGe couples output signals are sent to digitizers. Such modules produce data which are processed in real-time by custom preprocessing boards: these perform online calculations to establish when a crystal detects a γ-ray (local trigger) and the amount of energy deposited. The timing information for each firing detector is provided during the online analysis. In summary, the pre-processing system takes data from the digitizer, extract all the useful data which can be calculated in real time and passes these parameters to the online analysis system. The pre-processing also interfaces with a Global Trigger and clock System (GTS), which manages the trigger and the synchronization. From the GTS, indeed, a clock for the digitizer and the timestamp information are derived. The validated data are sent to the Data AcQuisition (DAQ) system, were event building and online software analysis take place. A scheme of the readout system is illustrated in Fig. 6.6.

The GALILEO digitizer module employs a board developed for the AGATA array second generation of electronics, which digitises the differential input signal at 100 Msps with 14 bits of resolution. The digital output is sent to a 12-fiber optical cable by means of high-speed serial links, encoded with the JESD204A protocol and working at 2 Gbps each. Each HPGe channel has two programmable input ranges, corresponding to energy range of 0-7 MeV and 0-20 MeV for γ-rays interacting in HPGe detectors equipped

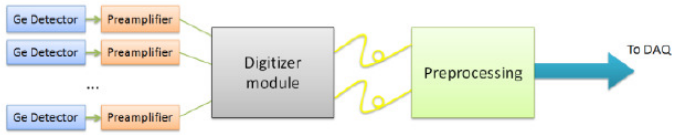

Figure 6.6: Readout system for the GALILEO array. [133].

with the GALILEO preamplifiers [130]. For the experiment we used the input range corresponding to 0-7 MeV.

The preprocessing board consists in a custom PCI express board which processes and sends data to the hosting PC trough a 4 x PC express link. The data from 36 high-speed links at 2 Gbps are processed in a Xilinx Virtex-6 Field Programmable Gate Array (FPGA), where custom algorithms select the information from events of interest and send the data to the hosting PC via the PCI express link at a sustained rate up to 400 MB/s [130].

6.2.3 Ancillary arrays

In its first building phase, the (25 HPGe) GALILEO array was coupled to the EUCLIDES charged particles array and to the Neutron Wall array. EUCLIDES, which was placed inside tha scattering chamber around the target position, covered almost all the solid angle (~80%), while the Neutron Wall, located in the forward direction with respect to the beam direction, covered a solid angle of 1π [126].

EUCLIDES array

The Si 4π array EUCLIDES (EUropean Charged Light Ions DEtector Sphere) is a light charged particle ancillary detector originally build to be used coupled with the high efficiency-array EUROBALL IV [127, 128]. Nowadays, it is one of the key GALILEO ancillary, since it provides channel selection.
The EUCLIEDES array is composed by 40 $\triangle$E-E Si telescopes: segmented and single hexagonal and pentagonal elements, forming a self-supporting structure which covers ~80% of the solid angle. The thickness of the silicon $\triangle$E and E layers are ~100 µm and ~1000 µm respectively. This allows the discrimination between light charged particles [134, 135]. The surface of the telescopes is ~10 cm^2. For a typical fusion-evaporation reaction ($v/c \sim 5\%$), the most forward placed telescope has the highest count rate, because of the kinematic enlargement of the solid angle in the center of mass reference frame. When the count rate exceeds ~25 kHz, the pile-up becomes a problem. For this reason, 5

segmented telescopes are placed in the 5 most forward positions. The 4 segments forming a telescope have equal area and individual electronic circuits. This allows to each segment to sustain a count rate up to 100 kHz, a never reached limit for an experiment. The array efficiency reaches about 60% for a single proton and about 35% for a single α-particle. A picture of the EUCLIDES array is shows in Fig. 6.7.

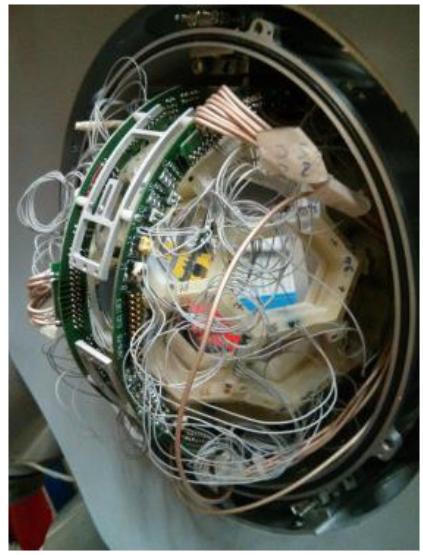

Figure 6.7: A picture of the EUCLIDES array inside the (opened) scattering chamber.

In order to protect the Si detectors from the direct exposition to heavy-ion beams, layers of different materials are added. At least the first layer in contact with the detector should be of isolating material, since the side of the detector facing the target is under voltage. Due to its mechanical resistance, a 70 μm thick UPILEX foil has been chosen. On the other side of the UPILEX foil it is necessary to add enough material to stop the scattered beam.

A fully-digitized electronics, the standard GALILEO digital ones, was implemented for the EUCLIDES array. The Si detector is coupled to a dedicated preamplifier, a 16-channel custom module developed by INFN Milano, which provides a rise time smaller than 10 ns and an ENC of 20 keV + 20 eV/pF. The output signal is then sent to the digitizer.

Fig. 6.8 shows an example of EUCLIDES $\triangle$E-E matrix, where the x-axis and y-axis indicated the energy deposited in E and $\triangle$E detector respectively.

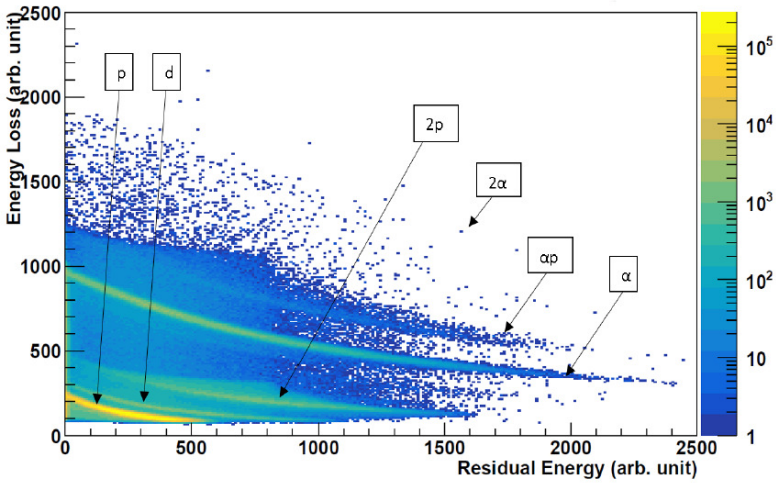

Figure 6.8: A △E-E matrix of an EUCLIDES detector [136]. The x-axis and y-axis show the energy deposited in E and △E detector respectively. Loci, corresponding to different combination of evaporated particles, are visible and are marked.

Neutron Wall array

The Neutron Wall is a BC501A liquid scintillators array: 15 hexagonal detectors. It is mounted in the forward hemisphere of GALILEO array. The hexagonal detectors (of two different types) are sub-divided into 3 segments. It results in 45 different segments with 6 different geometries, placed at 18.5°, 30.3°, 34.9°, 46.8°, 47.2°, 57.2° with respect to the beam direction. Each detector segment has a own photo-multiplier tube (the PMT Philips XP4512PA is actually used [137]) [138]. Mounted as ancillary array of GALILEO, the Neutron Wall has a focal point located 50 mm down stream from the target position. The typical distance from the focus to the front edge of each detector segment is 510 mm. For our experiment, due to the presence of the 10 $LaBr_3$:Ce detectors array, such distance was increased by 130 mm (therefore the total distance was 640 mm). Figure 6.9 shows two different views of the Neutron Wall array. It is worth to note the pentagonal detector (5 segments) placed in the center of the array (in figure) was removed, since the beam line pass through the array to reach the beam dump.

The detector cans are made of 2 mm aluminium, except for the back plate, which is 20 mm thick. The large part of this plate is covered by a 5-10 mm thick glass window, on which the PMT is mounted. At the back of each detector an aluminium collar is installed, in order to mount the detectors by connecting them to each other in a self-supporting way [138]. The part of the detector segments filled with scintillator liquid

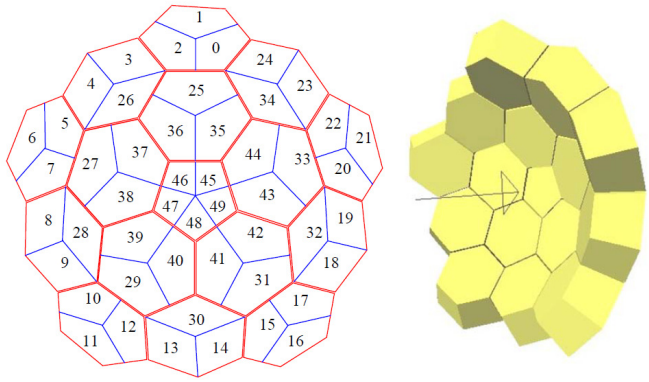

Figure 6.9: The Neutron Wall array. The figure on the left shows the array as viewed from down stream, with the official numbering scheme of the detector segments. The 3D figure on the right shows the aluminium cans of the neutron detectors as modelled in GEANT4, with the beam direction indicated by the arrow. In our case, the pentagonal detector (5 segments) placed in the center of the array was removed. Taken from [138].

is 147 mm long, with a volume of 3.2 l. The BC501A, the Neutron Wall scintillator, is a carbon–hydrogen based liquid with the composition $C_6H_4(CH_3)_2$ (xylene). The neutron detection mechanism in the liquid scintillator is mainly elastic scattering of neutrons and protons. In its slow down, the recoiling proton converts part of its kinetic energy, gained in the elastic scattering process, into internal excitations of the molecules of the liquid. In their de-excitation, these molecules emit photons of wavelengths suitable for being detected by the PMT. The absolute detection efficiency for a single neutron of energy E_n=1.5 MeV (with the array placed at a distance of 510 mm) is 0.5% for the single segment and ~23% for the whole array.

Neutron Wall has a VME readout. The detectors signals is treated by the so-called NDE202 Bartek module, an hardware dedicated to the pulse shape analysis of the PMT anode signals. It is a NIM unit implemented as a dual channel pulse shape discriminator (PSD). Each PSD channel has a constant fraction discriminator (CFD), a bipolar shaping amplifier with a zero-crossover (ZCO) detector, two time-to-amplitude converters (TAC), and a charge-to-voltage Converter (QVC) [137]. The neutrons/γ-rays discrimination is obtained trough a combined used of the ZCO time signal and the difference in measured time of flight (TOF) of neutrons and γ-rays.
An example of ZCO-TOF matrix of a Neutron Wall detector is reported in Fig. 6.10.

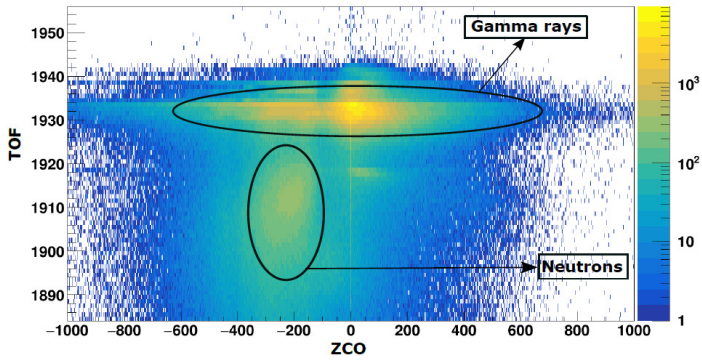

Figure 6.10: The ZCO-TOF matrix of a Neutron Wall detector [136]. Two different regions, corresponding to γ-rays and neutrons, are visible and are marked.

6.2.4 $LaBr_3$:Ce detectors array

Ten $LaBr_3$:Ce scintillator detectors, 3"x3" in size, were installed in the Galileo array. The general properties of the $LaBr_3$:Ce scintillator has been described in sec. 3.2. Anyway, it is worth to recall its typical performances in terms of energy resolution, 2.7-3.3% at 661.7 keV, and time resolution, which is $<$1 ns [72].
For this reasons, $LaBr_3$:Ce detectors represent a suitable choice to measure high-energy γ-rays from fusion-evaporation reactions, where the γ-rays/neutrons discrimination is a crucial point. The coupling of these detectors to an array which enables for the detection of low-energy γ-transitions and light particles emitted in the compound nucleus decay allows for exclusive detailed measurements of the response of the nucleus. This is the case of the whole GALILEO apparatus, which combines HPGe detectors for discrete γ-transitions, the EUCLIDES Si telescopes for light charge particles identification and the Neutron Wall for neutrons measurement [139].

Nowadays, in the GALILEO array, the 10 scintillators can be installed in two different positions: in the central ring (90°), removing the 10 HPGe detectors, or at 70° with respect to the beam direction (see Fig. 6.11). The latter solution, adopted for our experiment, allows not to loose low-energy γ-ray efficiency. As previously mentioned, to accommodate the $LaBr_3$:Ce detectors at 70° the Neutron Wall array has to be moved off (at least) 130 mm. In both the two configurations, the $LaBr_3$:Ce detectors can be placed at distances ranging from 20 to 40 cm, with absolute efficiency at 15 MeV varying from 1% to 0.25%. In our case, they were placed at 20 cm from the target position. The mechanical supports for the detectors has been fully realized, from their design to the machining, by the INFN mechanical workshops of Milano and Padova.

Figure 6.11: The 10 $LaBr_3$:Ce array. The detectors are mounted at 70° with respect to the beam line.

The fast signals coming from the $LaBr_3$:Ce detectors have been implemented into the GALILEO DAQ system trough a half-analog and half-digital readout. The analogue $LaBr_3$:Ce signals are sent to a dedicated NIM unit, called LaBr-pro, analogous to the PARISpro module (see sec. 4.2.4). The output shaped signals, which provide the energy, are sent to the digitizers. The LaBrpro ECL time outputs, instead, are converted to NIM signals (using a ECL-NIM converter), sent to a TAC modules (one for each detector) and then digitized. The digitizer channels associated to $LaBr_3$:Ce detectors were settled on an input range corresponding to an energy range 0-40 MeV.
In addition, a fully-analogue acquisition system was also employed for the $LaBr_3$:Ce array.

The two systems have been tested and compared before the experiment. The use of the GALILEO digitizer, which is not optimised for $LaBr_3$:Ce scintillators, leads to a

slight degradation in the performances in terms of energy resolution, which is ~28 keV at 661.7 keV with respect to ~24 keV measured, still in the experimental hall, with the fully-analogue system. On the other hand, the semi-digital system is able to support a higher count rate.

Since for our experiment the energy resolution is not a crucial parameter, in the data analysis we mainly used the informations from the semi-digital acquisition and kept the fully-analogue system as a backup.

Figure 6.12 shows the whole experimental apparatus used for the experiment, except for EUCLIDES, which is placed inside the scattering chamber and therefore it is not visible.

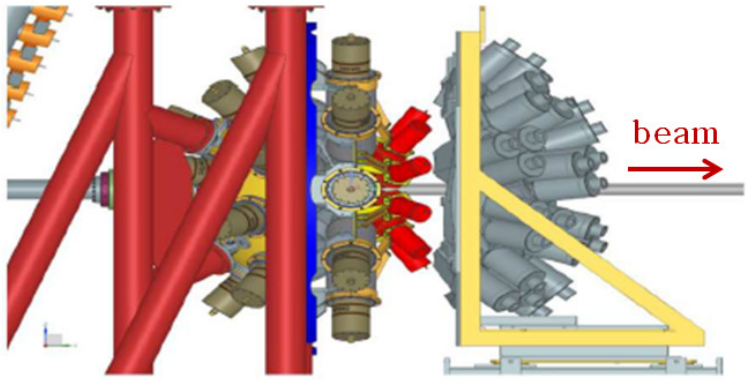

Figure 6.12: The whole experimental apparatus used for the experiment. The GALILEO array is placed in the backward hemisphere with respect to the beam direction and in the central ring (at 90°). The 10 $LaBr_3$:Ce detectors are installed at 70° and the rest of the forward hemisphered is covered by the Neutron Wall array. EUCLIDES array, which is placed inside the scattering chamber, is not visible.

6.3 The data acquisition system

The GALILEO DAQ is based on the XDAQ framework [140], a software suite that has been designed and developed to match the requirements of distributed data acquisition application scenarios of the CMS experiment [130]. The XDAQ basic unit is an executive (process), which can run one or more applications, specifically developed for the GALILEO acquisition.

Different XDAQ applications have been developed in order to manage the GALILEO data flow: readout units, filter units, builder units and merger units. All of these are

written in C++ and compiled for a Scientific Linux 6 operating system. The readout units run on the front-end PCs, equipped with the custom preprocessing board. The GALILEO hall hosts 9 machines (indicated with gal-XX in Fig. 6.13). On a machine Readout Unit (RU) and Local Filter (LF) or Builder Unit (BU), Merger Unit (MU) and Global Filter (GF) run. Two readout units are dedicated to HPGe detectors (25 channels), four to EUCLIDES Si detectors (55 channels, 40 in our case). One machine read out the other possible detectors, in this case the $LaBr_3$:Ce detectors (10 channels). Another machine is dedicated to Newutron Wall array: it reads the VME signals from the scintillators and runs the filter (which is not implemented in XDAQ). One machine is dedicated to BUs, MU and GF [141].

The RU collects data from the hardware and sent them to the local filter application, which runs dedicated algorithms to data. At different levels of the data flow chain, different kind of filter can be applied, such as Pulse Shape Analysis or track reconstruction. Data coming from different RU (and filter) are then channelled towards a builder unit, which build the event by means of a time window. A BU is dedicated to GALILEO, two to EUCLIDES and one to $LaBr_3$:Ce detectors. At the end, the data from the different BU are combined together in the MU, which also adds frames to events from the Neutron Wall array. The full event is now available and it is filtered again (a writing condition is required), in the GF, before being permanently written on the disk [141]. Figure 6.13 provides a complete scheme of the data acquisition system.

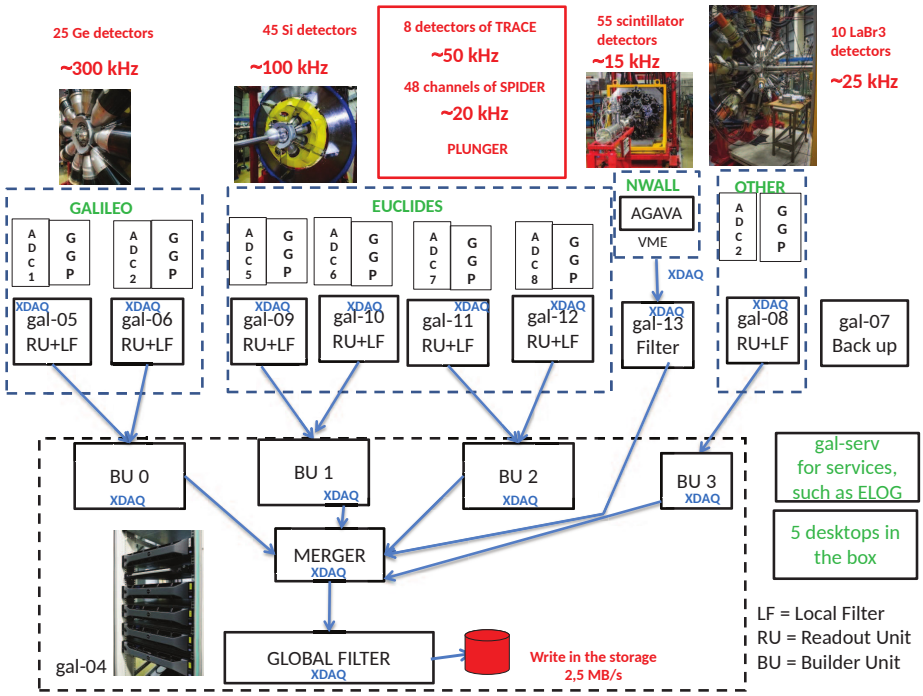

Figure 6.13: Data acquisition system scheme [142].

CHAPTER 7

Experimental setup: calibrations and response functions

In this chapter the starting point of the data analysis will be presented. It concerns the calibration of the experimental setup. It should be remembered that the data analysis of this kind of experiment generally requires several years. At the moment, we are still in the first stage. In particular, during this year, we have been focusing on the *gamma-analysis*, i.e. the analysis of the information provided by $LaBr_3$:Ce detectors (high-energy γ-rays) and HPGe detectors (low-energy γ-rays). The information provided by the particles, only mentioned in these chapters, will be integrated at a later stage.
The analysis code was written in C++ using the scientific software framework ROOT [83].

7.1 GALILEO HPGe array

As previously discussed, we will use the HPGe detectors to study the distribution of the CN residual nuclei, the nuclei populated after the CN particle decay process. This is possible by measuring the low-energy transitions of the residues to their ground state. Therefore, to characterize the GALILEO array a low-energy calibration and the low-energy efficiency estimate of the HPGe detectors have been performed. Finally, the mul-

tiplicity response of the array has been studied.
It is worth to note that all the spectra considered are Compton suppressed.

7.1.1 Energy calibration

The energy calibration of the HPGe detectors has been performed using the following radioactive sources: ^{22}Na, ^{60}Co, ^{88}Y, ^{133}Ba, ^{137}Cs and ^{152}Eu, which emit γ-rays in the energy range 0.1-3 MeV. Polynomial functions up to the fifth order, depending on the detector, have been used. Figure 7.1 shows the calibrated spectra of the 25 HPGe detectors.

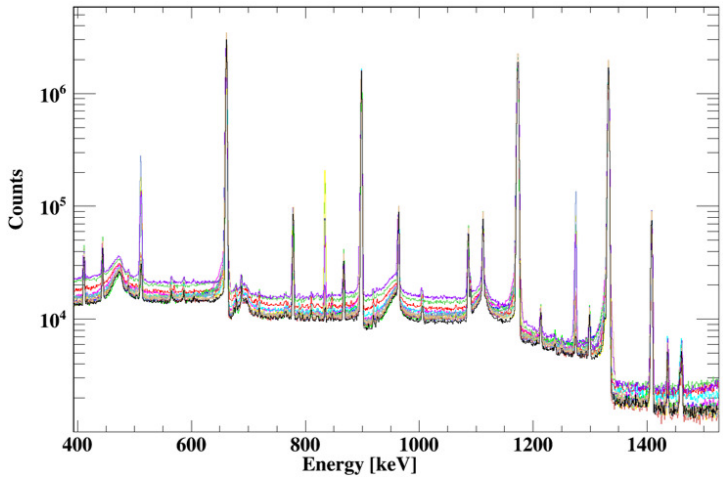

Figure 7.1: Calibrated energy spectra of the 25 HPGe detectors of the GALILEO array.

For the single detector, the measured FWHM of the 1332.5 keV peak is ~2.2 keV, consistent with what we expect for the GALILEO HPGe array. It corresponds to an energy resolution of 0.17% (at 1332.5 keV). The FWHM values as a function of the γ-ray energy for a GALILEO detector is displayed in Fig. 7.2.
The sum of the 25 HPGe calibrated spectra, whose energy resolution is comparable to the one associated to the single detector, is reported in Fig. 7.3.

During the experiment, the γ-radiation is emitted by a non-stationary object, that is the residual nucleus. For this reason, a Doppler correction (DC) must be applied to have the γ-energy spectrum in the rest frame of the projectile. The relation between the energy in the rest frame of the projectile, E_0, and the detected energy E_γ is:

$$E_0 = E_\gamma \frac{(1 - \beta \cos\theta)}{\sqrt{1 - \beta^2}} \tag{7.1}$$

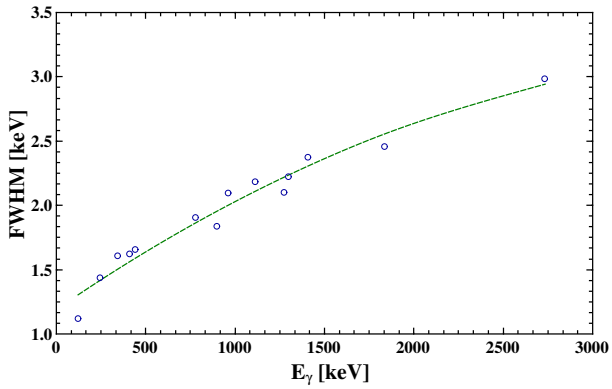

Figure 7.2: FWHM of a HPGe detector as a function of the energy.

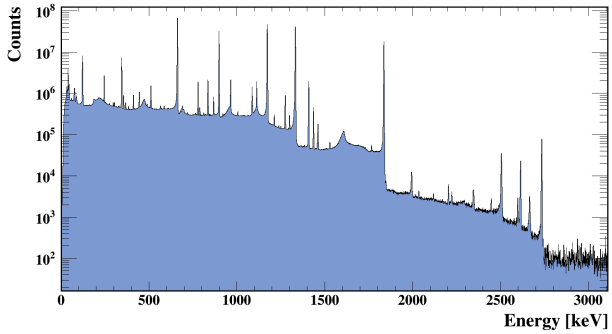

Figure 7.3: Total energy spectrum of the GALILEO array (sum of 25 the HPGe detector spectra).

where $\beta = v/c$ is the nucleus velocity and θ is the angle between the nucleus direction (assumed to be the same as the beam direction) and the emitted γ-ray.
The β values we use in the analysis for the four different reactions have been calculated using the statistical code PACE4 and are reported in Tab. 7.1.

Equation 7.1 allows us to recalibrate the energy spectra, as shown in Fig. 7.4 as an example. Anyway, the finite size of the detector, and therefore its finite angular opening $\triangle\theta$, introduces an uncertainty in the energy calculation $\triangle E_{Doppler}$, responsible for a broadening in the energy-peaks, the so-called Doppler broadening, equal to:

$$\triangle E_{Doppler} = E_0 \frac{\beta sin\theta}{1 - \beta cos\theta} \triangle \theta. \tag{7.2}$$

reaction	E_{beam}	β
$^{32}S + ^{28}Si$	86	0.041
$^{32}S + ^{28}Si$	110	0.046
$^{32}S + ^{30}Si$	75	0.036
$^{32}S + ^{30}Si$	98	0.042

Table 7.1: The β values for the 4 different reactions performed in the experiment. Such values have been calculated using the code PACE4.

Such a broadening depends on the γ-ray energy E_0, the β value of the reaction, the angular position of the detector θ and the detector angular opening $\triangle\theta$. Considering this effect, the resolution for the experiment is worse than for the calibration, where the γ-rays are emitted at rest (from sources).

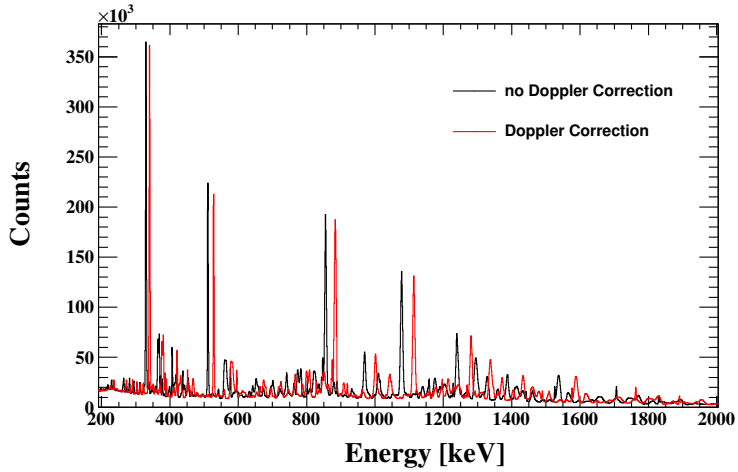

Figure 7.4: HPGe energy spectra associated to the reaction ^{32}S + ^{30}Si with E_{beam}=75 MeV, before (black spectrum) and after (red spectrum) the Doppler Correction has been applied.

7.1.2 Efficiency

The knowledge of the GALILEO array efficiency is fundamental in the determination of the relative cross section of the different residues populated during the compound nucleus decay. The calculation of the absolute photo-peak efficiency as a function of the γ-ray energy has been performed in [136], using a calibrated ^{152}Eu source. The efficiency ϵ is defined as:

$$\epsilon = \frac{N_{detected}}{N_{emitted}}, \tag{7.3}$$

where $N_{detected}$ and $N_{emitted}$ are the number of γ-rays detected and emitted respectively. In our case, $N_{emitted}$ has been calculated as:

$$N_{emitted} = A \cdot I_\gamma \cdot t. \tag{7.4}$$

Therefore, it depends on the source activity A, on the emission probability I_γ for a γ-ray with energy E_γ and on the time of measurement t.
$N_{detected}$, instead, is the area of the experimental peak of energy E_γ.

The calculation has been performed considering all the 25 GALILEO detectors. The efficiency value of the GALILEO array at ~1.3 MeV is estimated to be ~2.3%. The efficiency curve for a single GALILEO HPGe detector, obtained as $\epsilon_{tot}/25$, is shown in Fig. 7.5.

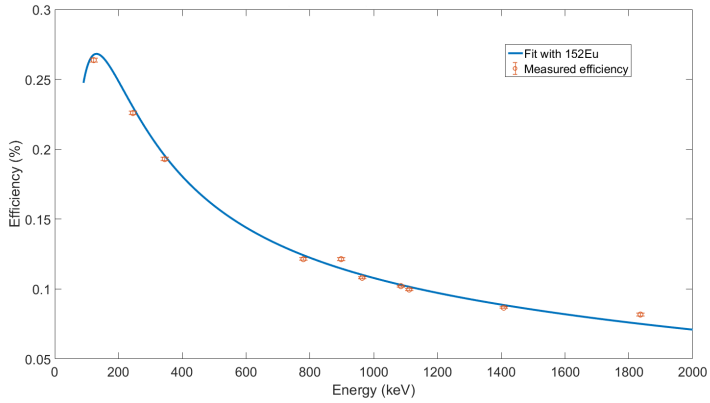

Figure 7.5: Efficiency curve for a single GALILEO HPGe detector (Compton suppressed). Adapted from [136]

7.2 $LaBr_3$:Ce detectors array

The $LaBr_3$:Ce array will be mainly use to measure the γ-decay of the IVGDR, whose energy is around 15 MeV. Since the subject of our measurement is a small size quantity, the scintillators time information plays a key role in order to reject the background. Therefore an energy calibration up to ~15 MeV and a time calibration have been accomplished. Finally, to complete the $LaBr_3$:Ce array characterization, the efficiency and the response function have been calculated.

7.2.1 Energy calibration

The calibration of the $LaBr_3$:Ce detectors have been performed over the energy range 0.6-15.1 MeV. Due to the fact that the PMT does not guarantee a good linearity over a so wide energy range, a quadratic calibration have been employed. Together with ^{137}Cs, ^{60}Co and ^{241}Am-Be (see sec. 4.3) γ-ray sources, an in beam calibration has been used: ^{11}B + d $\rightarrow$ ^{12}C + n. This reaction, indeed, excites a resonant state of ^{12}C, which decays emitting a γ-ray of energy 15.1 MeV. The high-energy calibrated spectra of the 10 $LaBr_3$:Ce detectors are displayed in Fig. 7.6. It is worth to note that, since it is emitted in flight and all the detectors are placed at the same angle $\theta = 70°$, the 15.1 MeV is detected with energy 15.36 MeV (without applying the Doppler correction). As one can see from Fig. 7.7,

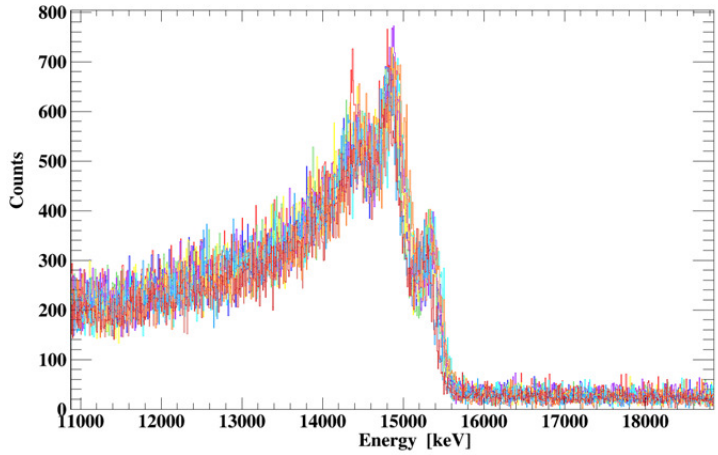

Figure 7.6: γ-ray energy spectra of the 10 $LaBr_3$:Ce detectors for the calibration reaction ^{11}B + d $\rightarrow$ ^{12}C + n. The 15.36 MeV peak (E_0, see text) is visible, together with its first and second escape peaks.

using a quadratic calibration, the difference between the calibrated energy and the real one, i.e. the residue, is very small ($\leqslant$ 100 keV for all the detectors).
The FWHM curve of a $LaBr_3$:Ce detector is shown in Fig. 7.8. It is possible to note that the FWHM values, and therefore the energy resolution, is worse than the typical values for a $LaBr_3$:Ce detector. At 661.7 keV, indeed, we measured FWHM$\approx$30 keV, while the reference value for the same detectors, obtained in laboratory (a more controlled environment than the experimental hall) using a fully-analogue chain, is 20 keV. This is due to the fact that the GALILEO digitizer is not optimized for $LaBr_3$:Ce detectors. Anyway, this does not represent a problem for this kind of experiment, since the energy resolution is not a key parameter (the IVGDR width is larger than 4-8 MeV). Such calibration will be used for the high-energy spectra ~5-15 MeV, i.e. to study the gamma decay of IVGDR.

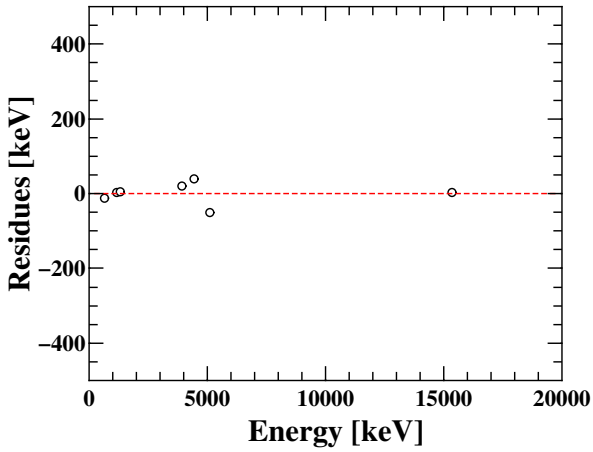

Figure 7.7: Difference between the calibrated energy (quadratic calibration) and the real one, i.e. residues, for a single $LaBr_3$:Ce detector.

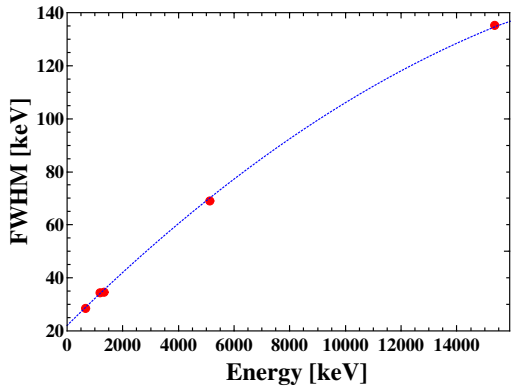

Figure 7.8: FWHM curve of a $LaBr_3$:Ce detector.

In order to be able to use also the low-energy γ-ray information of the $LaBr_3$:Ce, a linear calibration has been performed using only γ-ray sources (0.6-4.4 MeV). In this case, below 5 MeV, the residues are $<$10 keV. Anyway, as it is clear from Fig. 7.9, such calibration cannot be used at high-energy, where the residue are of the order of hundreds of keV. The low-energy calibrated spectra of the 10 $LaBr_3$:Ce detectors are reported in Fig. 7.10.

During the experiment, the sources calibration measurements has been performed before and after each one of the four CN reactions. This allowed us to check the detector stability along all the experiment and to correct any possible gain drift.

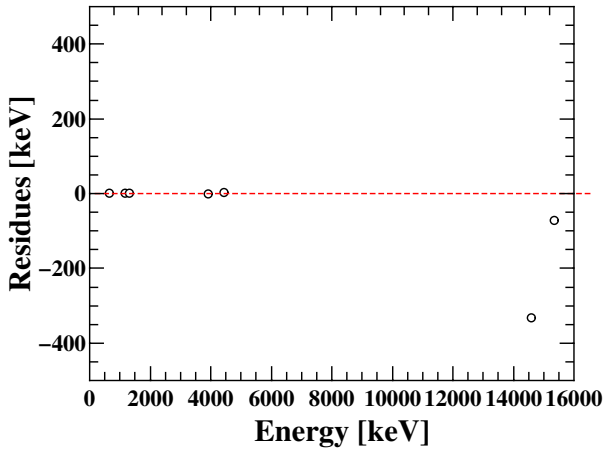

Figure 7.9: Residues of a single $LaBr_3$:Ce detector associated to a linear calibration performed using only γ-ray sources (0.6-4.4 MeV). Such calibration does not work at high energy (~15 MeV), where the residues are of the order of hundreds of keV.

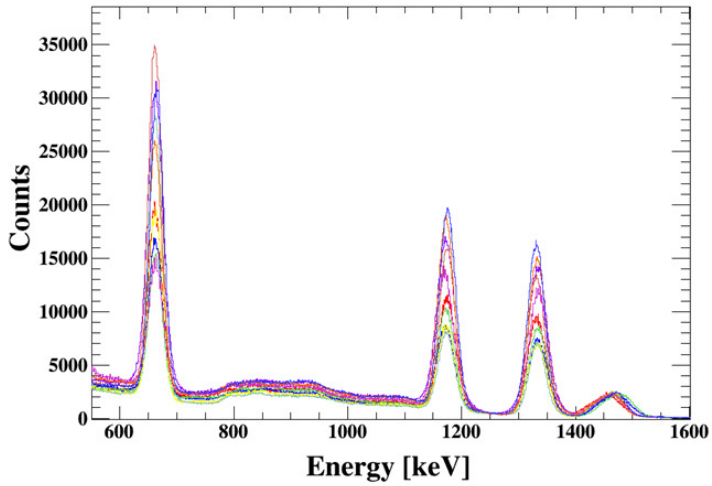

Figure 7.10: Low-energy calibrated spectra of the 10 $LaBr_3$:Ce detectors. A linear calibration (0.6-4.4 MeV) has been used.

For the beam data, the Doppler correction has been applied (see sec. 7.1.1), in order to have the spectra in the rest frame of the projectile.

7.2.2 Time calibration

The time information for each detector was provided by the LaBrpro CFD coupled to a TAC module. Each TAC module has the LaBrpro CFD signal as START and the RF beam signal (after a delay) as STOP. The time calibration of the 10 $LaBr_3$:Ce detectors has been performed by inserting a delay cable of 12 ns between the RF beam signal and the TACs input. The 10 time spectra, one for each scintillator, have been aligned, calibrated and corrected for the time walk. Since the experiment has run for several days, the detectors stability must be checked. In the left panel of Fig. 7.11 the "time-event" matrix for a scintillator, associated to the reaction ^{32}S + ^{30}Si (E_{beam} = 75 MeV), is reported; the x and y axes show the event number and the time associated to the event respectively. The time peak was not stable during the experiment: a drift of $\pm$2 ns can be observed. The time drifts have therefore been corrected, as shown by the matrix in the right panel of Fig. 7.11. Fig. 7.12 shows the same matrices of Fig. 7.11 for the reaction ^{32}S + ^{28}Si (E_{beam} = 86 MeV). This kind of correction, together with the time-walk correction and time alignments, needs to be done reaction by reaction.

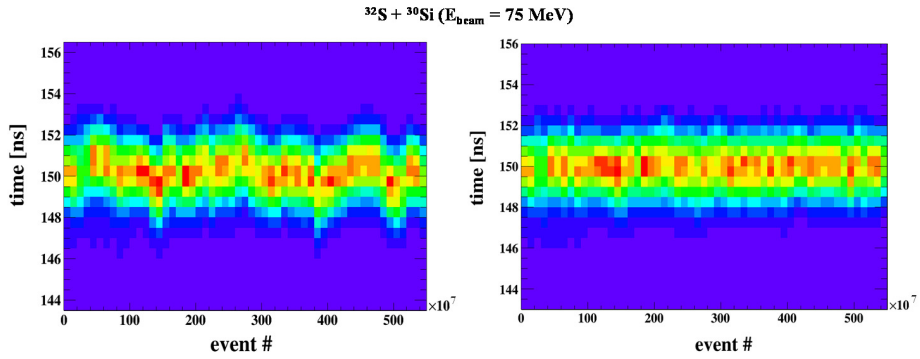

Figure 7.11: "time-event" matrix for a single $LaBr_3$:Ce scintillator, associated to the reaction ^{32}S + ^{30}Si with E_{beam} = 75 MeV before (on the left) and after (on the right) the time drift correction. The event number and the event time are reported on x and y axes respectively.

The time spectrum of a single detector for the reaction ^{32}S + $^{30}Si \rightarrow {}^{62}Zn$ (E_{beam} = 75 MeV) is displayed in Fig. 7.13. The γ-ray prompt peak can be observed, together with a bump on its left, which indicates the presence of neutrons. Indeed, the neutron events are delayed since neutrons have a smaller velocity than γ-rays. The time separation between the neutron and γ-ray peak is $\triangle T_{n-\gamma} \approx 10$ ns. This is consistent with the result of the simulations. In Fig. 7.14 a simulation of the energy spectrum (top panel) and the associated time spectrum (bottom panel) of neutrons emitted by ^{62}Zn at ~70° with respect to the beam direction (the $LaBr_3$:Ce detectors angular position) are reported. The

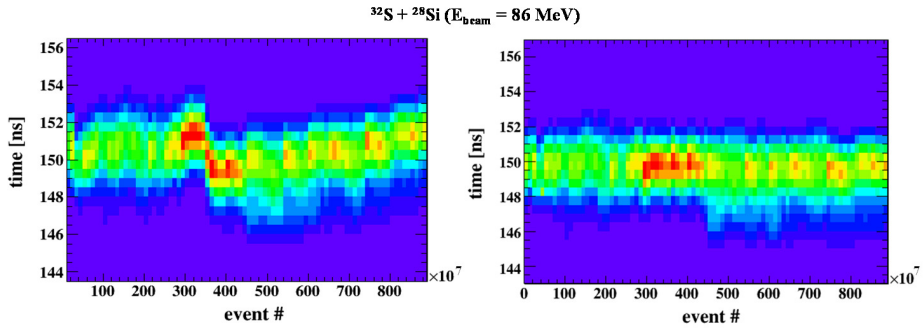

Figure 7.12: "time-event" matrix for a single $LaBr_3$:Ce scintillator, associated to the reaction $^{32}S + ^{28}Si$ with E_{beam} = 86 MeV, before (on the left) and after (on the right) the time drift correction. The event number and the event time are reported on x and y axes respectively.

energy spectrum was obtained using PACE4 code, while the time spectrum was obtained by converting the neutron kinetic energy into neutron velocity and considering the time needed to a neutron to travel 20 cm (the $LaBr_3$:Ce detectors distance from the target) with respect to a γ-ray. The energy distribution is peaked at $\approx$2 MeV, while the time distribution at $\approx$10 ns, in good agreement with the experimental $\triangle T_{n-\gamma}$. The presence of neutrons constitutes background, which must be removed by inserting a time constraint on data, i.e. a narrow time gate on the γ-ray peak.

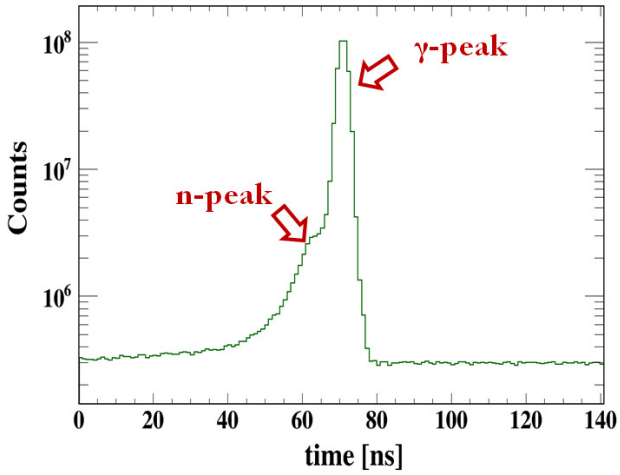

Figure 7.13: Time spectrum of a single $LaBr_3$:Ce scintillator. The γ-ray and neutron peaks are marked.

As one can see in Fig. 7.13, such γ-ray peak is large: its width is $\triangle T_{LaBr\text{-}RF} \approx$2.5 ns.

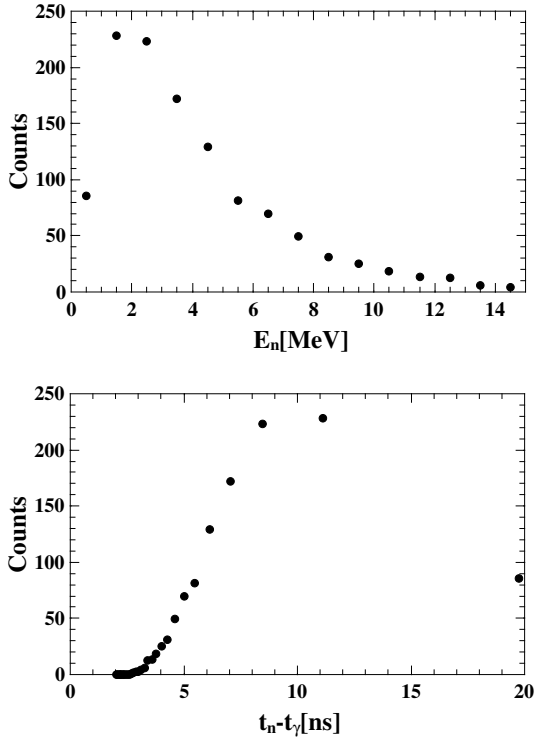

Figure 7.14: Top panel: energy distribution of neutrons emitted at ~70° by the compound nucleus ^{62}Zn (^{32}S + ^{30}Si, with E_{beam} = 75 MeV). The spectrum has been obtained using the code PACE4. Bottom panel: corresponding time distribution, obtained by converting the neutron kinetic energy into neutron velocity and considering the time needed to a neutron to travel 20 cm (the $LaBr_3$:Ce detector-target distance).

This is mainly due to RF beam fluctuation. To understand this, Fig. 7.15 shows the comparison between the time spectrum of Fig. 7.13 (in green) and another spectrum obtained as the time difference between two $LaBr_3$:Ce detector signals (in blue) both in linear and logarithmic scale (left and right panel respectively). The γ-ray peak of the latter spectrum, in which the RF beam contribution has been removed, has a width of $\triangle T_{LaBr\text{-}LaBr}$ $\approx$800 ps, which is a typical value for a $LaBr_3$:Ce scintillator. In the right panel of Fig. 7.15, one should note the double neutron peak, on the right and on the left of the prompt peak (~150 ns) in the blue spectrum. This is due to the fact that the spectrum is obtained as the time difference between two $LaBr_3$:Ce detector signals and we can have an interaction of the neutron in the first detector and γ-ray in the second or viceversa.

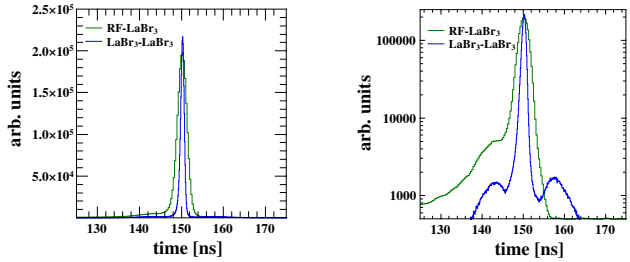

Figure 7.15: Left panel: comparison, in linear scale, between the time spectrum of a single $LaBr_3$:Ce detectors (in green), obtained as the time difference between the RF beam signal and the $LaBr_3$:Ce signal, and a second one, obtained by the time difference between two $LaBr_3$:Ce detectors (in blue). The green spectrum is the same as the one in Fig. 7.13. Right panel: the same comparison as the left panel is shown in logarithmic scale.

7.2.3 Efficiency

The absolute photo-peak efficiency for the 10 $LaBr_3$:Ce detectors has been measured with a ^{60}Co source, using the sum-peak technique. Since this source emits simultaneously two γ-rays in the same energy range (1173.2 keV and 1332.5 keV), it is possible to obtain an absolute efficiency estimate by comparing the areas of each experimental peak associated to a γ-transition (1173.2 keV or 1332.5 keV) and the sum peak, corresponding to events in which both the two γ-rays release all their energy inside the detector. To use this method we have to assume that the efficiency for a γ-ray of 1173.2 keV and 1332.5 keV is the same.

The efficiency values of the 10 $LaBr_3$:Ce detectors obtained using this methods are represented by the blue filled circles in Fig. 7.16. The average value, $\overline{\epsilon}$ = (0.22 $\pm$ 0.02)%, is in agreement with the simulated efficiency of a $LaBr_3$:Ce detector placed at 20 cm from the source position, calculated with GEANT4 code (ϵ_{sim} = 0.22%).

It is worth to note that, for a γ-ray of 1332.5 keV, the absolute photo-peak efficiencies of the whole $LaBr_3$:Ce array (~2.2%) and the whole GALILEO array are almost equivalent.

7.2.4 Response function

The detection process induces a deformation in the γ-ray spectrum emitted by the compound nucleus. This occurs because the detector photo-peak efficiency changes with the γ-ray energy. In order to be able to compare the simulated γ-ray spectrum and the detected one, such deformation, the so-called response function, has been calculated for

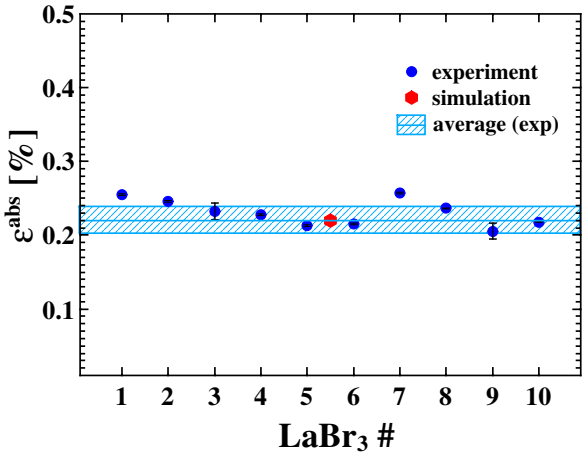

Figure 7.16: $LaBr_3$:Ce detectors efficiency. The blue circles represent the measured efficiency values of the 10 detectors, while their average value and the corresponding standard deviation are represented by the line and the hatched areas respectively. The red hexagon indicates the result of an efficiency simulation for a $LaBr_3$:Ce detector, performed using GEANT4 code.

the $LaBr_3$:Ce array following a standard procedure reported in [21, 143]. We simulated the interaction in the $LaBr_3$:Ce detectors of monochromatic γ-rays starting from energy 1 MeV up to 30 MeV, obtaining 30 different simulated spectra, as the ones reported in Fig. 7.17. These spectra were considered as the columns of a 30 x 30 matrix, where each element (E_{det}, E_γ) represents the probability to detect a γ-ray with energy E_{det} when a γ-ray of energy E_γ interacts. Such matrix is the $LaBr_3$:Ce array response function.

Calling v the emitted γ-ray spectrum, w the detected one and A the response function matrix, the following relation can be written:

$$w = A \times v. \tag{7.5}$$

Therefore, to properly compare the γ-ray emitted and the simulated one, the latter must be folded with the response function. The dashed curve of Fig. 7.18 has been obtained following this procedure.

7.3 Multiplicity response

In this kind of experiment, an important information to know is the compound nucleus spin distribution, since it represents a fundamental input parameter for the statistical

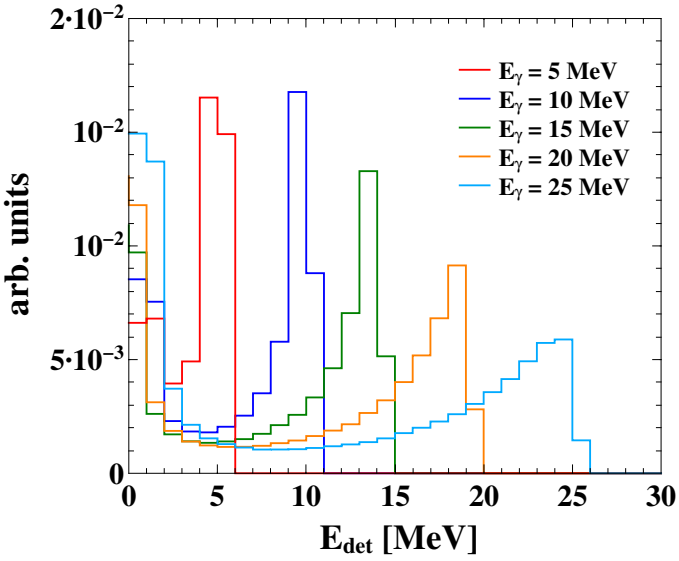

Figure 7.17: Simulated spectra of the interaction in the $LaBr_3$:Ce array of monochromatic γ-rays of energy E_γ, for 5 different values of E_γ.

model calculations. As discussed in Appendix A, it could be extracted by counting the number of γ-rays emitted in the compound nucleus decay, i.e. the so-called γ-ray multiplicity M_γ. However, the number of γ-rays detected by the apparatus, the so-called γ-ray fold F_γ, is obviously different and generally less than M_γ, because of the apparatus efficiency. In particular, a specific F_γ corresponds to a M_γ distribution. Therefore, it is important to know the conversion between F_γ and M_γ.

In our case, for the GALILEO array $P(F_\gamma, M_\gamma)$ was experimentally determined using a ^{60}Co source, since it emits two γ-rays in cascade. We registered an event only if the 1332.5 keV γ-ray from the ^{60}Co source (placed in the target position) results in a full energy peak, ensuring that exactly one γ-ray of energy 1173.2 keV has been emitted and we stored the associated GALILEO fold. Hence, the fold spectrum corresponds to the response of the array to the γ-ray multiplicity M_γ=1 (at the energy 1173.2 keV). The response to the multiplicity M_γ=k is generated by randomly selecting k events from the previously stored data and summing up their fold.
The $P(F_\gamma, M_\gamma)$ distributions for the GALILEO array are shown in Fig. 7.20, for three different F_γ conditions.

It is worth to note that P(1, 1) corresponds to the detection efficiency (ϵ_{det}) of the GALILEO array at 1173.2 MeV. Its value is reported in Tab. 7.2, together with the photopeak efficiency (ϵ_{ph}) at the same energy, obtained by counting the number of 1173.2 keV

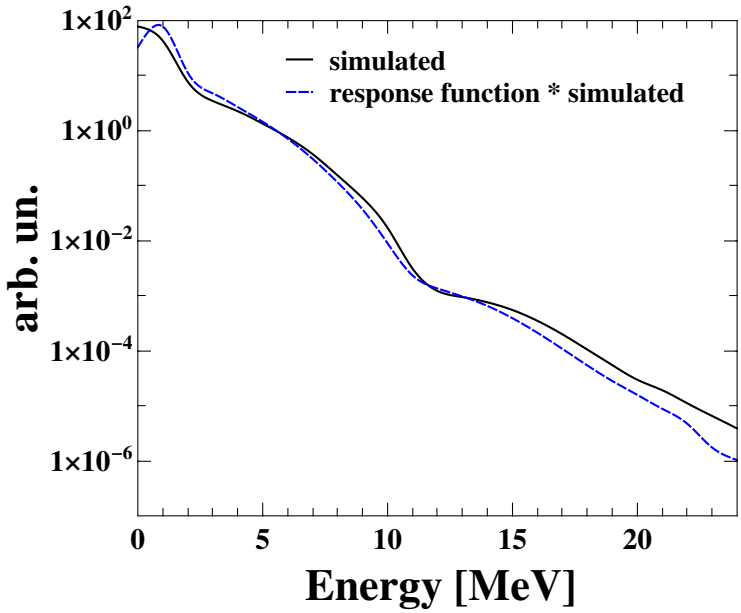

Figure 7.18: γ-ray spectrum simulated using the statistical code CASCADE, before (black solid line) and after (blue dashed line) the application of the $LaBr_3$:Ce array response function. The two spectra have been normalized between 5 MeV and 7 MeV.

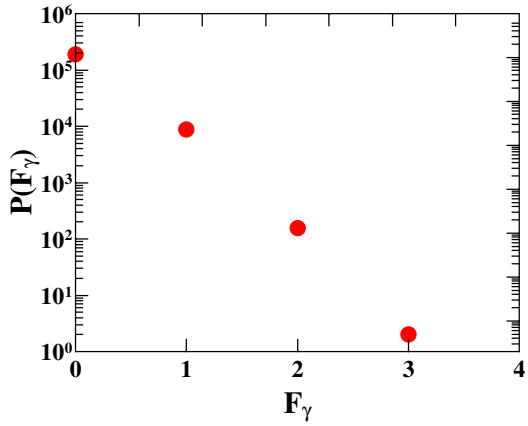

Figure 7.19: F_γ distribution associated to multiplicity M_γ = 1, measured with a ^{60}Co source (using the method described in the text).

full-energy peaks stored in coincidence with the reference 1332.5 keV γ-ray. As one can see, the ϵ_{ph} value is in good agreement with the one reported in sec. 7.1.2 for a γ-ray

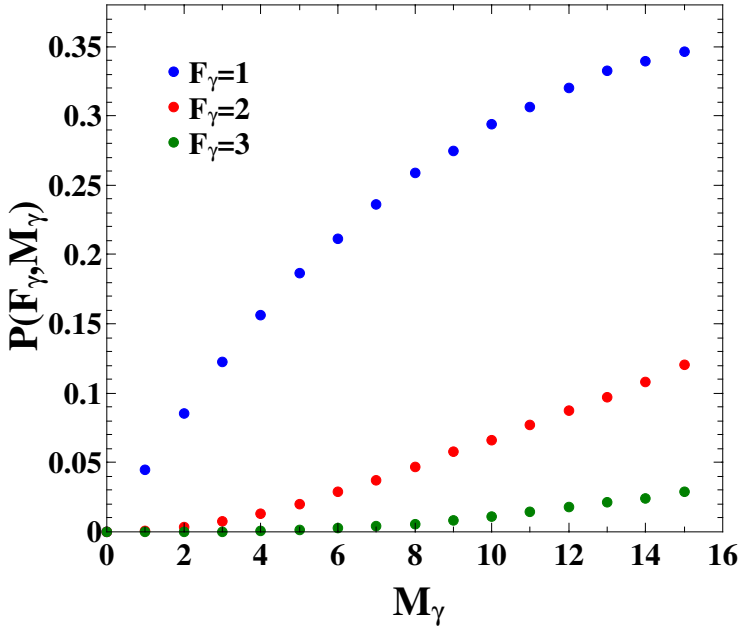

Figure 7.20: Probability distributions $P(F_\gamma, M_\gamma)$ to trigger F_γ γ-rays in the GALILEO array by a cascade of M_γ γ-rays, calculated using a ^{60}Co source. Three different F_γ values have been considered.

in the same energy range. It is important to remember that the GALILEO detectors are Compton suppressed.

	GALILEO array
ϵ_{ph}	2.3%
ϵ_{det}	4.5%

Table 7.2: Photo-peak efficiency and detection efficiency of the GALILEO array for a γ-ray of energy 1173.2 keV, calculated using a ^{60}Co source.

In principle, if $F_\gamma \ll N$ (number of detectors), the relation between F_γ and M_γ can be described by the binomial distribution:

$$P(F_\gamma, M_\gamma) = \binom{M_\gamma}{F_\gamma} \epsilon_{det}^{F_\gamma} (1 - \epsilon_{det})^{M_\gamma - F_\gamma}. \tag{7.6}$$

Therefore, knowing the detection efficiency ϵ_{det}, for the GALILEO array $P(F_\gamma, M_\gamma)$ has been determined also trough eq. 7.6. This is possible since the intra-detector scattering

probability is considered negligible, due to the presence of the anti Compton shields and to the low expected multiplicity.

As one can see in Fig. 7.21, the $P(F_\gamma, M_\gamma)$ distributions obtained with the two techniques described above are practically identical.

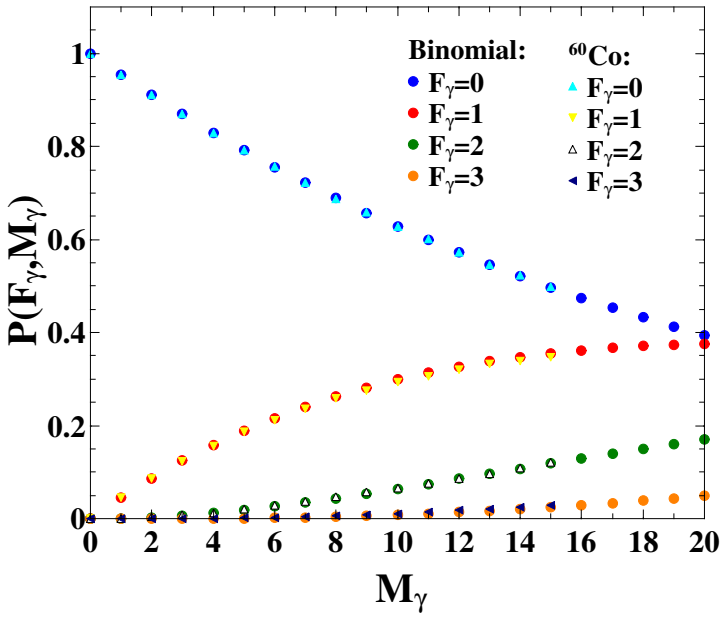

Figure 7.21: Comparison between $P(F_\gamma, M_\gamma)$ calculated by using the ^{60}Co method (filled circles) and the binomial distribution technique (triangles). Four different F_γ values have been considered.

The binomial distribution method (eq. 7.6) has then been used to calculated the conversion F_γ and M_γ for the $LaBr_3$:Ce detector array. The detection efficiency ϵ_{det} of the array at 1.3 MeV has been simulated using GEANT4 code and it is reported Tab. 7.3, together with the photo-peak efficiency of the array.

	$LaBr_3$:Ce array
ϵ_{ph}	2.2%
ϵ_{det}	4.2%

Table 7.3: Photo-peak efficiency and detection efficiency of the $LaBr_3$:Ce array for a γ-ray of energy 1173.2 keV, simulated using GEANT4 code.

The $P(F_\gamma, M_\gamma)$ distributions for the $LaBr_3$:Ce array are shown in Fig. 7.22, for three dif-

ferent F_γ conditions.

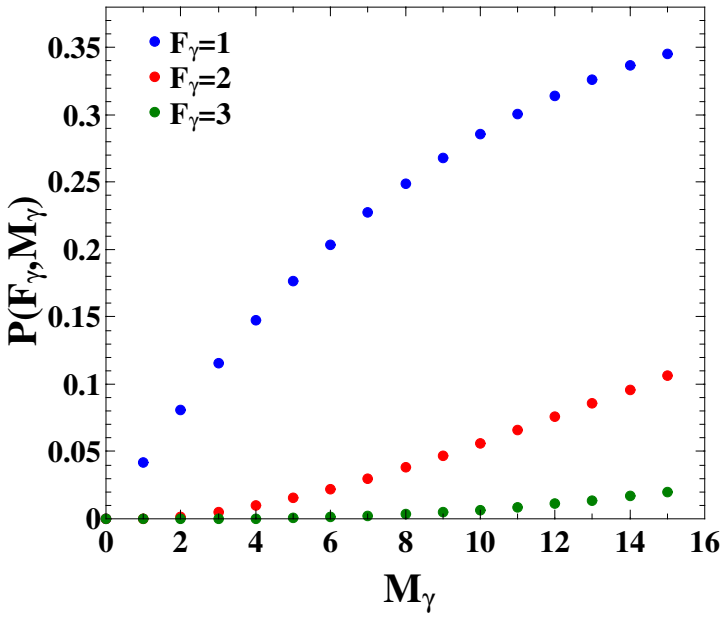

Figure 7.22: Probability distributions $P(F_\gamma, M_\gamma)$ to trigger F_γ γ-rays in the $LaBr_3$:Ce detectors array by a cascade of M_γ γ-rays, calculated using eq. 7.6. Three different F_γ values have been considered.

A kind of event which is important for the analysis corresponds to a coincidence between $LaBr_3$:Ce array and GALILEO array. Since the detection of a γ-ray in the GALILEO array can be considered statistically independent on the detection of a γ-ray in the $LaBr_3$:Ce, the probability distribution $P(F_\gamma, M_\gamma)$ associated to the coincidence between $LaBr_3$:Ce array and GALILEO array was obtained by multiplying the $P(F_\gamma, M_\gamma)$ of the two arrays, as shown in Fig. 7.23.

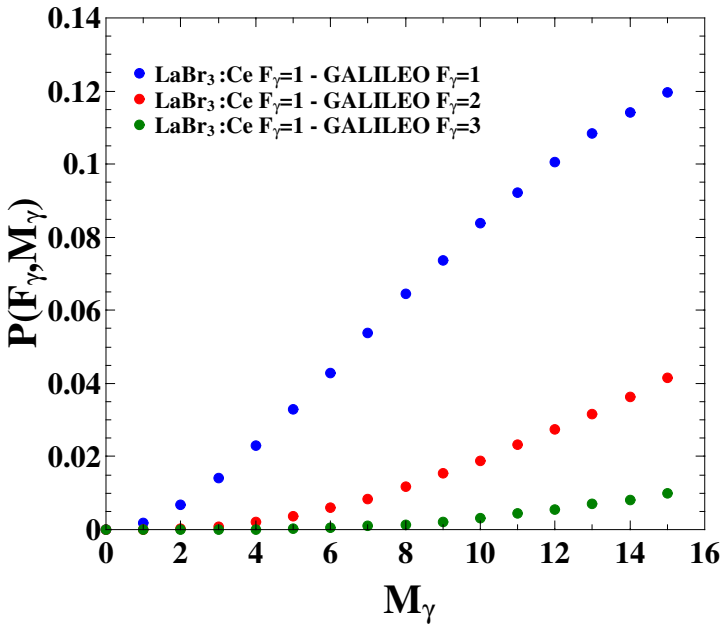

Figure 7.23: Probability distributions $P(F_\gamma, M_\gamma)$ associated to the coincidence between GALILEO array and the $LaBr_3$:Ce detectors array by a cascade of M_γ γ-rays, calculated using eq. 7.6. Three different coincidence conditions have been considered.

CHAPTER 8

Preliminary analysis

In this chapter we will report on the preliminary data analysis, focused on the information provided by $LaBr_3$:Ce and HPGe detectors. As introduced in Chapter 6, the first step of the analysis is the study of the fusion-evaporation reactions. In particular, we concentrated on the reaction: $^{32}S + ^{30}Si \rightarrow ^{62}Zn$ (E_{beam} = 75 MeV), a reference reaction, in which the γ-decay of the IVGDR is practically not affected by the Isospin mixing. Therefore, this reaction will be used to extract the IVGDR parameters. The spin distribution of the compound nucleus ^{62}Zn, populated with this fusion reaction, and the residual nuclei populated during the CN evaporation process have been identified. This study is fundamental and it provides a check on the statistical model, which constitutes the condition for the Isospin mixing degree determination. Finally, the high-energy spectrum (in the IVGDR region) has been analysed and, to give an idea of the work to be done in the forthcoming future, it has been preliminarily compared to the one obtained by statistical model calculation.

8.1 Spin distribution

In order to analyse the fusion-evaporation reaction: $^{32}S + ^{30}Si \rightarrow ^{62}Zn$ (E_{beam} = 75 MeV), the angular momentum distribution (or spin distribution) of the compound nucleus ^{62}Zn has been identified. As previously explained, the number of γ-rays emitted during the

CN de-excitation process, i.e. the γ-ray multiplicity M_γ, is expected to be directly related to the angular momentum of the compound nucleus. Therefore a crucial point is the measurement of the multiplicity distribution $P(M_\gamma)$ which, from the experimental point of view, is based on the measurement of the fold distribution $P(F_\gamma)$.

The conversion between the experimental fold distribution and the spin distribution has been performed in two steps. The first one concerns the conversion between fold distribution and multiplicity distribution [64, 144]. The multiplicity distribution for fusion events can be assumed to have a semi-triangular form:

$$P(M_\gamma) = \frac{2M+1}{1+exp\,[(M-M_0)/\delta_m]}, \tag{8.1}$$

where M_0 is the inflection point of the distribution and δ_m the diffuseness. Such distribution was folded with the response function $P(F_\gamma, M_\gamma)$ for the GALILEO array (without any condition on $LaBr_3$:Ce energy, see sec. 7.3) generating the corresponding fold distribution $P(F_\gamma)$:

$$P(F_\gamma) = \sum_M P(F_\gamma, M_\gamma) P(M_\gamma) \tag{8.2}$$

The two $P(M_\gamma)$ parameters M_0 and δ_m were varied, in order to obtain the simulated fold distribution which better reproduces the experimental one. To avoid possible contamination of non-fusion events, only folds higher than 1 ($F_\gamma > 1$) were considered in the fit. However, looking at the HPGe energy spectra we estimate that non-fusion events are a very small percentage of data.

Fig. 8.1 shows the comparison between the experimental fold distribution and the one obtained with the method just described. The extracted values of M_0 and δ_m are reported in Tab. 8.1.

$^{32}S + {}^{30}Si \rightarrow {}^{62}Zn$ (E_{beam} = 75 MeV)	
M_0	7.0
δ_m	0.6

Table 8.1: Fitted values of M_0 and δ_m for the extraction of the multiplicity distribution $P(M_\gamma)$.

The corresponding multiplicity distribution is displayed in Fig. 8.2. It represents an approximation of the multiplicity distribution associated to the γ-decay of the CN ^{62}Zn (populated at E^* = 47 MeV, corresponding to E_{beam} = 75 MeV). The average value of $P(M_\gamma)$ is $\langle M \rangle$ = 4.7.

The limit of this method to determine $P(M_\gamma)$ is that our response function $P(F_\gamma, M_\gamma)$ takes into account only the γ-ray detection efficiency at ~1.2 MeV, while the energy of the emitted γ-rays is expected not to be constant, even though in the same energy range.

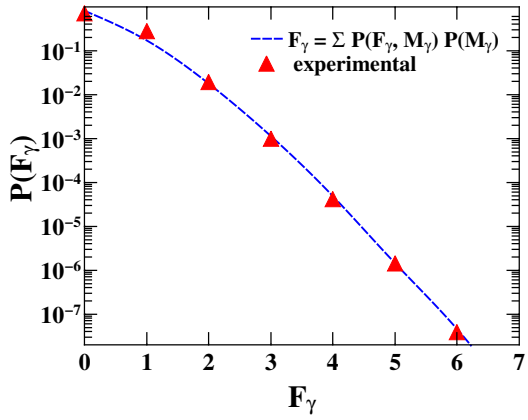

Figure 8.1: Comparison between the experimental fold distribution (filled triangles) and the simulated fold distribution obtained with the multiplicity distribution method (dashed line) described in the text.

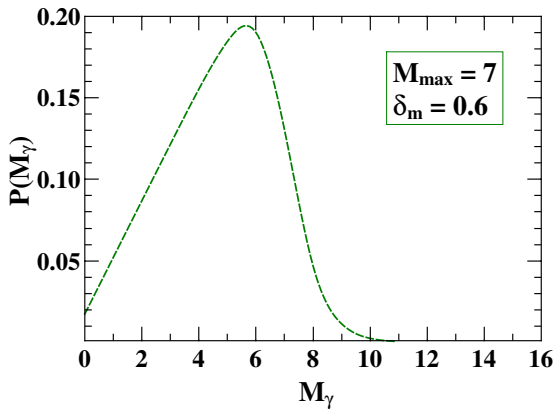

Figure 8.2: Semi-triangular multiplicity distribution (eq. 8.1 with $M_0 = 7$ and $\delta_m = 0.6$). It represents an approximation of the multiplicity distribution associated to the decay of CN ^{62}Zn ($E^* = 47$ MeV, corresponding to $E_{beam} = 75$ MeV).

The second step concerns the conversion of the multiplicity distribution into the spin distribution. The angular momentum J is given as follows:

$$J = 2N(E2) + k, \tag{8.3}$$

where N(E2) is the multiplicity of the E2 γ-rays coming from the decay of the rotational band (yrast line) and k takes into account the angular momentum removed by statistical γ-rays and particle evaporation. However, in the experiment no distinction could be made between the E2 photons and the other photons. Therefore, the following relation was considered:

$$J \approx 2M_{\gamma} + k, \tag{8.4}$$

In the present case the value $k = 2$ has been used. Indeed, the average value of the spin distribution obtained with $k = 2$, $\langle J \rangle \approx 11\ \hbar$, is in good agreement with the average values of the spin distributions calculated with the statistical codes GEMINI++, CASCADE and PACE4 (all $\langle J \rangle \approx 11\ \hbar$).
The obtained angular momentum distribution P(J) is shown in the left panel of Fig. 8.3. Additionally, in the right panel, the angular momentum distributions corresponding to different fold conditions are reported. As one can see, $F_{\gamma} = 1$ events are sensitive to low angular momentum, while $F_{\gamma} = 2$ and $F_{\gamma} = 3$ are sensitive to growing angular momentum. This can be better understood looking at Fig. 8.4, where the distribution corresponding to folds 1, 2 and 3 were normalized in the J range 20-40 $\hbar$. F_{γ} = 4-8 are associated to negligible statistics (see Fig. 8.3).

Finally, the obtained distribution has been compared with the ones simulated using GEMINI++, CASCADE and PACE4 statistical codes (see Fig. 8.5). The four curves have been normalized to the fusion reaction cross section. As one can see, the curves follow the same trend.

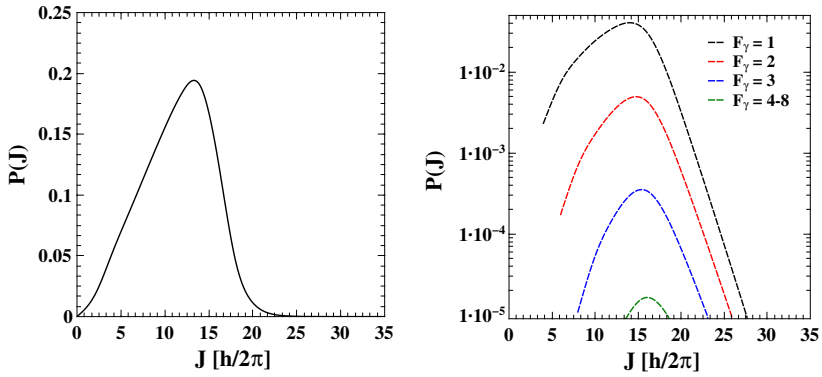

Figure 8.3: Left panel: angular momentum distribution obtained using the multiplicity distribution method. Right panel: angular momentum distributions corresponding to different fold conditions.

As one can see from the distributions, the range of possible angular momenta, and

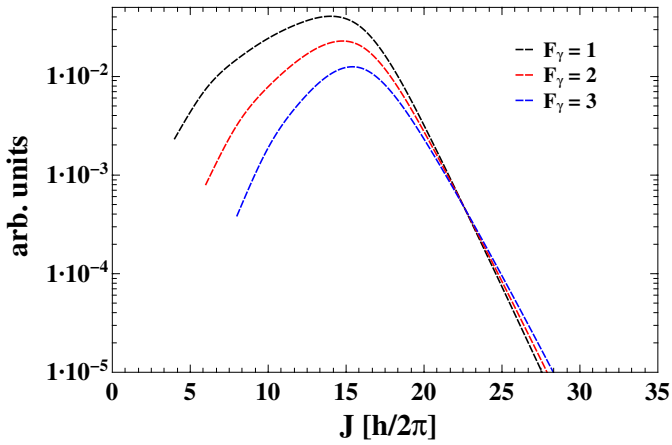

Figure 8.4: Angular momentum distributions associated to $F_\gamma = 1$. These distributions have been normalized in the J range 20-40 ħ.

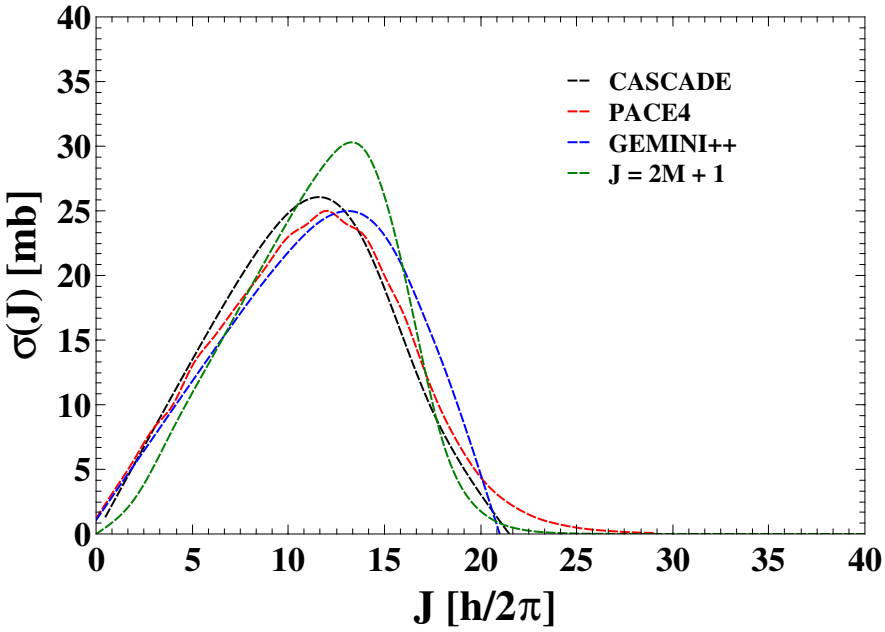

Figure 8.5: Spin distributions obtained using the multiplicity distribution method (green curve) compared to the spin distributions calculated with the statistical codes CASCADE, PACE4 and GEMINI++.

thus of rotational energy values, for the compound nucleus is small. The yrast line of the CN, calculated with GEMINI++ code, is shown in Fig. 8.5. The red rectangle indicates the region of interest: the rotational energy window associated to the range of possible angular momenta populated in this case. In particular, the rotational energy associated to the maximum J is $E(J_{max}) \sim 7$ MeV.

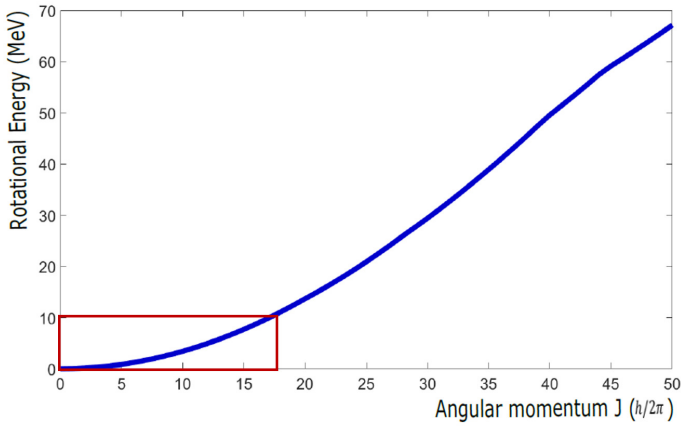

Figure 8.6: Yrast line of ^{62}Zn, calculated using the code GEMINI++. The red rectangle indicates our region of interest: the rotational energy window associated to the range of possible angular momenta populated in the reaction ^{32}S + ^{30}Si $\rightarrow$ ^{62}Zn with E_{beam} = 75 MeV.

8.2 Analysis of residual nuclei population

During the decay process, the compound nucleus emits mainly particles until its excitation energy remains above the particle binding energy and then it can only emits γ-rays. The nuclei populated after the particle emission are called residual nuclei, or residues. The low-energy γ-ray transitions associated to the de-excitation of these nuclei were used to identify the residues and to extract, using their intensity, the residues distribution. These discrete γ-transition were measured using the HPGe detectors.
The residues distribution can also be calculated using the statistical model and the comparison between the experimental and simulated distributions provides a check on the reliability of the model.

The γ-ray spectrum of the GALILEO array, associated to the reaction ^{32}S + ^{30}Si $\rightarrow$ ^{62}Zn with E_{beam} = 75 MeV, is displayed in Fig. 8.7. Using the RadWare [145] and NuDat [146] archives as a reference, the main intense peaks were identified. The four main residues produced during the ^{62}Zn decay are reported in Tab. 8.2, together with the corresponding

decay channels. As one can see in Fig. 8.7, other nuclei, indicated by the rectangles, are clearly present in the spectrum although they are not associated to ^{62}Zn decay. They are associated to the fusion between the beam and a target contaminant. This issue will be addressed in subsec. 8.2.1.

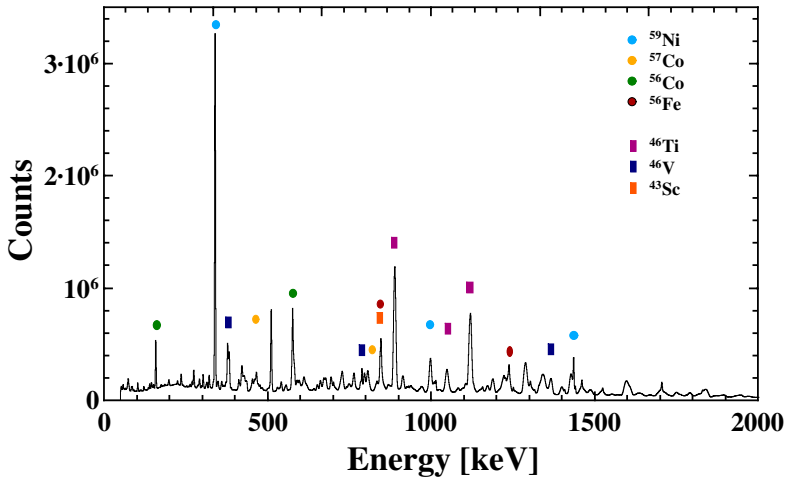

Figure 8.7: Energy spectrum of the GALILEO array associated to the ^{62}Zn decay (E^* = 47 MeV, corresponding to E_{beam} = 75 MeV). It has been produced without any condition in the sort code. The main residual nuclei are marked.

$^{32}S + {}^{30}Si \rightarrow {}^{62}Zn$ (E_{beam} = 75 MeV)	
^{59}Ni	2p + n
^{57}Co	α + p
^{56}Co	α + p + n
^{56}Fe	α + 2p

Table 8.2: Main residues associated to ^{62}Zn decay (E^* = 47 MeV, corresponding to E_{beam} = 75 MeV) with the corresponding reaction channels.

An helpful tool for the residual nuclei identification is provided by the particles detected by the EUCLIDES array. Indeed, to require a coincidence with a particle corresponds to select specific decay channels. In Fig. 8.8, for instance, the γ-ray spectrum produced in coincidence with a α particle (in red) is compared to the inclusive spectrum (in black). As one can see, in the red spectrum the γ-transitions related to ^{59}Ni (channel 2p), e.g. E_γ ~340 keV, are not present while the γ-transitions related to ^{57}Co, ^{56}Co and ^{56}Fe are more clearly visible, since they correspond to channels with at least an α particle. Fig. 8.9, instead, shows two spectra corresponding to two different conditions on particles emitted, one α particle (in red) and two protons (in blue).

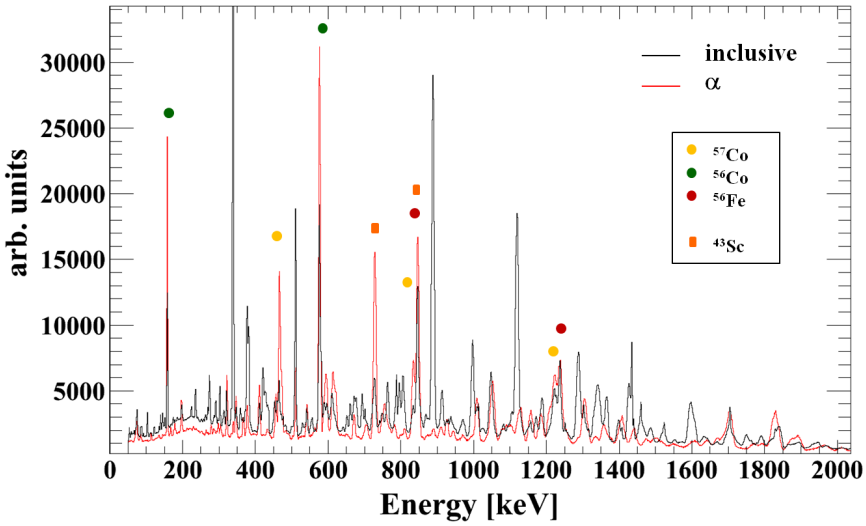

Figure 8.8: Two energy spectra of the GALILEO array associated to the ^{62}Zn decay (E* = 47 MeV, corresponding to E_{beam} = 75 MeV). The black one has been produced without any condition in the sort code, while the red one refers to a coincidence with an α particle detected by the EUCLIDES array. The main residual nuclei are marked.

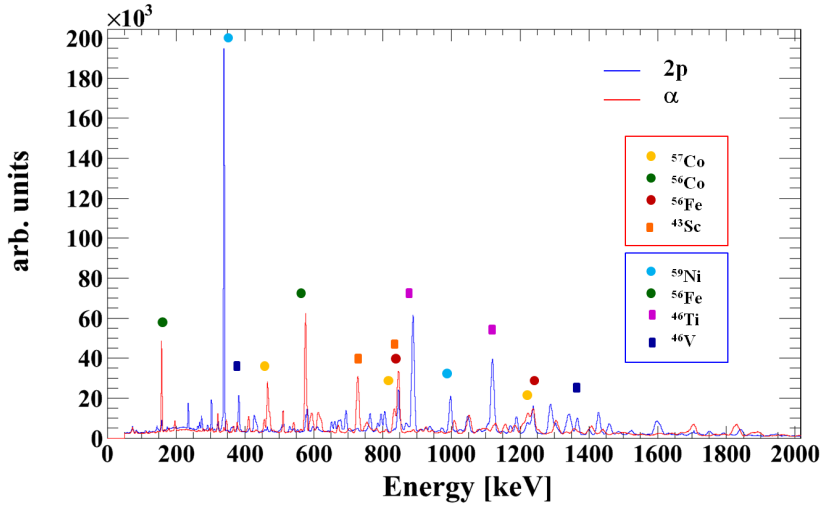

Figure 8.9: Energy spectra of the GALILEO array of ^{62}Zn decay (E* = 47 MeV, corresponding to E_{beam} = 75 MeV) in coincidence with an α particle (red spectrum) or two protons (2p, blue spectrum) detected by the EUCLIDES array. The main residual nuclei in the latter spectrum are marked.

The experimental residues distribution was calculated evaluating the intensity of the transitions, and correcting them by the efficiency of the GALILEO array. The statistical model calculations was performed using the CASCADE code. According to this predictions the four most strongly populated residues are: ^{59}Ni, ^{57}Co, ^{56}Co and ^{56}Fe, in agreement with the experimental data (see Tab. 8.2). The experimental and simulated residual nuclei distributions are shown in Fig. 8.10. They are obtained without any condition (on fold, coincidence etc.). It is possible to assert that the population of the four most intense residues is rather well reproduced by the statistical model, except for ^{56}Fe where the measured and simulated intensities differ by 6 percentage points. This could be related to the fact that, due to the high overlap of peaks in the experimental spectrum, the uncertainties could be important.

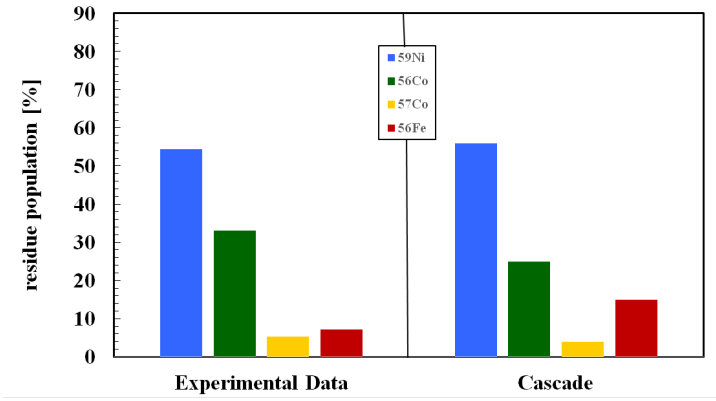

Figure 8.10: Residual nuclei distributions obtained from experimental data, i.e. from the analysis of GALILEO spectrum, (on the left) and from statistical model calculation performed using the code CASCADE (on the right).

Two additional checks have been performed on experimental data. One concerns the evaluation of the residues distribution as a function of the GALILEO fold (and thus for different spin distributions) and the second the evaluation of the residues distribution as a function of the γ-ray energy detected in the $LaBr_3$:Ce array. The results are shown in Fig. 8.11 and Fig. 8.12 respectively.

As one can see in Fig. 8.11 for the two main populated residues, the ^{59}Ni intensity increases with the fold, while the ^{56}Co intensity decreases when the fold increases. Indeed, different fold requirements correspond to the selection of different regions of the phase-space. In particular, the F_γ=3 condition corresponds to an higher average CN spin value than F_γ= 1 or 2 and thus to an higher average rotational energy. For F_γ=3, the available phase-space for particles decay is smaller.

Obviously, also a condition on the energy detected in $LaBr_3$:Ce corresponds to the

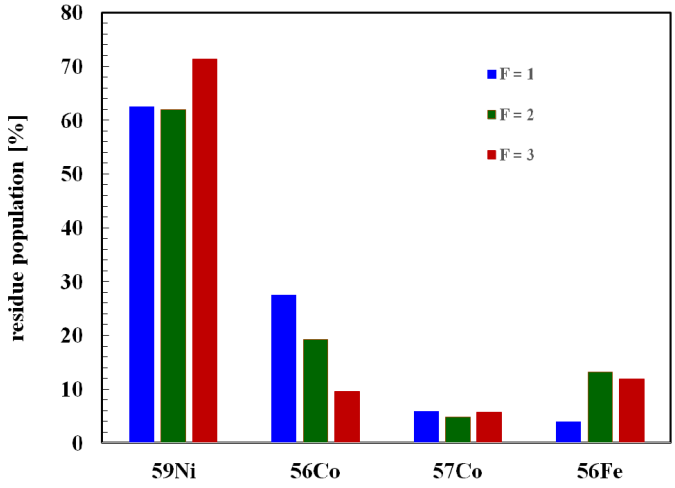

Figure 8.11: Residual nuclei population, obtained from the analysis of GALILEO spectrum, as a function of the GALILEO array fold request, obtained from experimental data. Three fold conditions have been shown.

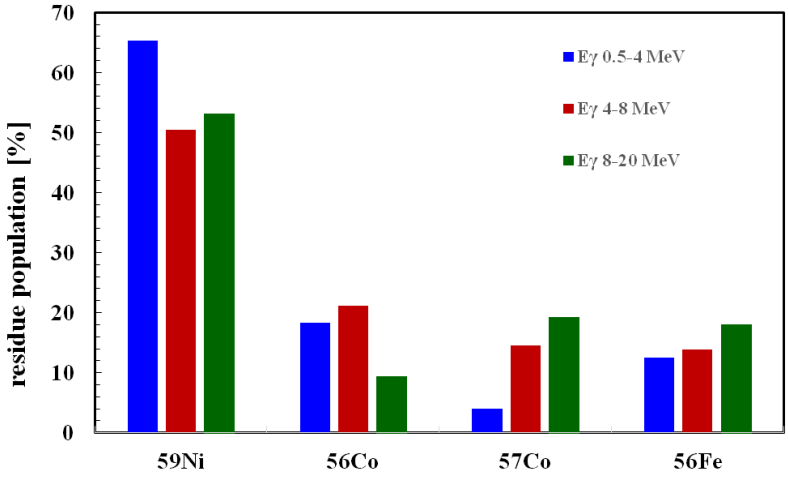

Figure 8.12: Residual nuclei population, obtained from the analysis of GALILEO spectrum, as a function of the energy detected in the $LaBr_3$:Ce array, obtained from experimental data. Three $LaBr_3$:Ce energy range have been considered: 0.5-4 MeV, 4-8 MeV and 8-20 MeV.

selection of a specific phase-space region. In particular, gating on an high-energy γ-ray less phase-space is available for particle decay; therefore, in principle, the residues with less particles emitted should be favourite. In our case (see Fig. 8.12), the experimental data does not show any significant trend in this sense for the two main residues, ^{59}Ni

and ^{56}Co, while the intensity of ^{57}Co and ^{56}Fe seems to increase with the increasing of the $LaBr_3$:Ce energy required. Anyway, the residual trends of Fig. 8.11 and Fig. 8.12 are not clearly evident and this may be due to the fact that the rotational energy is rather small ($0 < E_{rot} < 10$ MeV) and the granularity and the efficiency of the detector are low. In addition, to populate all the four main residues, always two or three particles (n, p, α) have to be emitted (see Tab. 8.2) and, in our case, the sum of the energy removed by the emitted particles is similar in the four cases.

8.2.1 Target contamination

As previously mentioned, the analysis of the GALILEO spectra revealed the presence of nuclei which are not related to the decay of the compound nucleus ^{62}Zn. Such nuclei, mainly ^{46}Ti, ^{46}V and ^{43}Sc, were found to be compatible to the residues of the compound nucleus ^{48}Cr, which could be produced by the fusion reaction: ^{32}S + ^{16}O. This suggested the presence of a oxygen contamination of the target, probably due to the production mechanism.

The ^{28}Si and ^{30}Si targets have been analysed at the AN2000 accelerator of the Laboratory Nazionali di Legnaro (LNL-INFN, Italy) in October 2016. A proton beam was used to determine the targets composition trough Elastic BackScattering (EBS) technique. The results of the analysis, reported in [147], confirmed the presence of O in the targets. In particular, in [147], it is indicated that the ratio between the Si and O amounts is Si/O~1 for the ^{28}Si target and $1.2 \leqslant$ Si/O $\leqslant 1.5$ for the ^{30}Si one. Moreover, some other elements, such as C and Pb, are present within the targets, but in negligible quantities.
It is interesting to note that also a non used target shows the same contamination, and, for the used targets, the same contamination was observed at the beginning and at the end of the measurement.

Fig. 8.13 shows an image of the ^{28}Si target, produced using a scanning electron microscope (SEM), while in Fig. 8.14 a scheme of the two targets composition is reported.

8.3 High-energy γ-ray spectra

As previously mentioned, the high-energy γ-radiation emitted during the compound nucleus decay was detected by the $LaBr_3$:Ce array. It is worth to note that also the evaporated neutrons might be detected by the scintillators array, distorting the γ-ray spectrum. The neutron background can be observed in the $LaBr_3$:Ce Time-Energy matrix of Fig. 8.15, where x-axis and y-axis show the energy and the time associated to an event respectively. The neutron time peak is visible at around 140 ns and the maximal energy deposited appears to be ~8 MeV. Additional background, originated by nucleon-nucleon

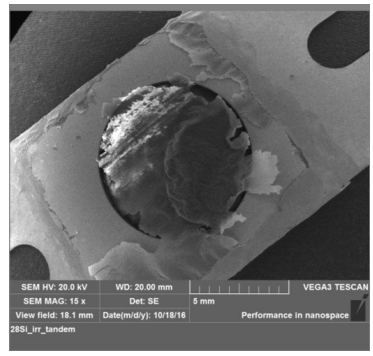

Figure 8.13: ^{28}Si target. The image has been produced by using a scanning electron microscope (SEM). Taken from [147].

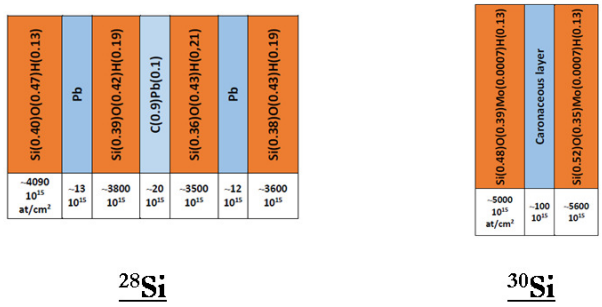

Figure 8.14: Scheme of the composition for the two targets ^{28}Si (on the left) and ^{30}Si (on the right). Taken from [147].

bremsstrahlung radiation and cosmic rays, was present.
In order to reduce the background, a gating condition (3 ns) on the prompt peak in the time spectrum was applied: in Fig. 8.15 it is represented by the black rectangle. The $LaBr_3$:Ce high-energy spectra, with and without the time gate, are shown in Fig. 8.16. Without the time condition, the spectrum (inclusive, in red) is affected by the background, which dominates especially above 10 MeV. The time gate implies a strong reduction of background events in the spectrum (in green) and it highlights a change in the slope above 10 MeV. This is the indication of the IVGDR.

As a preliminary step, the experimental spectrum of ^{62}Zn at E^* = 47 MeV has been compared to the one produced by the statistical model CASCADE, after folding the latter with the $LaBr_3$:Ce response function (see sec. 7.2.4). The two spectra, reported in the left panel of Fig. 8.17, have been normalized between 6 and 8 MeV. As one can see, from a qualitative point of view, the experimental data are well reproduced by the statistical model calculations. The correct IVGDR parameters of ^{62}Zn (and thus of ^{60}Zn) at E^* = 47

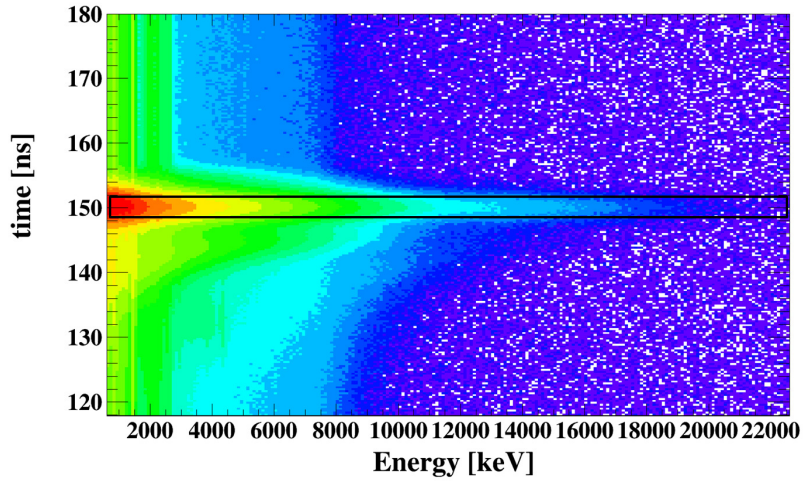

Figure 8.15: Time-Energy matrix of the $LaBr_3$:Ce detectors array, where x-axis and y-axis show the energy and the time associated to an event respectively. Two peaks are visible: the first one at ~ 140 ns represents the neutrons and the one at ~150 ns corresponds to the γ-rays. Furthermore, the rest of the signals are random coincidences coming from nucleon-nucleon bremsstrahlung radiation and cosmic rays. The black rectangle indicated the time gate applied.

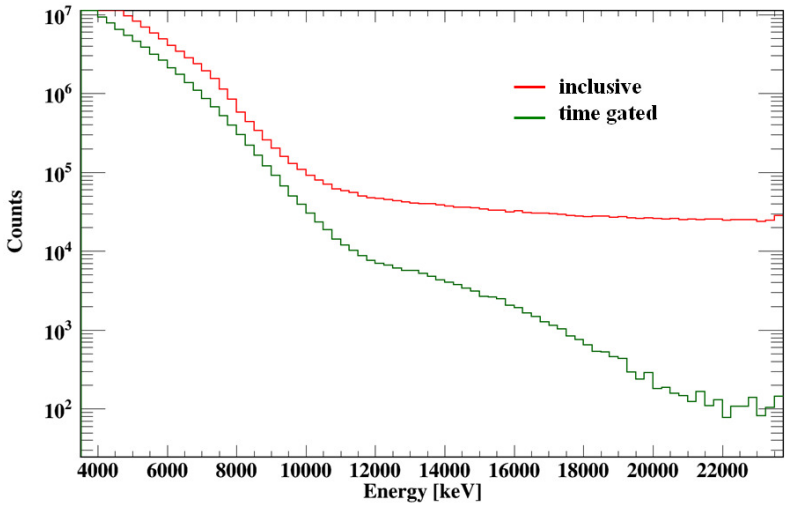

Figure 8.16: High-energy $LaBr_3$:Ce spectra without (in red) and with (in green) the time constraint. The applied time gate is shown in Fig. 8.15.

MeV will be derived from the fit to the data.

The same check has been made for the corresponding reaction: $^{32}S + ^{28}Si$, with E_{beam}

= 86 MeV, which produces ^{60}Zn at the same excitation energy of ^{62}Zn, E* = 47 MeV. The time-gated experimental spectrum is shown in the right panel of Fig. 8.17, together with the one produced by the statistical model, here again folded with the response function. The two spectra have been normalized between 6 and 8 MeV, as for the case of ^{62}Zn. It is worth to note that the version of the CASCADE code used does not include the Isospin formalism, and therefore the Isospin selection rules. As one can see from the experimental spectrum, in this case the γ-decay of the IVGDR is clearly reduced (compared to the statistical model) and this is an evidence of the E1 selection rule, discussed in sec. 2.1. This inhibition, or rather the observed IVGDR strength, is to be quantified in order to extract the Isospin mixing probability. Indeed, as already discussed, in N=Z nuclei E1 transitions with $\triangle$I=0 are forbidden. For a I=0 pure state, the only possible decay is to a I=1 state, with a consequent reduction of the E1 yield. The Isospin mixing attenuate this effect, enhancing the E1 decay yield that would be observed if the Isospin was a conserved quantum number.

Starting from the high-energy experimental spectrum of ^{32}S + ^{28}Si with E$_{beam}$ = 86 MeV (right panel of Fig. 8.17) it is possible to obtain a very preliminary indication about the ^{60}Zn Coulomb spreading width $\Gamma^{\downarrow}$. Using a version of the CASCADE code which includes the Isospin formalism, several different spectra have been generated varying the Coulomb spreading width input value $\Gamma^{\downarrow}$. For each one, which has been firstly normalized, the integral of the spectrum the has been calculated in two energy ranges in the IVGDR region: 15-17 MeV and 15-19 MeV. The obtained integral values are reported in Fig. 8.18 as a function of the Coulomb spreading width $\Gamma^{\downarrow}$, connected by the trend lines (blue and green dashed lines). The same two integral values have been also calculated for the experimental spectrum and, in Fig. 8.18, they are represented by the dashed-dotted lines. The intersections between the simulated and experimental values define the ^{60}Zn Coulomb spreading width energy region, $5 < \Gamma^{\downarrow} < 20$ keV. This is in good agreement with the $\Gamma^{\downarrow}$ literature values obtained with the IAS [25], reported in Fig. 8.19, which are all in the energy range 5-20 keV.

8.4 Discussion

The experiment has been performed in June 2016. The whole data analysis will lead, through the study of the Isospin mixing degree α^2 temperature dependence, to the extraction of the α^2 value at zero temperature for the nucleus ^{60}Zn, which will also allow to determine the correction parameter δ_C for the calculation of the CKM matrix element V_{ud}. To fulfil this ambitious goal several years of work are required.
In particular, to start the analysis the following steps have to be performed for each of the four reactions:

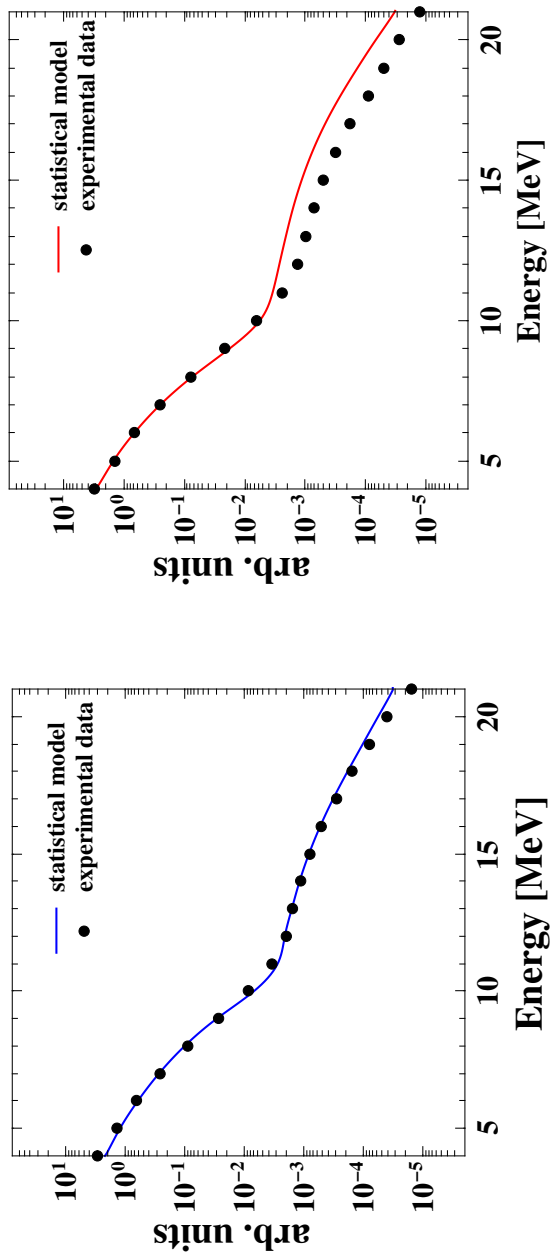

Figure 8.17: Left panel: high energy γ-ray spectra for the reaction ^{32}S + ^{30}Si $\rightarrow$ ^{62}Zn (E_{beam} = 75 MeV, E^* = 47 MeV). The experimental data (filled circles) are shown in comparison to the statistical model calculation (blue line). Right panel: high energy γ-ray spectra for the reaction ^{32}S + ^{28}Si $\rightarrow$ ^{60}Zn (E_{beam} = 86 MeV, E^* = 47 MeV). The experimental data (filled circles) are shown in comparison to the statistical model calculation (red line). It is worth to note the version of the CASCADE code used does not include the Isospin formalism, and therefore the Isospin selection rules.

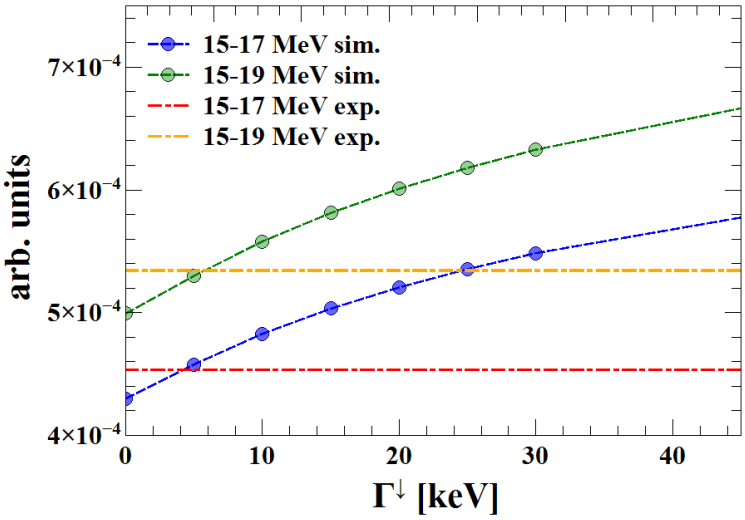

Figure 8.18: Integral of the simulated γ-ray spectra over two different energy region (15-17 MeV, blue full line, and 15-19 MeV, green full line) as a function of the Coulomb spreading width $\Gamma^{\downarrow}$ input value. The simulations have been performed using a CASCADE code which includes the Isospin formalism. The red and yellow dotted-dashed lines represent the integral of the experimental spectrum in the regions 15-17 MeV and 15-19 MeV respectively. The intersection between the experimental and simulated values provides an indication on the ^{60}Zn Coulomb spreading width $\Gamma^{\downarrow}$.

- to tune the experimental set-up: to calibrate and align time and energy spectra ($LaBr_3$:Ce and HPGe detectors),
- to extract the CN spin distribution,
- to identify the residual nuclei distribution for different conditions on measured fold F_γ and on measured coincident high-energy γ-rays,
- to tune the statistical model.

As previously stated, at the moment the data analysis is in a preliminary stage. Two of the four reactions have been considered: ^{32}S + ^{28}Si with E_{beam}= 86 MeV and it's reference reaction ^{32}S + ^{30}Si with E_{beam}= 75 MeV, which populate ^{60}Zn and ^{62}Zn at E^*= 47 MeV. In particular, up to now, only the latter (^{32}S + ^{30}Si with E_{beam}= 75 MeV) has been analysed in detail, following the steps listed above. As it is a reference reaction, it will be used to extract the IVGDR parameters at E^*= 47 MeV for ^{62}Zn, which are supposed to be

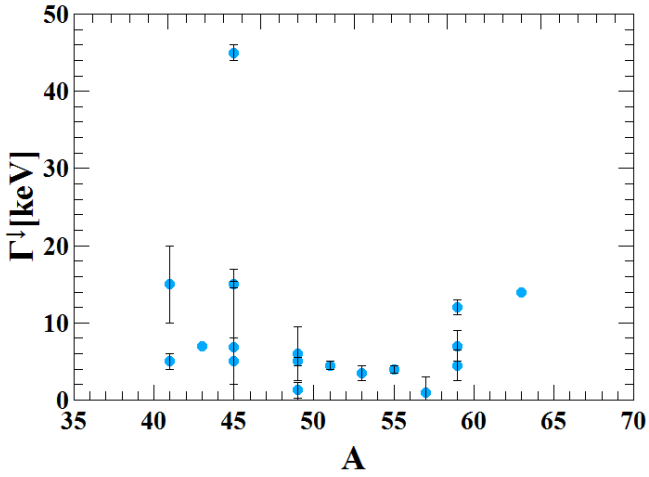

(a)

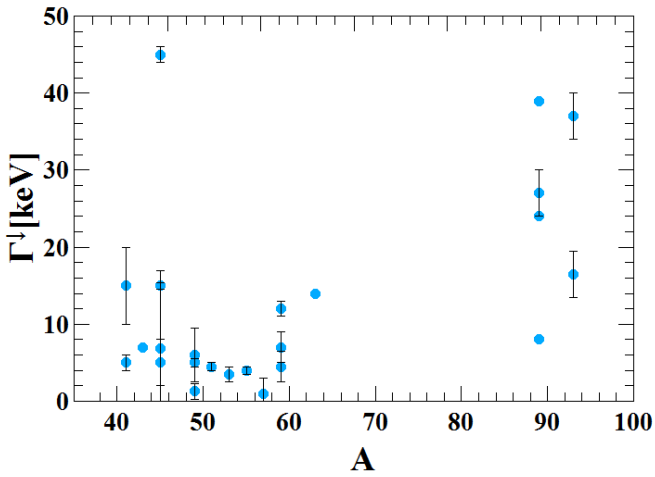

(b)

Figure 8.19: Coulomb spreading width data obtained with the IAS [25] in the mass region $40 \leqslant A \leqslant 70$ (panel (a)) and $40 \leqslant A \leqslant 100$ (panel (b)).

the same for ^{60}Zn at the same excitation energy. Then, the analysis of the γ-decay spectrum of ^{60}Zn will be performed to deduce the Isospin mixing probability α^2 at a finite temperature value T_1, which will be the only free parameter. All these parameters must be extracted with the proper error bar and uncertainty. An unexpected complication is the non negligible target contamination, which must be accounted for.

At the moment, it is not possible to give an $\alpha^2(T_1)$ value. However, already at this stage of the analysis, we have achieved the evidence of the Isospin selection rule and we have

identified the energy range of the ^{60}Zn Coulomb spreading width $\Gamma^{\downarrow}$, which is in good agreement with the literature data. This constitutes the starting point for the α^2 determination.

The procedure described above will be carried on also for the other two reactions: ^{32}S + ^{30}Si with E_{beam}= 98 MeV and ^{32}S + ^{28}Si with E_{beam}= 110 MeV, which populate ^{62}Zn and ^{60}Zn at E^*= 58 MeV. This will lead to the determination of the mixing probability $\alpha^2(T_2)$, at the second temperature value T_2.

Starting from the two obtained values $\alpha^2(T_1)$ and $\alpha^2(T_2)$ and using the theoretical model of Sagawa, Bortignon and Coló [4], discussed in sec. 1.3.2, it will be possible to extract the mixing probability α^2 for ^{60}Zn at T=0 (see sec. 2.3.1). The $\alpha^2_>(T=0)$ value will allow to determine, trough the Auerbach parametrization (reported in sec. 1.4, eq. 1.24), the δ_C correction parameter for the calculation of the CKM matrix element V_{ud}.

CHAPTER 9

Conclusions

In this thesis work the experimental study of the Isospin mixing phenomenon has been approached from two different points of view:

1. possible future experimental apparatuses to investigate the phenomenon through the γ-decay of IsoVector Giant Dipole Resonance (IVGDR),

2. the experimental determination of the Isospin mixing probability in the nucleus ^{60}Zn, using the experimental technique mentioned at point 1.

Firstly, a characterization of two different types of detector which, in the forthcoming future, will represent ideal solutions to investigate the Isospin mixing in self-conjugate nuclei, by measuring the γ-decay of the IsoVector Giant Dipole Resonance, has been conducted.
The first one, the PARIS array, is currently under construction and, in its final configuration, it will be a 4π array composed by phoswich detectors ($LaBr_3$:Ce-NaI:Tl or $CeBr_3$-NaI:Tl). Due to its high efficiency and high granularity, this array will be able to serve the dual purpose to be an high energy γ-ray detector and a multiplicity filter, holding, in a single apparatus, the two main features required for an Isospin mixing measurement via the IVGDR γ-decay. Therefore, the PARIS array represents an advantageous solution for this kind of measurements. The array will be used mainly with stable beams. In general, when at least 8 clusters (72 detectors) are operational, the efficiency will be

enough to allow for the use of specific intense radioactive beams. The general properties of a single phoswich have been here examined. Furthermore, PARIS prototype, the first array cluster, composed by nine $LaBr_3$:Ce-NaI phoswiches, has been characterized through the data analysis of two measurements: an in beam test (Dresden, Germany, 2013) and a source test (Milano, Italy, 2015). The energetic and time performances have been determined and the multiple scattering within the cluster has been studied.
The second detector analysed, the CLYC (Cs_2LiYCl_6:Ce) crystal, is a new generation scintillator belonging to the Elpasolite family. The interest in this new detection system arises from its good energy resolution and its capability to identify (through the pulse shape discrimination technique, PSD), measure, and therefore separate, both neutrons and γ-rays. These features make a CLYC detectors array a unique solution for the experimental investigation of the Isospin mixing via the γ-decay of IVGDR using exotic beams. By balancing the radioactive beams low intensity with the possibility to be placed at short distance from the target, a CLYC array could allow to study the N=Z nuclei in the mass region between ^{80}Zr and ^{100}Sn, which is totally uncharted from this point of view. A measurement of the fast neutron detection efficiency, up to 10 MeV, for two samples of CLYC scintillators (both 1"x1" in size, one enriched with ^{6}Li and the other with ^{7}Li) has been presented in this work. This measurement contributes to a complete characterization work of CLYC scintillators [114], whose performances are currently not well known.

Secondly, an experiment to investigate the Isospin mixing in the N=Z nucleus ^{60}Zn at finite temperature, via the γ-decay of IVGDR, has been proposed and realized. Its final goal will be to extract, using a theoretical model ([4]), the Isospin mixing value for ^{60}Zn at zero temperature. This will be a very important step, since it will provide a validation of the experimental technique, through the comparison to the existent experimental data in the same mass region [5, 6]. It will also confirm the validity of the theoretical model, by means of the comparison to the theoretical prediction [7]. Furthermore, the Isospin mixing value at zero temperature will allow to determine, for mass A=60, the correction parameter δ_C, for the calculation of the CKM matrix element V_{ud}.
The planning and realization of the experiment has been presented here. The data analysis, which requires several years of work, is currently in a preliminary phase. The work of calibration and characterization of the experimental setup has been illustrated. Moreover, the study of one of the fusion-evaporation reactions used, by means of the determination of the residual nuclei populated and of the identification of the compound nucleus angular momentum distribution, has been reported. Finally, a first evidence, in the high-energy γ-ray spectrum, of the E1 selection rule has been pointed out and the range of the Coulomb spreading width $\Gamma^{\downarrow}$ for ^{60}Zn has been identified. This represents the starting point for the Isospin mixing probability determination.

APPENDIX A

Compound Nucleus (CN) theory

The Compound Nucleus (CN) concept was introduced by N. Bohr in 1936 [148], starting from experimental studies of neutron induced processes, to describe the neutron-capture in resonant states:

> *"The phenomena of neutron capture thus force us to assume that a collision between a high-speed neutron and a heavy nucleus will in the first place result in the formation of a compound system of remarkable stability. The possible later breaking up of this intermediate system by the ejection of a material particle, or its passing with emission of radiation to a final state, must in fact be considered as separate competing processes which have no intermediate connexions with the first stage of the encounter."*

The theory has been then extended to describe the intermediate state populated during a fusion-evaporation reaction among heavy-ions.

A CN reaction A(a,b)B can be sketched as:

$$a + A \rightarrow (CN)^* \rightarrow B^* + b, \tag{A.1}$$

where B is the residual nucleus after the particle b decay.
The idea behind the formation of such an intermediate system is that the nuclear force is so strong that the projectile is captured by the target, without any possibility to escape

before all its energy is completely shared among the nucleons of the system. Due to the complete energy sharing, the compound nucleus looses all the memory about its formation process and the decay process is totally independent [149]. This assumption is the so-called *Bohr independence hypothesis*.
This implies that the mean free path of the projectile in the nucleus is much less than the nuclear diameter, so that a long time elapses between the formation and the decay of the compound system.
On the basis of the Bohr independence hypothesis, the CN theory has then been developed by Weisskopf and Ewing [150], with the evaporation theory, and by Hauser and Feshbach, with the introduction of a quantum-mechanical formalism to describe the system [125].
A very brief outline of the compound nucleus theory, which is extremely complicated, will be given in the following sections.

CN statistical description

A CN is formed at high excitation energy. With the increase of the excitation energy, the energy distance between two levels becomes smaller than the their decay width Γ. In this situation, a description of the system in terms of discrete single levels is no more convenient: it is preferable to use a description in terms of a continuum level density ρ.
Thanks to the Bohr independence hypothesis and to this high density of states, the CN and, in particular, its decay can be analysed using a statistical approach: all the degrees of freedom of the system are in equilibrium and thus all the states with the same angular momentum J, parity π and excitation energy E^* have an equal probability to be populated. The detailed balance is valid: the transition matrix elements associated to the formation and to the decay processes are the same.
The probability to populate a nucleus in a state *k* (with angular momentum J_k, parity π_k) with energy E_k is:

$$p_k = \frac{\delta(E_k - E^*)\delta(j_k - j)\delta(\pi_k - \pi)}{\rho(E^*)}. \tag{A.2}$$

This is the Microcanonical probability [47]. Using the Microcanonical formalism, the level density is deduced from the entropy of the system S:

$$\rho = \rho_0 exp^{S(E^*)}, \tag{A.3}$$

Now, starting from the analogy with a system in thermodynamic equilibrium, it is possible to introduce the concept of nuclear temperature T:

$$T = (\frac{dS}{dE^*})^{-1} = (\frac{1}{\rho}\frac{d\rho}{dE^*}). \tag{A.4}$$

The Bethe's Fermi gas formula for the level density, in case of the nuclei, can be written as:

$$\rho(E^*) \approx \frac{e^{2(\sqrt{aE^*})}}{\sqrt{48}E^*}, \tag{A.5}$$

where a is the level density parameter (a = A/10-A/7) MeV^{-1}. The general requirement for a physical system to be described using a statistical approach is a large constituent number. In this sense, the comparison between the atomic nucleus (with A ~ 100 nucleons) with a classic gas (with 10^{23} particles) seems to be improper. Anyway, the statistical description appears more reasonable if we think of the CN in terms of the high number of states. As an example, the number of state, calculated with eq. A.5, for a nucleus with A=100 and E^*=50 MeV is ~10^{17}.

Combining eq. A.5 and eq. A.4, the explicit relation between the nuclear temperature T and the excitation energy E^* is pointed out:

$$E^* = aT^2. \tag{A.6}$$

In analogy with the classical gas, the energy distributions of particles emitted during the CN evaporation process is expected to be Maxwell-Boltzmann distributions, while the angular distribution is expected to be symmetrical about 90°.
With the increasing of the projectile energy, anyway, the limit of the Bohr independence hypothesis becomes more evident due to the increase of the probability of pre-equilibrium emission (i.e. the emission of particle before the thermodynamic equilibrium has been reached) [149].
An evidence of this phenomenon is a γ-ray emission from a dynamic electrical dipole which is formed in fusion reactions during the charge equilibration process. This emission overlaps that related to the statistical decay of the compound nucleus (at thermal equilibrium). The origin of the dynamic dipole is associated to the fact that, in dissipative collisions, energy and angular momentum are quickly distribute among the degrees of freedom, while charge equilibration takes place on a longer time-scale. Thus, for very asymmetric entrance channels, a pre-equilibrium photon emission from the dipole is expected at the time of the formation of CN. This phenomenon has been experimental investigated in [151–153].

CN statistical decay

The compound nucleus decay has been successfully described by Hauser and Feshbach [125], by incorporating the angular momentum conservation. The Hauser-Feshbach formalism is based on the assumption that the thermal equilibrium has been reached before the cooling process. The dependence of the CN fusion cross section on the angular momentum of the system J is given by:

$$\sigma_{fus}(J) = \sum_{J} \pi\lambda^2 \frac{2J+1}{1+exp(\frac{J-J_0}{d})}, \tag{A.7}$$

where J_0 is the angular momentum cut-off. It can be measured, constrained from systematic or obtained from the Bass model [154]. d is the diffuseness, which can vary from 2 up to 10 $\hbar$.
The partial decay width for the particle *i* evaporation of a CN with excitation energy E^* and angular momentum J_{CN} is parametrized as:

$$\Gamma_i(E^*, J_{CN}) = \frac{1}{2\pi\rho_{CN}(E^*, J_{CN})} \int d\epsilon \sum_{J_d=0}^{\infty} \sum_{|J_{CN}-J_d|}^{J_{CN}-J_d} \sum_{l=|J-S_i|}^{J+S_i} T_l(\epsilon)\rho_d(E^* - B_i - \epsilon). \tag{A.8}$$

J_d is the spin of the daughter nucleus. S_i, J and l are the spin, the total and the orbital angular momenta of the evaporated particle *i* respectively, while ϵ and B_i its kinetic and separation energies. ρ_{CN} and ρ_d are the level densities of the CN and the daughter nucleus and T_l is the trasmission coefficent or barrier penetration factor.
For γ-decay, T_l can be written as [155]:

$$T_l(E_\gamma) = \xi_l E_\gamma^{2l+1}, \tag{A.9}$$

being ξ_l a constant, to be estimated from the strength of transitions between low-lying states in the mass region of interest or from the Weisskopf single-particle estimate.

In a schematic view, the CN decay is composed by two main phases. In the first one, when the compound system is formed, the excitation energy E^* is higher than the nuclear binding energy (~8 MeV): the CN de-excitation occurs through particles emission, in particular neutrons, which do not have to cross the Coulomb barrier. The neutron emission is in competition with the γ-decay of the Giant Dipole Resonance: the typical branching ratio is $\frac{P_\gamma}{P_n} \approx 10^{-3}$.
In the second phase, in which E^* is lower than the particle separation energy, the CN can only decay through γ-ray emission [21]. Fig. A.1 shows a schematic representation of CN decay.

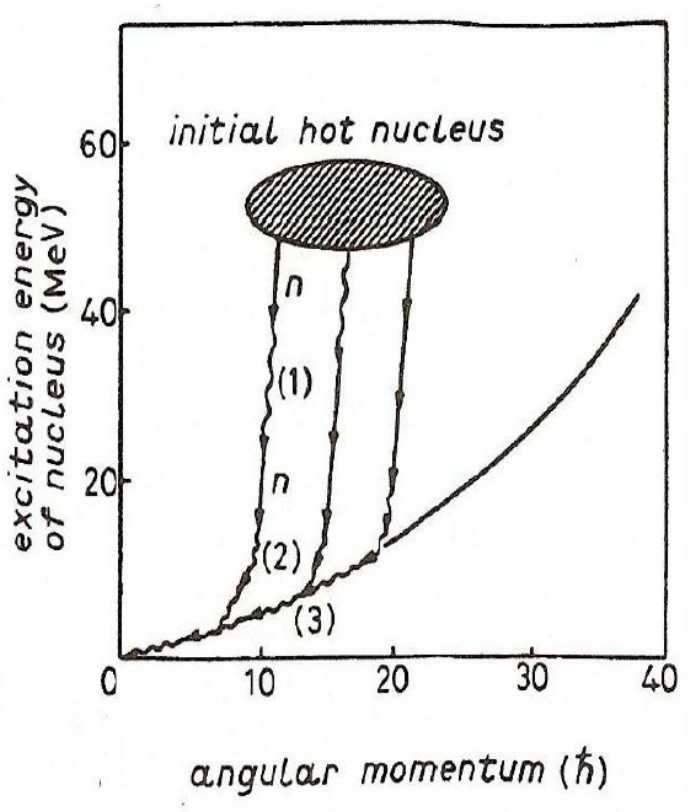

Figure A.1: Schematic representation of CN decay. (1), (2) and (3) indicate the γ-rays from GDR decay, neutron emission and the γ-radiation along the Yrast line respectively.

APPENDIX B

The Isobaric Analog State (IAS)

Analog states are particular energy levels of a nucleus which have a special relationship to energy levels in the neighbouring nucleus with the same mass number A. In particular, defining N, Z and I_0 the neutron number, the proton number and the Isospin of the ground state of the parent nucleus $|\pi\rangle$, its Isobaric Analog State $|IAS\rangle$ is the first state of the nucleus with N-1 neutrons and Z+1 protons which has Isospin I_0. The $|IAS\rangle$ has the same quantum numbers of $|\pi\rangle$ except for I_z that is one unit lower, and it preserves the wave function of $|\pi\rangle$. However, since one more proton means a larger Coulomb interaction energy, the Isobaric Analog State lies at higher excitation energy than $|\pi\rangle$.
In the nucleus (N-1,Z+1), starting from the $|IAS\rangle$ state energy, a set of excited levels that matches one-to-one the lowest levels of the parent nucleus (N,Z), in terms of spacing energy and other properties, can be identified. The first evidence for the existence of the Isobaric Analog State has been presented in [156] by Anderson and Wong (1961) for the nucleus ^{51}Cr, obtained from proton bombardment of ^{51}V.

As we mentioned above, because of the Coulomb interaction, the IAS (also know as IAR, Isobaric Analog Resonance) is shifted upwards in energy with respect to the parent state and its lifetime becomes finite. Since its excitation energy exceeds the particle separation energy, the IAS can decay by the emission of a proton or a neutron and therefore it acquires a width Γ. A narrow width is an important characteristic of the IAS. It can be

written as:

$$\Gamma_{\mathrm{IAS}} = \Gamma^{\uparrow}_{\mathrm{IAS}} + \Gamma^{\downarrow}_{\mathrm{IAS}}. \tag{B.1}$$

$\Gamma^{\uparrow}_{\mathrm{IAS}}$ is the sum of all particle decay widths, which is dominated by the allowed proton decay.
$\Gamma^{\downarrow}_{\mathrm{IAS}}$ is the spreading width and it is dominated by the Isospin-forbidden neutron decay. It is generated by the coupling of the IAS to the IsoVector Giant Monopole Resonance, due to the Coulomb interaction [157]. A sketch of an IAS (IAR) decay is reported in Fig. B.1.

Particular interest has been dedicated to the understanding and determination of the spreading width $\Gamma^{\downarrow}_{\mathrm{IAS}}$, since it represents a way to study the Coulomb interaction effects in the nuclear medium [19, 157–159]. As it is due to the Coulomb interaction, the spreading width is expected to increase with the proton number. The experimental data confirm this idea, as shown in Fig. B.2 [158].

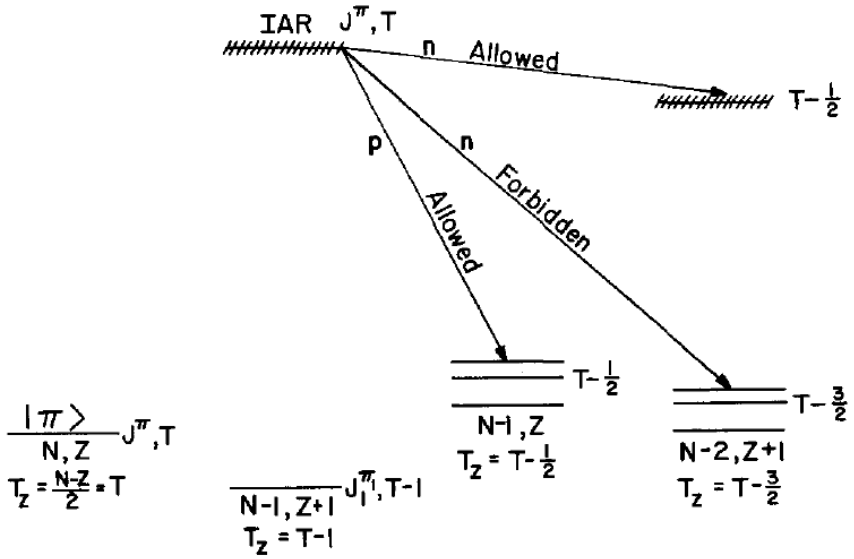

Figure B.1: The decay scheme of an IAS (or IAR) with a neutron excess parent. [157].

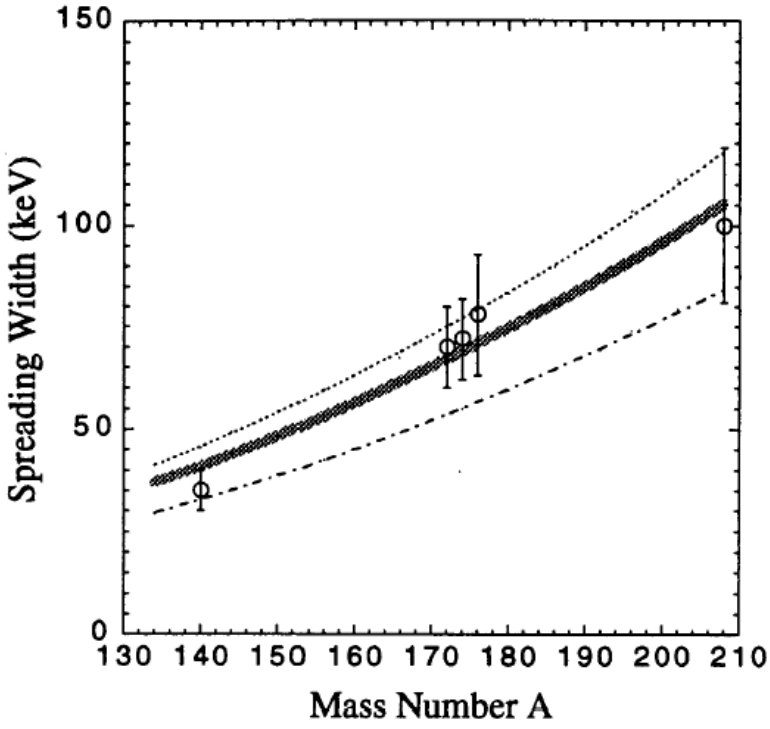

Figure B.2: Comparison between experimental data (circles) and theoretical calculations (lines) of the IAS spreading width as a function of the mass number A [158].

Bibliography

[1] D. D Warner, M. A. Bentley, and P. Van Isacker, Nature Physics **2** (2006).

[2] A. Corsi, et al., Phys. Rev. C **84**, 041304 (2011).

[3] S. Ceruti, et al., Phys. Rev. Lett. **115**, 222502 (2015).

[4] H. Sagawa, P. Bortignon, and G. Colò, Physics Letters B **444**, 1 (1998).

[5] E. Farnea, et al., Physics Letters B **551**, 56 (2003).

[6] I. S. Towner and J. C. Hardy, Phys. Rev. C **82**, 065501 (2010).

[7] W. Satuła, et al., Phys. Rev. Lett. **103**, 012502 (2009).

[8] A. Maj, et al., Acta Physica Polonica B **40**, 565 (2009).

[9] A. Bohr and B. R. Mottelson, *Nuclear Structure: Single particle motion*, Vol. 1 (World Scientific, 2008).

[10] F. Sammarruca, L. White, and B. Chen, The European Physical Journal A **48**, 181 (2012).

[11] W. Heisenberg, Zeitschrift für Physik **77**, 1 (1932).

[12] D. Wilkinson, *Isospin in nuclear physics* (North Holland Pub. Co., 1970).

[13] M. MacCormick and G. Audi, Nuclear Physics A **925**, 61 (2014).

[14] M. A. Bentley, et al., Phys. Rev. Lett. **97**, 132501 (2006).

[15] S. M. Lenzi and M. Bentley, in *The Euroschool Lectures on Physics with Exotic Beams, Vol. III* (Springer, 2009), pp. 57–98.

[16] J. Ekman, et al., The European Physical Journal A - Hadrons and Nuclei **9**, 13 (2000).

[17] J. Ekman, et al., Phys. Rev. C **70**, 014306 (2004).

[18] I. Hamamoto and H. Sagawa, Phys. Rev. C **48**, R960 (1993).

[19] T. Suzuki, H. Sagawa, and G. Colò, Phys. Rev. C **54**, 2954 (1996).

[20] M. Bentley and S. Lenzi, Progress in Particle and Nuclear Physics **59**, 497 (2007).

[21] S. Ceruti, Ph.D. thesis, Physics, Astrophysics and Applied Physics PhD School, Universitá degli Studi di Milano, Milano (2016).

[22] J. A. Behr, Ph.D. thesis, University of Washington (1991).

[23] D. H. Wilkinson, The Philosophical Magazine: A Journal of Theoretical Experimental and Applied Physics **1**, 379 (1956), http://dx.doi.org/10.1080/14786435608238116.

[24] H. Morinaga, Phys. Rev. **97**, 444 (1955).

[25] H. L. Harney, A. Richter, and H. A. Weidenmüller, Rev. Mod. Phys. **58**, 607 (1986).

[26] P. Donati, et al., Physics Letters B **383**, 15 (1996).

[27] S. Ceruti, et al., Phys. Rev. C **95**, 014312 (2017).

[28] N. Cabibbo, Phys. Rev. Lett. **10**, 531 (1963).

[29] I. S. Towner and J. C. Hardy, Phys. Rev. C **77**, 025501 (2008).

[30] I. S. Towner and J. C. Hardy, Phys. Rev. C **66**, 035501 (2002).

[31] J. C. Hardy and I. S. Towner, Phys. Rev. C **71**, 055501 (2005).

[32] I. S. Towner and J. C. Hardy, in *Proceedings of the 5th International WEIN Symposium: Physics Beyond the Standard Model, Santa Fe, NM, 1998*, edited by H.-V. K.-K. edited by P. Herczeg, CM. Hoffman (World Scientific, Singapore, 1999, ????), p. 338–359.

[33] H. Sagawa, N. V. Giai, and T. Suzuki, Phys. Rev. C **53**, 2163 (1996).

[34] W. Satuła, et al., Phys. Rev. Lett. **106**, 132502 (2011).

[35] N. Auerbach, Phys. Rev. C **79**, 035502 (2009).

[36] D. Rodríguez, et al., Phys. Rev. Lett. **93**, 161104 (2004).

[37] J. Damgaard, Nuclear Physics A **130**, 233 (1969).

[38] I. Towner, J. Hardy, and M. Harvey, Nuclear Physics A **284**, 269 (1977).

[39] M. Harakeh and A. Woude, *Giant Resonances: Fundamental High-frequency Modes of Nuclear Excitation*, Oxford science publications (Oxford University Press, 2001).

[40] B. L. Berman and S. C. Fultz, Rev. Mod. Phys. **47**, 713 (1975).

[41] P. Carlos, et al., Nucl. Phys. **A219**, 61 (1974).

[42] F. S. Dietrich, et al., Phys. Rev. C **10**, 795 (1974).

[43] J. O. Newton, et al., Phys. Rev. Lett. **46**, 1383 (1981).

[44] D. M. Brink, Ph.D. thesis, Oxford University (1955).

[45] P. Axel, Phys. Rev. **126**, 671 (1962).

[46] K. A. Snover, Annual Review of Nuclear and Particle Science **36**, 545 (1986), https://doi.org/10.1146/annurev.ns.36.120186.002553.

[47] P. Bortignon, A. Bracco, and R. Broglia, *Giant Resonances: Nuclear Structure at Finite Temperature*, Contemporary concepts in physics (Harwood, 1998).

[48] A. Bracco, et al., Modern Physics Letters A **22**, 2479 (2007), http://www.worldscientific.com/doi/pdf/10.1142/S0217732307024474.

[49] J. Gaardhøje, et al., Physics Letters B **139**, 273 (1984).

[50] J. J. Gaardhoje, Annual Review of Nuclear and Particle Science **42**, 483 (1992), https://doi.org/10.1146/annurev.ns.42.120192.002411.

[51] M. Mattiuzzi, et al., Nuclear Physics A **612**, 262 (1997).

[52] D. Kusnezov, Y. Alhassid, and K. A. Snover, Phys. Rev. Lett. **81**, 542 (1998).

[53] O. Wieland, et al., Phys. Rev. Lett. **97**, 012501 (2006).

[54] H. J. Hofmann, et al., Nucl. Phys. **A571**, 301 (1994).

[55] D. Kusnezov and W. E. Ormand, Phys. Rev. Lett. **90**, 042501 (2003).

[56] D. Pandit, et al., Phys. Rev. C **88**, 054327 (2013).

[57] D. Pandit, et al., Physics Letters B **713**, 434 (2012).

[58] D. Pandit, et al., Physics Letters B **713**, 434 (2012).

[59] N. Severijns, et al., Phys. Rev. C **71**, 064310 (2005).

[60] E. Kuhlmann, Phys. Rev. C **20**, 415 (1979).

[61] M. Harakeh, et al., Physics Letters B **176**, 297 (1986).

[62] J. A. Behr, et al., Phys. Rev. Lett. **70**, 3201 (1993).

[63] M. Kicińska-Habior, et al., Nuclear Physics A **731**, 138 (2004).

[64] D. Mondal, et al., Physics Letters B **763**, 422 (2016).

[65] A. Corsi, Ph.D. thesis, Physics, Astrophysics and Applied Physics PhD School, Universitá degli Studi di Milano, Milano (2011).

[66] *Paris*, URL http://paris.ifj.edu.pl.

[67] I. Mazumdar et al., *A report on the possible experiments to characterise paris array*, http://paris.ifj.edu.pl/articles (2012).

[68] O. Dorvaux et al., Detectors Working-Group Report, *paris prototype*, http://paris.ifj.edu.pl/articles (2012).

[69] A. Mentana, Master's thesis, Universitá degli Studi di Milano (2014).

[70] A. Maj et al., PARIS Detector-Progress Report, *high-energy γ-rays as a probe of hot nuclei and reaction mechanism*, http://paris.ifj.edu.pl/articles (2011).

[71] M. Zięblíński, et al., Acta Physica Polonica B **44**, 651 (2013).

[72] A. Giaz, et al., Nuclear Instruments and Methods in Physics Research Section A: Accelerators, Spectrometers, Detectors and Associated Equipment **729**, 910 (2013).

[73] O. a. Roberts.

[74] Saint-Gobain, URL `www.crystal.saint-gobain.com`.

[75] S. Agostinelli, et al., Nuclear Instruments and Methods in Physics Research Section A: Accelerators, Spectrometers, Detectors and Associated Equipment **506**, 250 (2003).

[76] J. Allison, et al., IEEE Transactions on Nuclear Science **53**, 270 (2006).

[77] G. F. Knoll, *Radiation detection and measurement; 4th ed.* (Wiley, New York, NY, 2010).

[78] E. Nácher, et al., Nuclear Instruments and Methods in Physics Research Section A: Accelerators, Spectrometers, Detectors and Associated Equipment **769**, 105 (2015).

[79] Saint-Gobain, private communication.

[80] G. Cozzi, et al., in press.

[81] Scionix, private communication.

[82] *Lifetime measurements of excited states in neutron-rich c and o isotopes: a stringent test of the three body forces with the agata+paris+vamos setup*, Experiment proposal, GANIL Laboratory, Caen (FR).

[83] *Root cern*, URL `https://root.cern.ch/`.

[84] B. Wasilewska, et al., Journal of Physics: Conference Series **620**, 012006 (2015).

[85] C. Ghosh, et al., Journal of Instrumentation **11**, P05023 (2016).

[86] G. Hull, et al., Nuclear Instruments and Methods in Physics Research Section A: Accelerators, Spectrometers, Detectors and Associated Equipment **695**, 350 (2012), new Developments in Photodetection NDIP11.

[87] R. Schwengner, et al., Nuclear Instruments and Methods in Physics Research Section A: Accelerators, Spectrometers, Detectors and Associated Equipment **555**, 211 (2005).

[88] *Nuclear resonane fluorescence-nrf-experiments at elbe*, URL `http://www.hzd.de`.

[89] K. Krane, *Introductory Nuclear Physics* (Wiley, 1987).

[90] *The bremsstrahlung facility at the elbe accelerator*, URL `http://www.hzd.de`.

[91] S. Brambilla, et al., in *Proceedings, 2012 IEEE Nuclear Science Symposium and Medical Imaging Conference (NSS/MIC 2012): Anaheim, California, USA, October 29-November 3, 2012* (2012), pp. 1087–1089.

[92] C. Boiano, et al., in *IEEE Nuclear Science Symposuim Medical Imaging Conference* (2010), pp. 268–270, ISSN 1082-3654.

[93] C. Boiano, A. Guglielmetti, and S. Riboldi, in *Proceedings, 2012 IEEE Nuclear Science Symposium and Medical Imaging Conference (NSS/MIC 2012): Anaheim, California,*

USA, October 29-November 3, 2012 (2012), pp. 865–867.

[94] R. Nicolini, et al., Nuclear Instruments and Methods in Physics Research Section A: Accelerators, Spectrometers, Detectors and Associated Equipment **582**, 554 (2007).

[95] A. Giaz, et al., Nuclear Instruments and Methods in Physics Research Section A: Accelerators, Spectrometers, Detectors and Associated Equipment **810**, 132 (2016).

[96] C. Combes, et al., Journal of Luminescence **82**, 299 (1999).

[97] B. S. Budden, et al., IEEE Transactions on Nuclear Science **60**, 946 (2013).

[98] J. Glodo, et al., IEEE Transactions on Nuclear Science **55**, 1206 (2008).

[99] J. Glodo, R. Hawrami, and K. Shah, Journal of Crystal Growth **379**, 73 (2013), compound Semiconductors and Scintillators for Radiation Detection Applications: A Special Tribute to the Research of Michael Schieber.

[100] J. Glodo, et al., IEEE Transactions on Nuclear Science **58**, 333 (2011).

[101] N. D'Olympia, et al., Nuclear Instruments and Methods in Physics Research Section A: Accelerators, Spectrometers, Detectors and Associated Equipment **694**, 140 (2012).

[102] N. D'Olympia, et al., Nuclear Instruments and Methods in Physics Research Section A: Accelerators, Spectrometers, Detectors and Associated Equipment **714**, 121 (2013).

[103] M. Bourne, et al., Nuclear Instruments and Methods in Physics Research Section A: Accelerators, Spectrometers, Detectors and Associated Equipment **736**, 124 (2014).

[104] D. Lee, et al., Nuclear Instruments and Methods in Physics Research Section A: Accelerators, Spectrometers, Detectors and Associated Equipment **664**, 1 (2012).

[105] K. Yang and P. R. Menge, Nuclear Instruments and Methods in Physics Research Section A: Accelerators, Spectrometers, Detectors and Associated Equipment **784**, 74 (2015), symposium on Radiation Measurements and Applications 2014 (SORMA XV).

[106] M. Smith, et al., Nuclear Instruments and Methods in Physics Research Section A: Accelerators, Spectrometers, Detectors and Associated Equipment **784**, 162 (2015), symposium on Radiation Measurements and Applications 2014 (SORMA XV).

[107] M. B. Smith, et al., IEEE Transactions on Nuclear Science **60**, 855 (2013).

[108] A. Giaz, et al., Nuclear Instruments and Methods in Physics Research Section A: Accelerators, Spectrometers, Detectors and Associated Equipment **825**, 51 (2016).

[109] N. D'Olympia, et al., Nuclear Instruments and Methods in Physics Research Section A: Accelerators, Spectrometers, Detectors and Associated Equipment **763**, 433 (2014).

[110] L. Pellegri, et al., in *2013 IEEE Nuclear Science Symposium and Medical Imaging Con-*

ference (2013 NSS/MIC) (2013), pp. 1–3, ISSN 1082-3654.

[111] *Iaea nds/exfor*, URL `https://www-nds.iaea.org/exfor/endf.htm`.

[112] U. Pujala, et al., Radiation Protection and Environment **34**, 262 (2011), `http://www.rpe.org.in/text.asp?2011/34/4/262/106194`.

[113] https://it.mathworks.com.

[114] A. Mentana, et al., in *Journal of Physics: Conference Series* (IOP Publishing, 2016), vol. 763, p. 012006.

[115] C. Allwork, et al., in *2015 IEEE Nuclear Science Symposium and Medical Imaging Conference (NSS/MIC)* (2015), pp. 1–7.

[116] *Mcnpx home page*, URL `http://mcnpx.lanl.gov/`.

[117] A. Schiller and M. Thoennessen, Atom. Data Nucl. Data Tabl. **93**, 549 (2007), `nucl-ex/0605004`.

[118] O. Tarasov and D. Bazin, Nuclear Instruments and Methods in Physics Research Section B: Beam Interactions with Materials and Atoms **204**, 174 (2003).

[119] O. Tarasov and D. Bazin, Nuclear Instruments and Methods in Physics Research Section B: Beam Interactions with Materials and Atoms **266**, 4657 (2008).

[120] *Study of isospin symmetry in* ^{60}zn, Experiment proposal, Laboratori Nazionali di Legnaro INFN (LNL-INFN), PD Italy (February 2016).

[121] F. Pühlhofer, Nuclear Physics A **280**, 267 (1977).

[122] I. Diószegi, Phys. Rev. C **64**, 019801 (2001).

[123] R. J. Charity, Phys. Rev. C **82**, 014610 (2010).

[124] Ciemała, M. and Kmiecik, M. and Krzysiek, M. and Maj, A. and Mazurek, K. and Charity, R. and Mancusi, D., Acta Physica Polonica B **44**, 611 (2013).

[125] W. Hauser and H. Feshbach, Phys. Rev. **87**, 366 (1952).

[126] J. Valiente Dobón et al., *Lnl-infn annual report 2014* (2015).

[127] A. Gadea et al., *Lnl-infn annual report 1996* (1997).

[128] A. Gadea et al., *Lnl-infn annual report 1999* (2000).

[129] Ö.Skeppstedt, et al., Nuclear Instruments and Methods in Physics Research Section A: Accelerators, Spectrometers, Detectors and Associated Equipment **421**, 531 (1999).

[130] D. Barrientos et al., *Lnl-infn annual report 2014* (2015).

[131] *Spes project*, URL `https://web.infn.it/spes/`.

[132] D. Mengoni et al., *Lnl-infn annual report 2013* (2014).

[133] D. Barrientos et al., *Lnl-infn annual report 2012* (2013).

[134] D. Testov et al., *Lnl-infn annual report 2014* (2015).

[135] D. Testov et al., *Lnl-infn annual report 2016* (2017).

[136] D. Jannis, Master's thesis, KU Leuven - Faculty of Science (2017).

[137] A. Lonardi, Bachelor thesis, Universitá degli Studi di Padova (2014-2015).

[138] J. Ljungvall, M. Palacz, and J. Nyberg, Nuclear Instruments and Methods in Physics Research Section A: Accelerators, Spectrometers, Detectors and Associated Equipment **528**, 741 (2004).

[139] G. Benzoni et al., *Lnl-infn annual report 2015* (2016).

[140] J. Gutleber, S. Murray, and L. Orsini, Computer Physics Communications **153**, 155 (2003).

[141] L. Berti et al., *Lnl-infn annual report 2016* (2017).

[142] A. Gozzellino (2017), workshop *GALILEO Days 2017*, 20-22 September 2017, Laboratori nazionali di Legnaro (LNL-INFN, PD Italy).

[143] S. Lodetti, Bachelor thesis, Universitá degli Studi di Milano (2011-2012).

[144] I. Mukul, et al., Phys. Rev. C **88**, 024312 (2013).

[145] *Radware*, URL `http://radware.phy.ornl.gov/`.

[146] *Nudat - national nuclear data center*, URL `www.nndc.bnl.gov/`.

[147] V. Rigato and *Laboratori Nazionali di Legnaro (LNL-INFN)*, private communication.

[148] N. Bohr, Nature **137**, 344 (1936).

[149] E. Gadioli and P. E. Hodgson, *Pre-Equilibrium in Nuclear Reaction* (Oxford Science Publications, 1992).

[150] V. F. Weisskopf and D. H. Ewing, Phys. Rev. **57**, 935 (1940).

[151] D. Pierroutsakou, et al., Phys. Rev. C **80**, 024612 (2009).

[152] A. Corsi, et al., Physics Letters B **679**, 197 (2009).

[153] A. Giaz, et al., Phys. Rev. C **90**, 014609 (2014).

[154] R. Bass, *Nuclear Reaction with Heavy Ions*, Theoretical and Mathematical Physics (Springer-Verlag Berlin Heidelberg, 1980).

[155] J. R. Grover and J. Gilat, Phys. Rev. **157**, 802 (1967).

[156] A. C. Anderson, et al., Phys. Rev. Lett. **7**, 220 (1961).

[157] N. Auerbach, Physics Reports **98**, 273 (1983).

[158] H. Orihara, et al., Phys. Rev. Lett. **81**, 3607 (1998).

[159] J. Jänecke, M. Harakeh, and S. Van der Werf, Nuclear Physics A **463**, 571 (1987).